ABSTRACT

ATOMIC AND ELECTRONIC STRUCTURE STUDIES OF NANO-STRUCTURED SYSTEMS: CARBON AND RELATED MATERIALS

by

Sumit Saxena

Modeling in the framework of density functional theory has been conducted on carbon nanotubes and graphene nano-structures. The results have been extended to non-carbon systems such as boron nanostructures. Computational studies are complemented by experimental methods to refine the structural models and obtain a better understanding of the electronic structure.

It is observed that the zigzag edged bilayered graphene nanoribbons are highly unstable as compared to their armchair counterparts. A novel approach has been proposed for the patterning of chirality/diameter controlled single walled carbon nanotubes. Nanotube formation is found to be assisted by edge ripples along with the intrinsic edge reactivity of different types of bilayered GNRs.

The effect of bundling on the electronic structure of single walled carbon nanotubes in zigzag single walled carbon nanotubes has been studied. Hydrostatic pressure effects were examined on bundled single walled carbon nanotubes. Nanotubes with chiral indices (3n + 3, 3n + 3) acquire hexagonal cross-sections on application of hydrostatic pressures. The formation of a novel quasi two-dimensional phase of carbon during hydrostatic compression of small and large nanotubes under extreme conditions of pressure is modeled and is understood to be dictated by breaking of symmetry during compression. Nanoscale materials with anisotropic compressibility do not exhibit symmetric compression as in bulk materials.

Structural stability of boron nanoribbons derived from ‘α-sheet’ and reconstructed {1221} sheets was studied. Antiaromatic instabilities were found to destabilize nanoribbons constructed from reconstructed {1221} sheets when compared to those obtained from the ‘α-sheet’. The stability of the nanoribbons was found to increase with increasing width and increase in the hole density (η) of the boron nanoribbons. The study of electronic structure reveals the presence of semiconducting nanostructures.

The presence of nanoscale crystalline domains due to random functionalization has made it difficult to resolve the chemical structure of graphene oxide and it remains a much debated topic to date. A combination of analytical, spectroscopic and density functional techniques have been used to determine the structure and properties of such nano materials. Graphene oxide has unusual exotic properties and belongs to this class of materials. Investigations reveal that the chemical structure of graphene oxide can be visualized as puckered graphene sheets linked by oxygen atoms. Density functional theory has been used to calculate the site projected partial density of states for carbon and oxygen atoms involved in different types of bonding. A comparison of these simulations with carbon and oxygen K-edge absorption spectra has led to an understanding of the basic electronic structure of this material.

ATOMIC AND ELECTRONIC STRUCTURE STUDIES OF NANO-STRUCTURED SYSTEMS: CARBON AND RELATED MATERIALS

by
Sumit Saxena

A Dissertation
Submitted to the Faculty of
New Jersey Institute of Technology
in Partial Fulfillment of the Requirements for the Degree of
Doctor of Philosophy in Materials Science and Engineering

Interdisciplinary Program in Materials Science and Engineering

August 2010

.

APPROVAL PAGE

ATOMIC AND ELECTRONIC STRUCTURE STUDIES OF NANO-STRUCTURED SYSTEMS: CARBON AND RELATED MATERIALS

Sumit Saxena

Dr. Trevor A. Tyson, Dissertation Advisor — Date
Professor of Physics, NJIT

Dr. Joseph W. Bozzelli, Committee Member — Date
Distinguished Professor of Chemistry, NJIT

Dr. Keun H. Ahn, Committee Member — Date
Assistant Professor of Physics, NJIT

Dr. Reginald Farrow, Committee Member — Date
Research Professor of Physics, NJIT

Dr. Huixin He, Committee Member — Date
Associate Professor of Chemistry, Rutgers-Newark, NJ

BIOGRAPHICAL SKETCH

Author: Sumit Saxena

Degree: Doctor of Philosophy

Date: August 2010

Undergraduate and Graduate Education:

- Doctor of Philosophy in Materials Science and Engineering,
  New Jersey Institute of Technology, Newark, NJ, USA, 2010

- Master of Science in Physics,
  Indian Institute of Technology - Kanpur, Kanpur, UP, India, 2001

- Bachelor of Science in Physics and Mathematics,
  Bundelkhand University, Jhansi, India, 1999

Major: Materials Science and Engineering

Publications:

Sumit Saxena and Trevor A. Tyson, "Local Electronic Structure of Graphene Oxide," (submitted to Physical Review Letters on 06/15/2010).

Sumit Saxena and Trevor A. Tyson, "What is Graphene Oxide," (submitted to Advanced Materials on 08/06/2010).

Sumit Saxena and Trevor A. Tyson, "Insights on the Atomic and Electronic Structure of Boron Nanoribbons," Physical Review Letters, 104, 245502, 2010.

Sumit Saxena and Trevor A. Tyson, "Interacting Quasi Two-Dimensional Sheets of Interlinked Carbon Nanotubes: A High Pressure Phase of Carbon," ACS Nano, 4, 3515, 2010.

Sumit Saxena and Trevor A. Tyson, "Ab-Initio Density Functional Studies of the Reconstructing of Graphene Nanoribbons to form Tailored Single Walled Carbon Nanotubes," CARBON, 48, 1153, 2010.

Sumit Saxena, "Sol-Gel Preparation and Characterization of TbxY3-xAl5O12," Materials Letters, 60, 1315, 2006.

Sumit Saxena, Archana Asokkumar K. and Bansi Lal, "Citrate - Nitrate route for the synthesis and characterization of TAG using sol-gel techniques," Journal of Sol-Gel Science and Technology, 41, 245, 2006.

F. Herfurth *et al*., "Masses along the rp-Process Path and Large Scale Surveys on Cu, Ni and Ga with ISOLTRAP", Nuclear Physics A, 746, 487, 2004.

Conference Proceedings and Presentations:

Sumit Saxena and Trevor A. Tyson, "Electronic Structure Studies of Graphene Oxide," Materials Research Society fall meeting 2010, Boston, MA, December 2010 (to be presented).

Sumit Saxena and Trevor A. Tyson, "Structural Study of Boron Nanoribbons," Materials Research Society fall meeting 2010, Boston, MA, December 2010 (to be presented).

Sumit Saxena, Trevor A. Tyson, Shobha Shukla, Ezana Negusse, Haiyan Chen, Jaimin Bai, and P.N. Prasad, "Atomic and Electronic Structure of Graphene Oxide," Proceedings of the American Physical Society March meeting 2010. Portland, OR, March 2010.

Sumit Saxena and Trevor A. Tyson, "Effect of Stone-Wales Defects on the Electronic Structure of Silicon Nanoribbon," Proceedings of the American Physical Society March meeting 2010, Portland, OR, March 2010.

Sumit Saxena and Trevor A. Tyson, "Role of Edge States in Graphene Nanoribbons: - DFT Studies," Proceedings of the American Physical Society March meeting 2009, Pittsburgh, PA, March 2009.

Sumit Saxena and Trevor A. Tyson, "Electronic properties of boron nano ribbons: - DFT study," Proceedings of the American Physical Society March meeting 2009, Pittsburgh, PA, March 2009.

Sumit Saxena and Trevor A. Tyson, "Pressure Induced Changes in the Atomic and Electronic Structure of Carbon Nanotubes," Proceedings of the American Physical Society March meeting 2008, New Orleans, LA, March 2008.

Sumit Saxena and Trevor A. Tyson, "Ab-initio Study of Metallic and Semi-Conducting Carbon Nanotubes," Proceedings of the American Physical Society March meeting 2007, Denver, CO, March 2007.

Sumit Saxena and Bansi Lal, “Design and Fabrication of Diode Pumped Nd: YAG Single Crystal Fiber Laser,” Proceedings of the National Laser Symposium – 4, Mumbai, India, December 2005.

Sumit Saxena, Archana Asokkumar K. and Bansi Lal, “Preparation and Characterization of Nanoscaled Terbium Aluminum Garnet by Sol-Gel Technique,” Proceedings of the National Laser Symposium – 4, Mumbai, India, December 2005.

Archana Asokkumar K., Sumit Saxena and Bansi Lal, “Preparation and Characterization of Single Crystal Fibers of MgO:LiNbO3 by Laser Heated Pedestal Growth Technique,” Proceedings of the National Laser Symposium – 4, Mumbai, India, December 2005.

“Sometimes winning is everything!!!”

This dissertation is dedicated to my parents Mr. N. K. Saxena and Smt. Mamta Saxena, my wife Dr. Shobha Shukla, my in-laws Mr. & Mrs. Ashok Kumar Shukla, my best friend Dr. Arnab Kr. Pal, and all family members and friends for their love encouragement and patience which have enabled in successful completion of this research work.

ACKNOWLEDGMENT

I would like to thank Dr. Trevor A. Tyson, my dissertation advisor, for his advisement, support and providing me work freedom in my research work. I feel highly grateful to all the committee members Dr. Joseph W. Bozzelli, Dr. Keun H. Ahn, Dr. Reginald Farrow, and Dr. Huixin He for providing useful suggestions and motivation. I would like to acknowledge the help of my wife Dr. Shobha Shukla for helping me and providing valuable contributions in performing experiments for this research work, Dr. Z. Tao and his students Eric Standard and Kwok Lo (Phil) for their help with the Raman measurements. Gracious unrestricted computational time on “HYDRA” made available through the Department of Mathematics is greatly acknowledged which enabled in computations required for this dissertation work. I would also like to thank the Department of Physics for employing me as a teaching assistant due to which I was able to take care of my living expenses during my PhD program. Last but not the least; I would like to thank Ms. Leslie Williams, Ms. Renee Crawley (Physics Department), Ms. Clarisa Gonzáles-Lenahan, Dr. Ronald Kane and Ms. Jenita Desai (Office of Graduate Studies) for their kind assistance.

TABLE OF CONTENTS

TABLE OF CONTENTS
(Continued)

Chapter **Page**

TABLE OF CONTENTS
(Continued)

Chapter **Page**

LIST OF FIGURES

LIST OF FIGURES
(Continued)

Figure **Page**

LIST OF FIGURES
(Continued)

Figure **Page**

LIST OF FIGURES
(Continued)

Figure **Page**

CHAPTER 1

INTRODUCTION

Nanotechnology was envisioned as early as 1959 by Richard Feynman [1] in his talk "There's Plenty of Room at the Bottom" at the American Physical Society meeting held at Caltech. Feynman had a clear perception of the tools required and was aware of the scaling issues that would arise due to changes in magnitude of different physical phenomenon. Carbon compounds form the basis of most, so far known life on earth. Carbon is one of the simplest elements to look on the periodic table with two valence electrons. Nanotechnology has become a buzz word and carbon nanostructures have become synonymous to nanotechnology today. Preliminary investigations have suggested that carbon based devices can be looked upon as an alternative for miniaturization of present silicon technology. Much effort has been put in this area to lay out the frame work for next generation of highly efficient and compact devices based on carbon nanostructures. These devices will feature high strength, flexibility, good conductivity and low cost production in terms of energy.

Research for carbon nanostructures was catalyzed with the discovery of Buckminsterfullerene also known as bucky ball or C_{60}, by Richard Smalley in 1985 [2] for which the Nobel Prize for Chemistry was awarded to Harold W. Kroto, Robert F. Curl and Richard E. Smalley in 1996. The pursuit of producing novel forms of carbon and exploring their properties gained further momentum with the discovery of carbon nanotubes (CNT) by Iijima in 1991 [3]. Since then the area of carbon nanostructure research have prospered with the discovery of graphene [4] and its chemical derivatives such as graphane [5] and graphene oxide (GO). The study of carbon nanostructures

such as carbon nanotubes and graphene has evolved into a one of the frontier areas of interdisciplinary research today. Since the discovery of carbon nanotubes in 1991, several theoretical and experimental studies have focused on both fundamental properties and potential applications in varied areas.

From the science perspectives, carbon nanotubes are excellent candidates to study and understand the physics of one dimensional system. Carbon nanotubes are unique nanostructures with remarkable electronic and mechanical properties. As other useful properties were discovered, interest has grown in the potential applications (Figure 1) that exploit both the electronic and mechanical properties such as nanotweezers [6], mass sensors [7] memory devices [8], molecule sensors [9], actuators and switches [10]. These results have shown that carbon nanotubes hold great promise for nanoelectromechanical systems (NEMS) application [11].

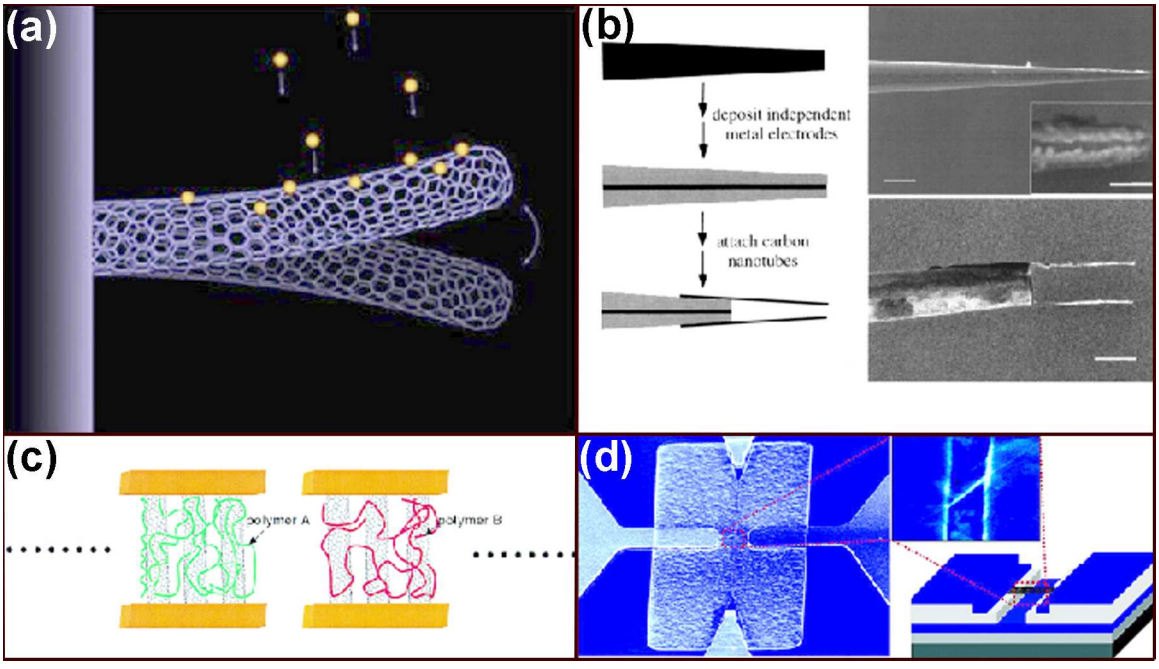

Figure 1.1 Different applications of carbon nanotubes (a) as mass sensors [6], (b) as nanotweezers [5], (c) as sensor for molecule detection [8] and (d) as switches [9].

The exploration of carbon nanotubes for biological applications is just underway. Cells do not adhere to carbon nanotubes this helps in using them as coatings for prosthetics. The ability to chemically modify the sidewalls of the carbon nanotubes also leads to biomedical applications such as vascular stents and growth as well as regeneration of neurons [12]. Carbon nanotubes have also been recently used for drug delivery applications of cancer drugs [13]. Recently carbon nanotubes are also being explored to be used as cell probes [14].

Graphene is an ideal system to study the physics of two dimensional systems. The application of graphene as sheets and nanoribbons are tremendous. Graphene nanoribbons (GNRs) can be produced by constraining one of the dimensions of the two dimensional infinite graphene sheets. Graphene and hence graphene nanoribbons have been used in fabricating electronic devices like transistors [15], resonant tunneling double barrier (RTDB) devices [16] (Figure 1.2), single molecule detection devices, transparent and conducting electrodes, ultra capacitors, and biosensors to name a few.

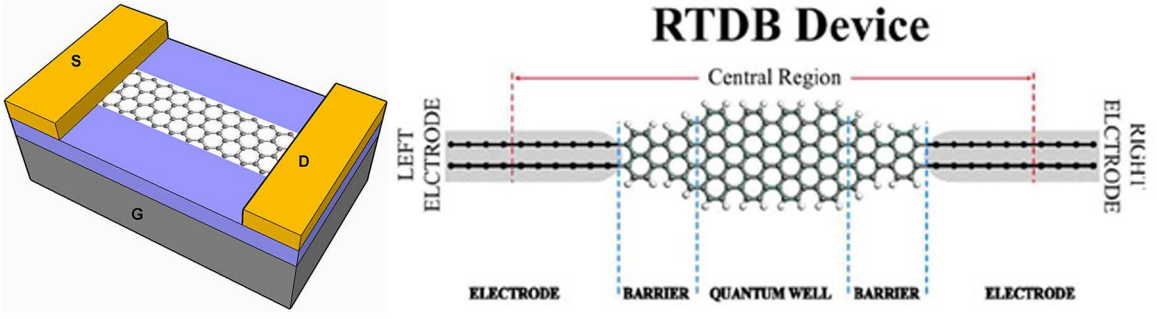

Figure 1.2 Different applications of graphene nanoribbons in devices such as FET [http://www.nanotech-now.com/news.cgi?story_id=29516]and resonant tunneling double barrier (RTDB) devices [16].

Functionalized graphene in form of recently discovered GO show unusual and exotic properties [17]. This makes it a promising materials system for fundamental

advances and an attractive platform for novel nano device technologies. GO has shown promising applications in multidisciplinary research such as transparent flexible electronic devices [18, 19], nano mechanical devices (NEMS) [20] and in delivery of water insoluble cancer drugs [21]. Recent studies have shown non-linear effects in GO samples at 532 nm in the nanosecond and picoseconds regime [22] indicating its futuristic applications in optoelectronic nano devices. Partially reduced GO samples have also demonstrated the ability to absorb gasses [23] at low concentrations, a key to nano-sensor applications. GO has also been used as precursor for large scale production of graphene by reduction [24]. The unprecedented success of using carbon as a multifunctional in different structural forms have led to the exploration of properties of other related materials for producing smart devices. Building on these results work on boron nanosystems is beginning to move forward.

Boron is a trivalent metalloid and neighbor of carbon in the periodic table. It is a fairly complex element and exists in 16 known polymorphs [25]. High pressure experiments on bulk boron samples have brought to light the occurrence of a high pressure ionic phase [26] and low temperature superconductivity [27] with a critical temperature of 6K at about 175 GPa. This element has been investigated both theoretically [28, 29] and experimentally [30] in various forms like bulk boron, nanotubes [31], clusters, and quasi planar sheets. It is used in a wide variety of applications and well known as trivalent dopant in the semiconductor industry. Boron compounds are important constituents for light structural materials, armors, insecticide and preservatives. To optimize the search for new nanosystems detailed modeling must be conducted.

Scientific computing is an inseparable and an essential part of scientific activity and can be used to predict and understand the properties or phenomenon within a given set of constraints. Density functional theory (DFT) is one of the most widely used first principles calculation technique used to investigate the structure of materials systems, in particular atoms, molecules, condensed phases and their interactions. It is a quantum mechanical theory, the conceptual roots of which can be traced back to the Thomas Fermi model developed by Thomas and Fermi in 1927. In the Kohn – Sham formulation of DFT the many electrons system is approached by replacing the interacting electrons in an external potential by non interacting electrons in an effective potential. DFT has been able to successfully predict and reproduce experimental data for many systems [32] including a few carbon nanostructures [33]. The beauty of DFT is that its formulation is exact and efficient with all the complexity hidden in the exchange correlation functional. The form of exchange correlation function holds the key to success or failure of DFT. This exchange arises from the antisymmetry due to Pauli's exclusion principle which states that for two identical fermions the wave function is antisymmetric. Despite huge success of DFT in predicting material properties, its applications suffer from pervasive errors that are not due to the breakdown of the theory itself but due to the deficiency of the exchange correlation functional. However, for many systems including carbon, specific approaches have been found to be quite reliable for atomic and electronic structure studies [34].

CHAPTER 2

CARBON NANOSTRUCTURES

2.1 Overview

Carbon is a versatile element and can exist in various nano forms as bucky ball, nanotubes, sheets and nanoribbons to name a few (Figure 2.1). Carbon atom has six electrons with two of them located in the core 1s orbital with an electronic configuration [He] $2s^2$ p^2. In complex systems, the remaining four valence electrons fill the sp^3, sp^2 or sp hybrid orbital, which are responsible for bonding in different type of structures. Three dimensional network of carbon linked by strong bonds is attributed to the sp^3 form of carbon which possesses tetrahedral geometry. The sp^2 type of hybrid orbital participate in forming layered structures such as in graphite with strong in-plane bonds and weak out of plane van der Waals (vdW) type of interactions.

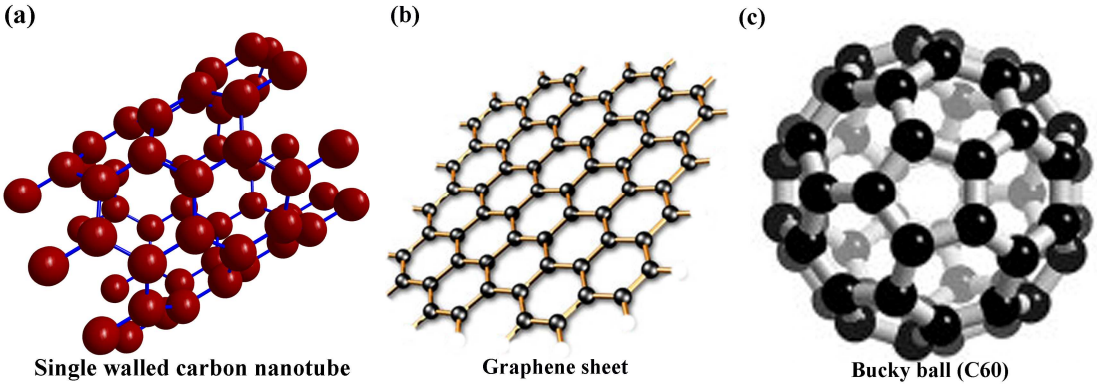

Figure 2.1 Different forms of nano scaled carbon (a) single walled carbon nanotube, (b) portion of indefinite graphene sheet, (c) Bucky ball also known as C_{60}.

Graphene is a single atom thick layer of carbon atoms packed in a honeycomb lattice and forms the basic structural element for GNR, CNT and the oxidized chemical derivative of graphene namely GO. Graphene can be visualized as periodic arrangement

of hexagonal aromatic rings. Intrinsic graphene is a semi metal or a zero band gap semiconductor. The electronic properties of GNR, CNT or GO, can be understood from band structure of graphene sheets. The unit cell of graphene honeycomb lattice is spanned by two vectors $\vec{a}_1$, $\vec{a}_1$ and contains two carbon atoms (Figure 2.2(a)) at the positions $\frac{1}{3}(\vec{a}_1+\vec{a}_2)$ and $\frac{2}{3}(\vec{a}_1+\vec{a}_2)$, where the basis vectors of length $|\vec{a}_1|=|\vec{a}_2|=a_o$=2.46Å form an angle of 60°.

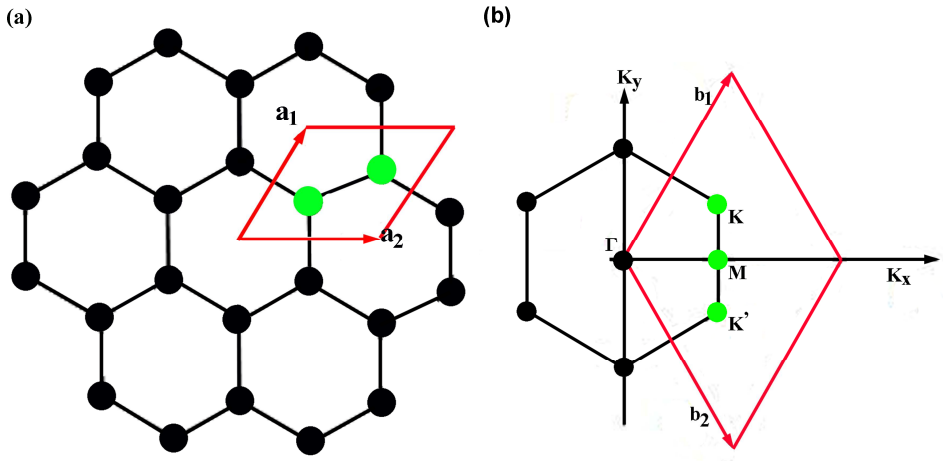

Figure 2.2 Graphene lattice showing (a) unit cell marked by red lines containing two atoms shown in green. (b) Shows the first Brillouin zone with high symmetry points marked as Γ, K and M.

This unit cell when repeated in space produces graphene sheets and is the basis for the carbon nanostructures discussed in this work. To a first approximation, the properties of carbon nanotubes are related to those of graphene. The Brillouin zone (BZ) of graphene (Figure 2.2(b)) is hexagonal and consists of high symmetry points namely the Γ, K (corner) and M (middle) points. In order to understand the electronic properties of graphene based carbon nanostructures such as single walled carbon nanotubes (SWCNTs) and GNRs a thorough understanding of tight binding (TB) model of graphene

is required, a brief overview of which is discussed below. This model provides a qualitative understanding of the electronic structure.

The valence electronic wave functions of different carbon atoms overlap when brought into close proximity on a hexagonal lattice of graphene. However, the overlap between the p_z wave functions with that of s, p_x and p_y is zero. The p_z electrons form the π bonds and can be treated independently of other valence electrons. In order to determine the electronic band structure of the π orbital, the Schrödinger equation $H\Psi(\vec{k}) = E(\vec{k})\Psi(\vec{k})$ is solved. Here $\vec{k}$ is the wave vector and the wave function $\Psi(\vec{k})$ is written as a linear combination of Bloch functions which in turn are written as linear combination of atomic wave functions. For graphene unit cell containing two atoms say A and B and the Bloch function for sublattice A is written as (where the atomic orbitals ϕ_A are centered at site A)

$$\phi_A = \frac{1}{\sqrt{N}} \sum_{R_A} e^{i\vec{k}.\vec{R}_A} \varphi(r - R_A) \tag{2.1}$$

here N is the number of unit cells and R_A is the lattice vector. The secular equation for the π orbital becomes

$$\begin{vmatrix} H_{AA}(\vec{k}) - E(\vec{k}) S_{AA}(\vec{k}) & H_{AB}(\vec{k}) - E(\vec{k}) S_{AB}(\vec{k}) \\ H^*_{AB}(\vec{k}) - E(\vec{k}) S^*_{AB}(\vec{k}) & H_{AA}(\vec{k}) - E(\vec{k}) S_{AA}(\vec{k}) \end{vmatrix}$$

with $H_{ij} = \langle \phi_i | H | \phi_j \rangle$ and $S_{ij} = \langle \phi_i | \phi_j \rangle$.

This yields the energy eigenvalues as below

$$E\left(\vec{k}\right)^{\pm} = \frac{-\left(-2E_0 + E_1\right) \pm \sqrt{\left(-2E_0 + E_1\right)^2 - 4E_2E_3}}{2E_3} \tag{2.2}$$

where

$$\begin{aligned} E_0 &= H_{AA}(\vec{k})S_{AA}(\vec{k}) & E_1 &= S_{AB}(\vec{k})H^*_{AB}(\vec{k}) + H_{AB}(\vec{k})S^*_{AB}(\vec{k}) \\ E_2 &= H^2_{AA}(\vec{k}) - H_{AB}(\vec{k})H^*_{AB}(\vec{k}) & E_3 &= S^2_{AA}(\vec{k}) - S_{AB}(\vec{k})S^*_{AB}(\vec{k}) \end{aligned} \tag{2.3}$$

The $E(\vec{k})^+$ denotes symmetric combination of wave functions and are energies of the valence band while $E(\vec{k})^-$ denote the energies of the conduction band. The assumption that the overlap of wave functions between different atoms is negligible i.e. $E_0 = H_{AA}(\vec{k}); E_1 = 0; E_2 = H^2_{AA}(\vec{k}) - H_{AB}(\vec{k}) \times H^*_{AB}(\vec{k}); E_3 = 1$, simplifies to

$$E(\vec{k})^{\pm} = H_{AA}(\vec{k}) \pm \left|H_{AB}(\vec{k})\right| \tag{2.4}$$

Considering the nearest neighbor approximation (short range approximations only) will further simplify Eq. (2.2). Under this assumption the atom interacts with itself and neighboring three carbon atoms. The matrix elements H_{IJ} and the overlap integral S_{IJ} are calculated from the Bloch functions in Eq. (2.1).

For atom at sublattice A, the matrix element H_{AA} and the overlap integral S_{AA} are

$$H_{AA}(\vec{k}) = \langle \phi_A | H | \phi_{A'} \rangle = \langle \varphi_A | H | \varphi_A \rangle = \varepsilon_{2p} \tag{2.5}$$

$$S_{AA}(\vec{k}) = \langle \varphi_A | \varphi_A \rangle = 1 \tag{2.6}$$

The value of H_{AA} is not exactly the energy of $2p_z$ states of isolated carbon atoms due to the periodic potential in the crystal Hamiltonian. For interactions of atom at sublattice A with atoms at sublattice B, the matrix element H_{AB} is given as

$$H_{AB}(\vec{k}) = \langle \phi_A | H | \phi_B \rangle = \frac{1}{N} \sum_{R_A} \sum_{R_B} e^{i\vec{k}.(\vec{R}_B - \vec{R}_A)} \langle \varphi_A | H | \varphi_B \rangle \tag{2.7}$$

The vectors $\vec{R}_{1i} = \vec{R}_{B_{1i}} - \vec{R}_A; (i = 1,2,3)$ point from A to one of its neighboring atom B_{1i} and can be written as $\vec{R}_{11} = \frac{1}{3}(2\vec{a}_1 - \vec{a}_2); \vec{R}_{12} = \frac{1}{3}(-\vec{a}_1 + 2\vec{a}_2); \vec{R}_{13} = \frac{1}{3}(-\vec{a}_1 - \vec{a}_2)$. Substituting this in Eq. 2.6 and summing over the B neighbors and the A atoms together with the fact that φ functions are radially symmetric and that the distance is the same for all three neighbors, the expression becomes

$$H_{AB}(\vec{k}) = \gamma_o \left(e^{-\frac{1}{3} i\vec{k}.(\vec{a}_1 + \vec{a}_2)} \right) \left(e^{i\vec{k}.\vec{a}_1} + e^{i\vec{k}.\vec{a}_2} + 1 \right) \tag{2.8}$$

Where γ_o is the carbon – carbon interaction energy and is written as $\gamma_o = \left\langle \varphi_A\left(\vec{r}-\vec{R}_A\right)\middle|H\middle|\varphi_B\left(\vec{r}-\vec{R}_A-\vec{R}_{11}\right)\right\rangle$. This is often also known as the tight binding integral. The overlap integral can be similarly written as follows with $s_o = \left\langle \varphi_A \middle| \varphi_{B_{1i}} \right\rangle$

$$S_{AB}(\vec{k}) = s_o\left(e^{-\frac{1}{3}i\vec{k}.(\vec{a}_1+\vec{a}_2)}\right)\left(e^{i\vec{k}.\vec{a}_1}+e^{i\vec{k}.\vec{a}_2}+1\right) \tag{2.9}$$

Inserting the overlap integral and the Hamiltonian matrix elements in Eq. (2.3) and subsequently in Eq. (2.2) the energy eigenvalues within the nearest neighbor is

$$E^{\pm} = \frac{\varepsilon_{2p} \pm \gamma_o\sqrt{f\left(\vec{k}\right)}}{1 \pm s_o\sqrt{f\left(\vec{k}\right)}} \tag{2.10}$$

where $u\left(\vec{k}\right) = 2\cos\vec{k}.\vec{a}_1 + 2\cos\vec{k}.\vec{a}_2 + 2\cos\vec{k}.\left(\vec{a}_1-\vec{a}_2\right)$ *and* $f\left(\vec{k}\right) = 3+u\left(\vec{k}\right)$. The Eq. (2.10) is widely used tight binding approximation of graphene.

2.2 Single Walled Carbon Nanotubes (SWCNTs)

SWCNTs can be considered as rolled up sheets of graphene such that graphene lattice vector $\vec{c} = n_1\vec{a}_1 + n_2\vec{a}$ becomes the circumference of the nanotube (Figure 2.3(a)). This vector also known as chiral vector is usually denoted by pair of indices $\left(n_1, n_2\right)$ and uniquely defines a particular nanotube. The chiral vector determines the structural parameters like diameter, unit cell, number of carbon atoms as well as size and shape of

the BZ. The nanotubes can be broadly classified as achiral and chiral. Achiral nanotubes consist of armchair and zigzag nanotubes for which the chiral angle θ is 30^o and 0^o. Nanotubes with chiral angle in the range $0^o < \theta < 30^o$ are termed as chiral nanotubes. The unit cell of SWCNT can be thought of as a cylindrical surface with height $a = \frac{\sqrt{3\left(n_1^2 + n_1 n_2 + n_2^2\right)}}{nR} a_o$ and diameter $d = \frac{a_0}{\pi}\sqrt{n_1^2 + n_1 n_2 + n_2^2}$. Where n is the order of the principal axis and $R = \frac{GCD(2n_1 + n_2, n_1 + 2n_2)}{n}$.

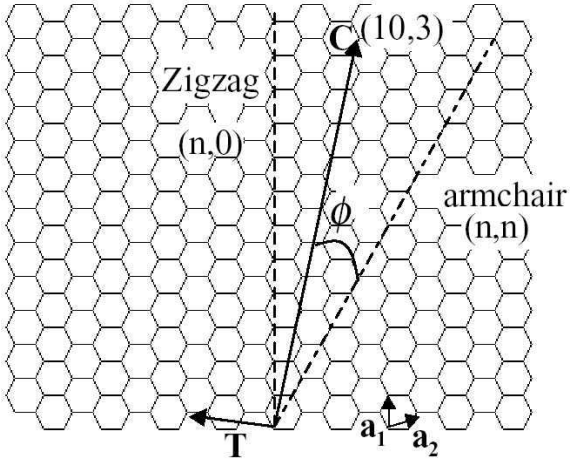

Figure 2.3 Two dimensional sheet of graphene showing the lattice vectors **a1** and **a2**, the chiral vector **C** and the translational vector **T** in the real space [35].

The reciprocal lattice vector along the length of the nanotube is given as $k_z = 2\pi/a$ where a is the translational period of the nanotube along the tube axis. Any wave vector along the circumference of the tube is expected to satisfy circular boundary conditions satisfying $m.\lambda = |\vec{c}| = \pi.d$ and $k_{\perp,m} = 2\pi/\lambda$. The quantized wave vector $\vec{k}_\perp$ and the reciprocal lattice vector $\vec{k}_z$ satisfy the conditions $\vec{k}_\perp.\vec{c} = 2\pi, \vec{k}_\perp.\vec{a} = 0$, $\vec{k}_z.\vec{c} = 0, \vec{k}_z.\vec{a} = 2\pi$.

Properties of Single Walled Carbon Nanotubes

The atoms in carbon nanotubes are bonded by σ bonds along the surface of the nanotube while the π bonds lie normal to the surface of the nanotube and are responsible for weak vdW interactions in bundles. The π states being close to the Fermi level play an important role in determining the properties of carbon nanotubes. The allowed wave vectors around the circumference of the nanotubes are quantized whereas along the axis, the wave vectors are continuous. The allowed wave vectors of the nanotube appear as series of lines parallel to the tube axis on the BZ of graphene. The length, number and orientation of these lines depend on the chiral indices (n, m) of the nanotube (Figure 2.4).

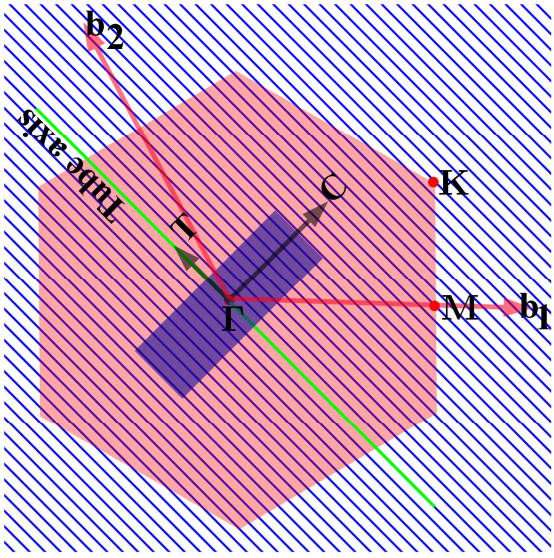

Figure 2.4 First Brillouin zone of the hexagonal lattice with superimposed cross section of the nanotube, **c** denotes the chiral vector, **T** is the translational vector along the tube axis, $\mathbf{b_1}$ and $\mathbf{b_2}$ represents the reciprocal lattice vectors.

The band structure of carbon nanotubes can be obtained to the first approximation from well known tight binding band structure of graphene by applying zone folding techniques to understand their properties. The tight binding model of graphene has shown that the valence and the conduction band of graphene cross at the K point on the BZ. If

the graphene K point is among the allowed states, the carbon nanotubes will show metallic behavior else it behaves like a semiconductor. In order to quantify this, the quantization condition $\vec{K}.\vec{c} = 2\pi m$ along the circumference of the nanotube is used, where m is an integer and $\vec{c}$ is the chiral vector of the nanotube. The K point of graphene is at $\frac{1}{3}\left(\vec{k}_1 - \vec{k}_2\right)$ thus, a nanotube will show metallic properties only if following condition is satisfied [36, 37].

$$\vec{K}.\vec{c} = 2\pi m = \frac{1}{3}\left(\vec{k}_1 - \vec{k}_2\right)\left(n_1\vec{a}_1 + n_2\vec{a}_2\right) = \frac{2\pi}{3}\left(n_1 - n_2\right) \tag{2.11}$$

Similarly, projecting the K point along the tube axis enables to determine $\vec{k}_z$ at which the valence band crosses the conduction band. Using the condition $\vec{K}.\vec{a} = 2\pi k_z$ (k_z is continuous) the following condition is finally obtain

$$k_z = \begin{cases} 0 & (n_1 - n_2)/3n \neq Integer \\ 1/3 & (n_1 - n_2)/3n = Integer \end{cases} \tag{2.12}$$

Thus, in (n, 0) metallic zigzag nanotubes the valence and the conduction band crosses at the Γ point, where as armchair (n, n) nanotubes are always metallic and the valence and the conduction bands cross each other at $2\pi/3a$.

The density of states (DOS) represent the number of available electronic states for a given energy level to be occupied. DOS enters critically in experimental verification of theoretical predictions of the properties of carbon nanotubes. Experimental verification to

test the theoretical predictions of the electronic properties of carbon nanotubes is very difficult as they strongly depend on the diameter and chirality of the nanotubes. Scanning tunneling spectroscopy (STS) can in principle be used to probe the density of states of SWCNTs. This technique also allows one to perform scanning tunneling microscopy (STM) to determine the diameter and chirality of the nanotubes at the same location. The current – voltage (I-V) measurement [38] suggested a gap in the DOS consistent with semiconducting behavior. Combined STS/ STM measurements [39] have provided preliminary but detailed test of the theory of electronic properties. These studies were further conducted by several groups [40-44] and were successfully able to characterize the peaks in the DOS. The plot of dI/dV with V for a SWCNT crudely mimics the one dimensional DOS for the nanotube and provides verification for theoretically predicted DOS.

The electronic band structure further away from the Fermi level can be measured by absorption and photoluminescence experiments. The vibrational properties are obtained using Raman scattering experiments or infrared measurements. The band structure of a semiconducting SWCNT shows kinks in the DOS plot represented by C1 and V1 belonging to different sub bands. These kinks are known as van Hove singularities (vHs) (Figure 2.5 (a)).

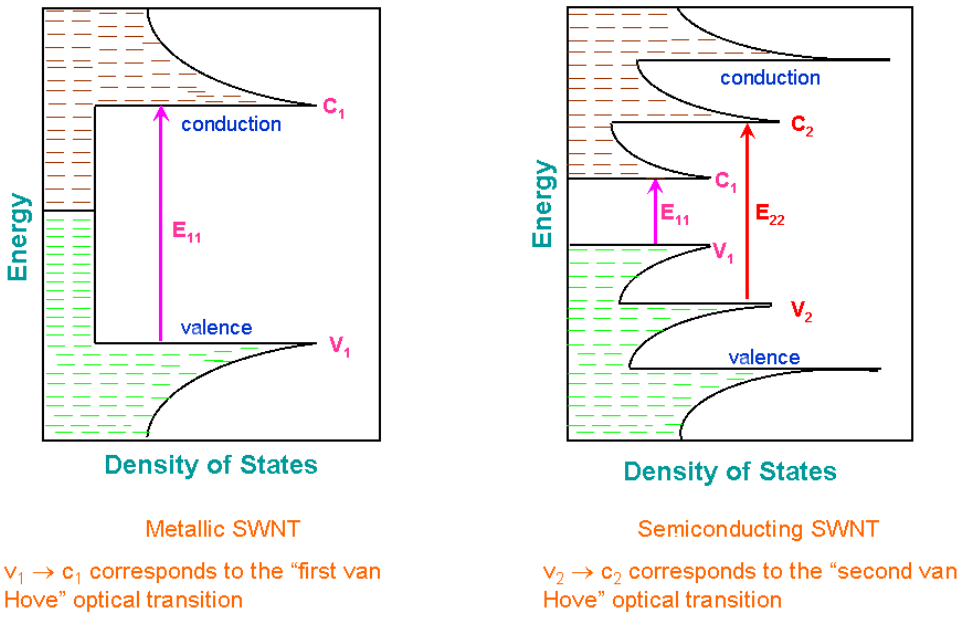

Figure 2.5 Electronic density of states plot for (a) metallic and (b) semiconducting carbon nanotube [Wikipedia].

The magnitude of the projection of the angular momentum along the tube axis is labeled by integers. The allowed dipole transitions (electric vector parallel to tube axis) promotes an electron from valence sub band to the conduction sub band conserving the angular momentum projection. The optical absorption and emission are dominated by these allowed dipole transitions. When the photon energy matches with the energy difference of the corresponding van Hove singularities, the transitions are predicted to be highly intense. Thus one expects the absorption and emission spectra to consist mainly of series of sharp features at energies E_{ii} with $i = 1, 2, 3\ldots$. For semiconducting nanotubes commonly produced (diameter ~1nm), the first three transition appear in the near infrared, visible, and ultraviolet region of the electromagnetic spectrum. These non dispersive interband optical transitions are the characteristics of diameter and chirality of the nanotube. SWCNTs also show dispersive intense near ultraviolet absorptions at 4.5 eV and 5.2 eV due to the collective plasmon excitation of their π electrons [45, 46].

However, the spectra of bulk samples containing structurally different nanotubes show broad optical absorption arising from the strongly overlapped transitions of different species. In the absence of emission, the transitions can not be assigned to van Hove singularities. a van Hove singularity is a kink in the density of the states (DOS) of a solid. The wavevectors at which van Hove singularities occur are often referred to as critical points in the Brillouin zone.

A breakthrough was obtained when nanotubes [47] synthesized by high pressure carbon monoxide (CO) conversion (HiPCO), were mechanically dispersed into aqueous solution of sodium dodecylsulphate (SDS) and processed to obtain desegregated samples [48]. These aqueous samples enriched in individual surfactant displayed near infrared photoluminescence. The peaks in their highly structured emission spectra were nearly coincident with that of the absorption spectra. This was attributed to the large number of emitting species with each contributing one dominant transition and a very small stokes shift between its absorption and emission peaks.

Spectroscopic assignment is a crucial task for identifying specific nanotube structure responsible for each peak. This was achieved using spectrofluorimetry techniques by scanning the excitation source wavelength over the range of E_{22} transitions. When the excitation energy matches the second van Hove transition energies, an electron is excited from the second valence sub-band creating a hole and an electron in the second conduction sub-band, with the absorption of photon. The electron and hole relax into their first conduction and valence sub-band by phonon emission. Subsequently a radiative recombination of electron-hole across the semiconducting band gap results in the emission spectra corresponding to the E_{11} transition energies. The variation of the

ratio of the E_{22} / E_{11} intensities with the excitation wavelengths are further analyzed in the light of extended tight binding calculations. This enables in the assignment of the observed samples to family of 'n-m' nanotubes. Raman Spectroscopy was later employed to correctly assign the (n, m) indices.

One-dimensional confinement of the electronic and phonon states cause unique optical and spectroscopic properties observed in SWCNTs. This creates strong enhancement of the resonance effect as compared to that observed in graphite and is highly selective to nanotube geometric structure. The two first order dominant Raman modes that distinguish a SWCNT from other forms of carbon are the radial breathing mode (RBM) and the multiple higher frequency features associated with the G-band modes.

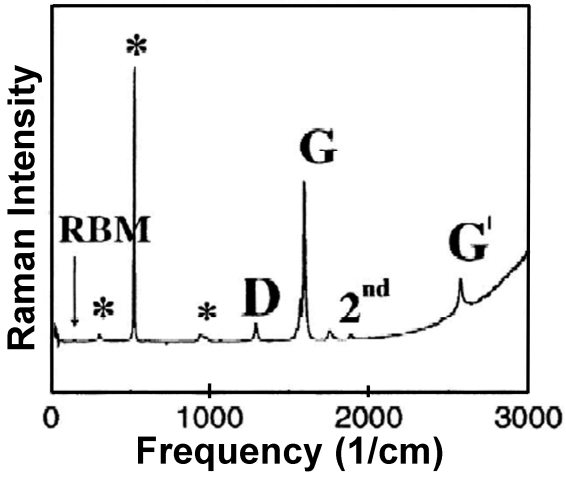

Figure 2.6 Raman spectrum for an isolated single walled carbon nanotube taken using E_{laser} = 785 nm. The features marked with * are from the Si/SiO_2 substrate [39].

These have been used to characterize the SWCNT samples [49-53]. The RBM (100 cm^{-1} – 350 cm^{-1}) correspond to the symmetric in-phase displacement of all the carbon atoms in the radial direction while the G-band (1580 cm^{-1}) corresponds to the

tangential vibrational modes (Figure 2.7). One-dimensional quantum confinement produces singularities in the DOS. Since the resonant Raman intensity depends on the DOS available for optical transitions, the power of this technique became evident when the process was shown to be highly selective of specific (n. m) SWCNTs [34, 54]. Despite the electronic structure of an (n, m) SWCNT having many van Hove Singularities (vHS), symmetry selection rules allows only a few of them to be connected by light. Electrons and phonons in carbon nanotubes characterized by their one-dimensional wave vectors are related to the number of nodes for their wave function along the circumference of the nanotube. The totally symmetric states for electrons and phonons have no nodes, while the other harmonics usually exhibit double degenerate symmetries E_μ, so for levels labeled by $\mu = 1, 2, 3.....$ the eigenvectors have $2, 4, 6, ...$ nodes. When the polarization of the electric field is parallel to the nanotube axis, valence and conduction electrons having the same symmetry $(E_\mu^v \rightarrow E_\mu^c)$ are coupled by light. However, when the polarization vector is normal to the tube axis, the absorption vanishes and couples $(E_\mu^v \rightarrow E_{\mu\pm1}^c)$.

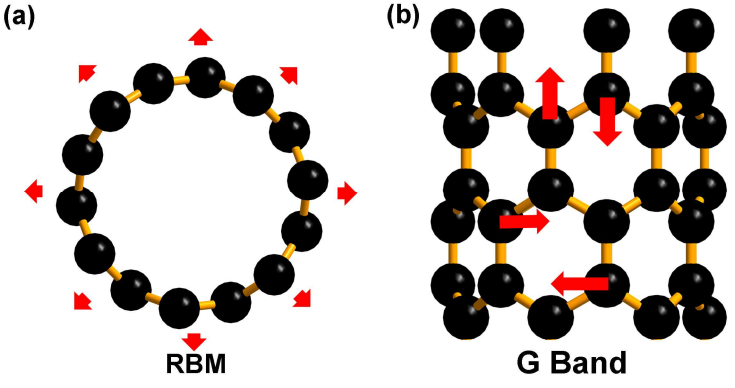

Figure 2.7 Raman modes for single walled carbon nanotube (a) RBM mode (100 cm^{-1} – 350 cm^{-1}) and (b) the G mode (1580 cm^{-1}).

Because of the selection rules, the optical transitions occur between two peaks which are almost symmetrically placed with respect to the Fermi level (Figure 2.5). It must be noted that the DOS at the Fermi level is non zero between the highest valence band vHS and lowest conduction band vHS. Since the excited electron is a bound hole that is left behind during the excitation process, the transition energies are excitonic in nature.

2.3 Graphene Nanoribbons (GNRs)

GNRs can be formed by limiting one of the dimensions of the two dimensional graphene sheets to form stripes of finite width. They may also be considered as unrolled SWCNTs [55]. Several techniques such as scanning tunneling microscope lithography [56], chemical approach [57, 58] and plasma etching of nanotubes [59] have been used to successfully produce GNRs. GNRs are expected to show a band gap due to the quantum confinement effect [60, 61]. This confinement of Dirac particles is of particular importance for the realization of nano electronic devices as it is possible to tune the electronic and optical properties [62]. Experimentally, the presence of a band gap has been observed in GNR devices [63, 64]. The edges of GNRs can be armchair, zigzag or a combination of the two. The electronic states of GNRs depend largely on the edge structures and their widths (armchair or zigzag).

The width of the nanoribbon is defined by the number of dimer lines for the armchair nanoribbon and number of zigzag lines for the zigzag nanoribbon (Figure 2.8). The global band structure of each one dimensional graphite nanoribbon can be understood by projecting the 2D graphite band along the ribbon axis.

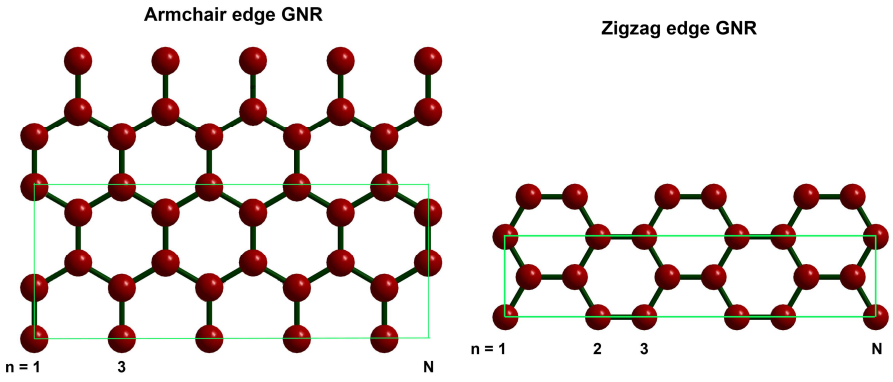

Figure 2.8 Structure of armchair edged graphene nanoribbon with 10 dimer lines indicating 10AGNR and zigzag edged graphene nanoribbon with 6 zigzag lines indicating 6ZGNR.

For armchair nanoribbons, the ribbon axis lies along the M point in the first BZ of the graphene sheet. Thus the electronic band structure of graphene can be used to understand the properties of the graphene nanoribbons.

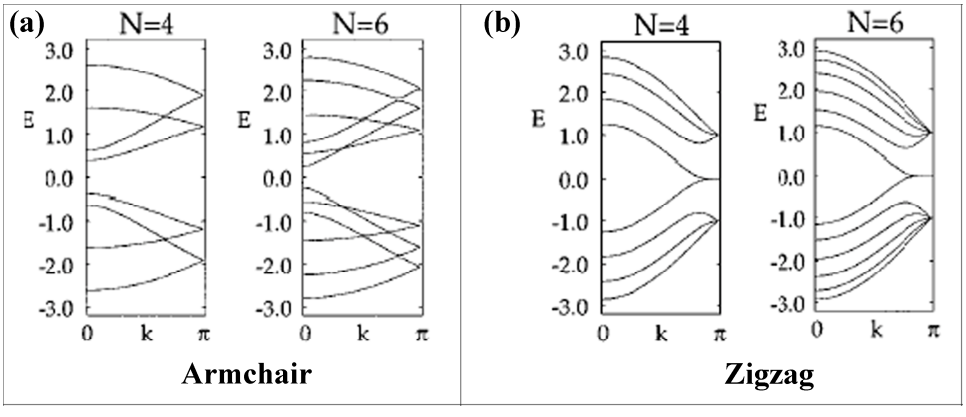

Figure 2.9 Electronic band structures for (a) armchair and (b) zigzag edged graphene nanoribbon [38].

For armchair nanoribbons, the highest valence band and the lowest conduction band lie close to the Γ point (Figure 2.9 (a)). Since the zigzag nanoribbons are metallic, the degeneracy between the valence and conduction band is expected to appear only at $k = \pm 2\pi/3$. However, the two center bands shows degeneracy at $k = \pi$ which does not

originate from the band structure of two dimensional graphene (Figure 2.9 (b). The flat bands sit steadily at the Fermi level and become flatter for wider ribbons in the range $2\pi/3 \le k \le \pi$ [65].

Properties of Graphene Nanoribbons

GNRs show a broad range of interesting properties in addition to the metallic or semiconducting behavior. In zigzag GNRs, transport is dominated by edge states. Moreover owing to their higher degeneracy, these states are expected to be spin-polarized making zigzag GNRs attractive for spintronics applications [66].

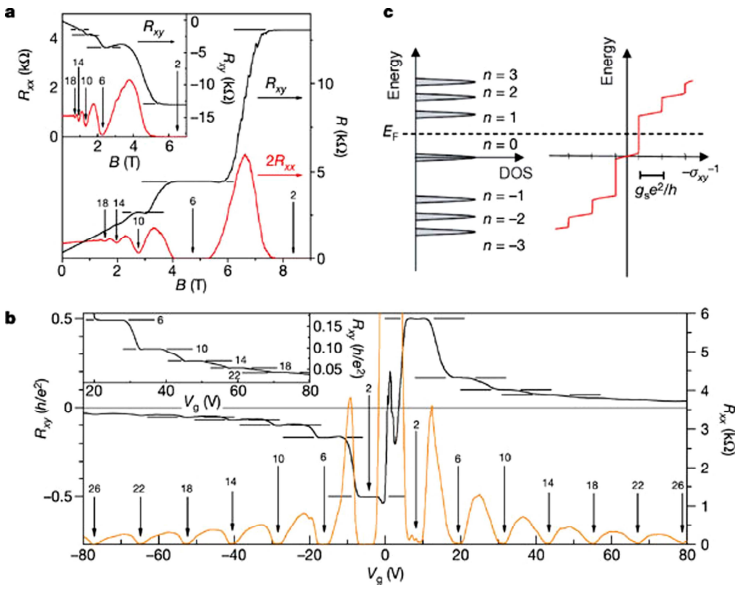

Figure 2.10 (a) Hall resistance and magnetoresistance measured at T = 30 mK and V_g = 15 V. The vertical arrows and the numbers on them indicate B and the corresponding filling factor υ of the QH states. The horizontal lines correspond to the h/e^2 υ values. The inset shows the QHE for a hole gas at V_g = -4 V measured at T = 1.6 K. (b) Hall resistance and magnetoresistance measured at T = 1.6 K and B = 9 T, measured as a function of gate voltage. The upper inset shows a detailed view of high-filling factor plateaux measured at 30 mK. (c) Schematic diagram of the landau level density of states and the corresponding quantum Hall conductance (σ_{xy}) as a function of energy. Note that in the QH states $\sigma_{xy} = -R_{xy}^{-1}$. The landau level index n is shown next to the DOS peak [48].

Recent theoretically reports have shown that the zigzag graphene nanoribbons are magnetic and can carry a spin current in the presence of a sufficiently large electric field [67]. Ideal zigzag GNRs are not efficient spin injectors due to symmetry between the edges with opposite magnetization. This symmetry must be broken in order to obtain net spin injection. Existing proposals to achieve this involves either application of very large transverse electric field or by introducing edge imperfections [68]. It has been observed experimentally that high mobility graphene samples exhibit an unusual sequence of quantum hall (QH) effects [69, 70].

In the presence of a magnetic field perpendicular ($B_\perp$) to the plane of graphene, QH plateaus at $\nu = \pm 4\left(|n| + 1/2\right)$ are observed in low magnetic fields $B_\perp < 9T$. At higher magnetic fields, a new set of QH states at $\nu = 0$, $\nu = \pm 1$ and $\nu = \pm 4$ are observed due to the magnetic field induced splitting of the $n = 0$ and $n = \pm 1$ landau levels (LL) [71]. Landau states occur only when the ribbon width is close to or greater than the distribution width of Landau wave function with the wavelength of the Landau wave function depending critically on the magnetic field as $l_B = \sqrt{h/2\pi eB}$. For graphene nanoribbons in a perpendicular magnetic field, the electron motion is confined by both the magnetic potential and the ribbon boundary. Hence in the limits of high magnetic field $l_B \propto B^{-1/2} \to 0$, the electrons are mainly confined by the magnetic potential and reproduce the landau levels of two dimensional graphene sheets. However, this holds only until the wave functions do not touch the edges. The electrons deep inside the nanoribbons execute cyclotron orbits. These orbits are disrupted when the electrons

approach the edges. This forces a competition between the quantum confinement and the magnetic confinement effect [72].

The finite width of the nanoribbons supports only symmetric or anti-symmetric eigenstates along the width of the nanoribbon. Hence the optical absorption of GNRs is qualitatively different from that of SWCNTs. Optical absorption peaks occurring due to interband transitions at direct band gap does not occur in GNRs. The edge states play an important role in optical absorption. The greatest photon energy with which the edge states can cause an absorption peak is ~0.11 au [73].

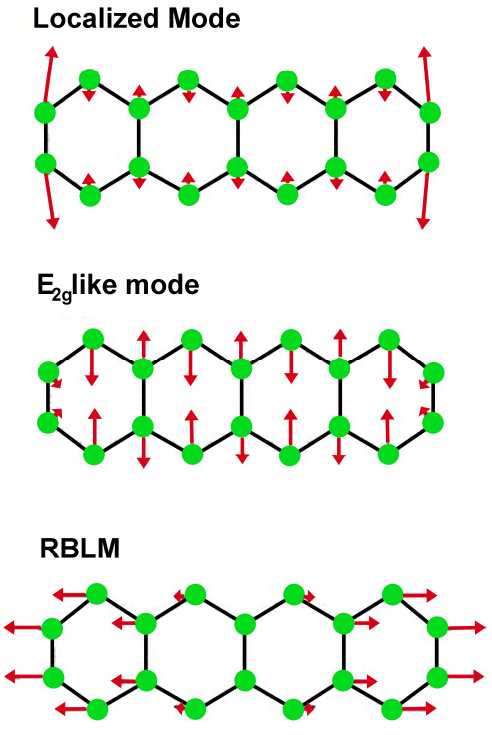

Figure 2.11 Atomic displacements of graphene nanoribbons for localized mode, E_{2g} like modes and radial breathing like modes (RBLM).

Density functional calculations have shown that for all graphene nanoribbons there are three typical Raman active modes namely the radial breathing like mode (RBLM ~250 – 650 cm^{-1}), the localized mode (~2000 cm^{-1}), and the graphene E_{2g} (~1580

cm^{-1})like modes. The low frequencies of the RBLM modes are understood to occur due to the relative movement of the left and right parts of the GNR. The frequencies of the RBLM decreases with the increasing width of GNR and may be used to characterize the width of GNRs. Besides the RBLM's and the graphene E_{2g} like modes, GNRs also show high frequency localized vibrational modes of the edge carbon atoms. Since the edge bonds of zigzag graphene nanoribbons (ZGNRs) are slightly shorter than that of the armchair graphene nanoribbons (AGNR), the vibrational modes are expected to occur at lower energies [74].

2.4 Graphene Oxide (GO)

Graphene oxide derives its origin from graphite oxide which was first prepared by treating graphite with mixture of potassium chlorate and fuming nitric acid [75]. Later on it was prepared using a mixture of H_2SO_4, $NaNO_3$, and $KMnO_4$ [76]. Graphite oxide is understood to be a layered material consisting of hydrophilic oxygenated graphene sheets. Recent reports have shown the fabrication of graphene oxide paper as well [17]. Microwave heating for pre-exfoliation of graphite has been used to produce large area monolayer GO samples [77]. It has been shown that under suitable conditions graphene oxide can undergo complete exfoliation in water producing suspensions of individual GO sheets [78, 79]. GO has been successfully suspended in solvents like dimethylformamide (DMF). It has been reported that addition of N-methylpyrrolidone (NMP), ethanol, dimethylsulfoxide (DMSO) and acetonitrile to aqueous suspension of GO produces stable homogenous colloidal suspensions of GO sheets. Addition of Acetone and tetrahydrofuran (THF) created suspensions of GO, however, particles visible to eyes were

observed after a day. GO tends to agglomerate and precipitate by addition of diethylether or toluene to the aqueous solution [80]. Atomic force microscopy (AFM) experiments have suggested the vertical stacking of GO sheets in multiples of 1.1 nm. This height has been assigned to individual graphite sheets bearing oxygen containing groups on both sides of the graphene sheet [81].

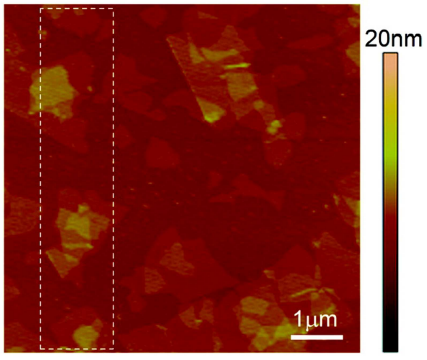

Figure 2.12 AFM images of graphene oxide sample [82].

AFM images of GO monolayers on atomically flat surfaces have shown pronounced roughness which has been accounted due to the sp^3 centers and point defects in the carbon lattice also causing wrinkling of sheets at nano-scale [83]. It should be noted that in the reverse process, GO may be deoxygenated under alkaline conditions to produce highly pure graphene sheets [24].

Properties of Graphene Oxide

GO has been characterized using various optical and transport measurements. Individual graphene oxide sheets have been characterized electrically [84]. GO monolayers deposited on doped silicon substrate with thermally grown SiO_2 layer (200nm thick), chemically reduced, and then contacted by e beam lithographically defined Au/Pd (60/40)

electrodes (300 – 1000 nm separation) show almost insulating behavior with differential conductivity values of 1-5 x 10^{-3} S/cm at a bias voltage of about 10V (assuming layer thickness of 1 nm).

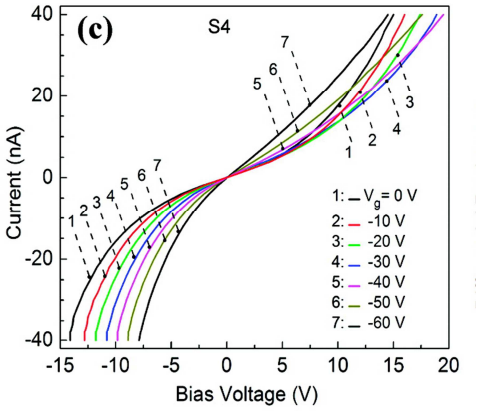

Figure 2.13 Current – Voltage (I-V) curve for graphene oxide device at different negative gate voltages [63].

Chemical reduction result in increase of conductivity (85). Non-linear optical properties of GO measured using Z-scan technique have revealed that at low intensities of $2.1\times10^{9}\,W/cm^{2}$ the normalized transmission curve shows a symmetrical peak with respect to the focus (z=0), indicating that saturable absorption (SA) dominates nonlinear absorption (NLA) mechanism. Increasing the input intensities, a valley between the peak appeared indicating reverse saturable absorption (RSA) or two photon absorption (TPA) appears following SA and finally NLA transition (22).

CHAPTER 3

THEORETICAL METHODS

3.1 Theoretical Developments

Within three years of the discovery of the electron by J. J. Thomson in 1897 [86], Drude [79] constructed his theory of electrical and thermal conduction based on kinetic theory of gasses for metals. The kinetic theory was applied to the conduction electrons moving against a background of heavy immobile ions. The two most significant results of Drude's model were electronic equation of motion $\frac{d}{dt}\vec{P}(t) = qE - \frac{\vec{P}(t)}{\tau}$ and linear relationship between the current density J and Electric field E, $J = \left(\frac{nq^2\tau}{m}\right)E$. The major assumptions involved were the independent particle approximation, and the free electron approximation [87].

Arnold Sommerfeld combined the classical Drudes model with quantum mechanical Fermi-Dirac statistics [88] to explain the properties in metals. Although the Free electron theory eliminated some deficiencies, the model still makes many quantitative predictions contradicted by observations. This model fails to distinguish between metals, semimetals, semiconductors and insulators; occurrence of positive values of Hall coefficients; the relation of conduction electrons in the metal to valence electrons of free atom and transport properties.

In free electron model, the allowed energy values are distributed essentially continuously from zero to infinity. The band structure of a crystal can be explained by the nearly free electron model in which the band electrons are treated as perturbed weakly by

the periodic potential of the ion core. This takes care of the interactions between the conduction electrons and the ion cores. This model like the free electron model does not take into account electron-electron interactions. This leads to the examination of general properties of the Schrödinger equation for single electron $H\psi = \left(-\frac{h^2}{8\pi^2 m}\nabla^2 + U(r) \right)\psi = \varepsilon\psi$ with the development of quantum mechanics in the 1920s.

A very different point of view can be taken by considering a solid as a collection of weakly interacting neutral atoms. The tight binding approximation deals with the case in which the overlap of atomic wave functions is enough to require corrections to the picture of isolated atoms, but not so much as to render the atomic description irrelevant.

3.2 The Tight Binding Method

The hallmark of this approach is that the wave function can be expanded as linear combination of the atomic orbitals each associated with a specific atom in a molecule or crystal. The advantages of this method are that not only does it provides a simplistic understanding of the fundamental features of electronic bands but also one assumes a form for the Hamiltonian and the overlap matrix elements without actually specifying anything about the orbitals except their symmetry [89, 90].

It is assumed that in the vicinity of each lattice point the full periodic crystal Hamiltonian (H) and can be approximated by the Hamiltonian of a single atom H_{at}. It is also assumed that the bound levels of H_{at} are unchanged. The extreme case would be when the crystal Hamiltonian differs from the atomic Hamiltonian at distances that exceed the range of the atomic wave function. Hence the atomic wave functions $\psi_n(\vec{r})$

would be an excellent approximation. Considering a Bravais lattice with translational vector $\vec{R}$, the wave function would be written as $\psi_n\left(\vec{r}-\vec{R}\right)$. Considering the corrections to the atomic Hamiltonian to produce the full periodic potential of the crystal to be $\Delta U(\vec{r})$, the crystal Hamiltonian can be written as $H = H_{at} + \Delta U(\vec{r})$. If $\Delta U(\vec{r})$ vanishes whenever $\psi_n(\vec{r})$ does not, then each atomic level would yield N levels in the periodic potential with wave function $\psi_n\left(\vec{r}-\vec{R}\right)$ for each of N sites in the Bravais lattice. The N linear combinations of these degenerate wave functions that satisfy the Blöch condition are $\psi_{n\vec{k}}(\vec{r}) = \sum_{\vec{R}} e^{i\vec{k}.\vec{R}}\psi_n\left(\vec{r}-\vec{R}\right)$ where the $\vec{k}$ ranges through the N values in the first BZ satisfying the Born-von Karmon periodic boundary conditions. The energy bands obtained are reminiscent of the atomic levels. An improvement towards a more realistic approach would to be to consider $\psi_n(\vec{r})$ small and not exactly zero as $\Delta U(\vec{r})$ becomes appreciable. In this case the solution $\psi_n(\vec{r})$ to the full crystal Schrödinger equation, satisfying the Blöch conditions can be written as a linear combination of some functions $\phi(\vec{r}-\vec{R})$ which are not atomic wave functions but are linear combination of the atomic wave functions $\psi_n(\vec{r})$ i.e. $\psi(\vec{r}) = \sum_{\vec{R}} e^{i\vec{k}.\vec{R}}\phi_n\left(\vec{r}-\vec{R}\right)$ where $\phi(\vec{r}) = \sum_n b_n\psi_n(\vec{r})$. The full crystal Schrödinger equation using the modified wave function is attempted to solve as below.

$$H|\psi\rangle = (H+\Delta U)|\psi\rangle = \varepsilon\left(\vec{k}\right)|\psi\rangle \tag{3.1}$$

By multiplying the crystal Schrödinger equation by the atomic wave function $\psi_m^*(\vec{r})$ and solving the following is obtained

$$\begin{aligned}\langle\psi_m|H|\psi\rangle &= \langle\psi_m|H_{at}+\Delta U|\psi\rangle \\ &= \langle\psi_m|H_{at}|\psi\rangle+\langle\psi_m|\Delta U|\psi\rangle \\ &= \langle\psi_m|H_{at}|\psi\rangle+\langle\psi_m|\Delta U|\psi\rangle = \langle\psi_m|\varepsilon|\psi\rangle\end{aligned}$$

$$E_m\langle\psi_m|\psi\rangle+\langle\psi_m|\Delta U|\psi\rangle=\varepsilon(\vec{k})\langle\psi_m|\psi\rangle$$

$$\langle\psi_m|\Delta U|\psi\rangle=(\varepsilon(\vec{k})-E_m)\langle\psi_m|\psi\rangle \tag{3.2}$$

Using the orthonormality condition of the atomic wave functions $\langle\psi_m|\psi_n\rangle=\delta_{mn}$ and $\psi(\vec{r})=\sum_{\vec{R}}e^{i\vec{k}.\vec{R}}\phi_n(\vec{r}-\vec{R})$ an eigenvalue equation is obtained that determines the coefficients $b_n(k)$ and the Bloch energies $\varepsilon(k)$ as

$$\begin{aligned}\left(\varepsilon(\vec{k})-E_m\right)b_m = &-\left(\varepsilon(\vec{k})-E_m\right)\sum_n\left(\sum_{\vec{R}\neq 0}\int\psi_m^*(\vec{r})\psi_n(\vec{r}-\vec{R}).e^{i\vec{k}.\vec{R}}d\vec{r}\right)b_n \\ &+\sum_n\left(\int\psi_n^*(\vec{r})\Delta U(\vec{r})\psi_n(\vec{r})d\vec{r}\right)b_n \\ &+\sum_n\left(\sum_{\vec{R}\neq 0}\int\psi_m^*(\vec{r})\Delta U(\vec{r})\psi_n(\vec{r}-\vec{R}).e^{i\vec{k}.\vec{R}}d\vec{r}\right)b_n\end{aligned} \tag{3.3}$$

The above theory has been formulated for a monatomic basis. In solids that are not monatomic Bravais lattices as in hexagonal lattices, one constructs linear combination

of atomic levels centered at the Bravais lattice points and at the basis points. The electronic levels so obtained are within the independent electron approximation. The independent approximation fails when it gives at least one partially filled band that derives from the well localized atomic levels with small overlap integrals. This might tend to fail when dealing with d and f shells in metals. This constitutes the well known electron correlation problem requiring multiple particle treatments.

3.3 Density Functional Theory

The problem of electrons in a solid is a many body problem hence a more accurate way would be based on solving the many body Schrödinger equation for a general system containing M nuclei and N electron. As a convention the position of the nuclei is denoted by $\vec{R}$ while those of the electrons by $\vec{r}$. The Schrödinger equation for such a system can be written as $H(R,r)\Psi(R,r) = E\Psi(R,r)$, where the Hamiltonian is written as

$$H(R,r) = \left(-\frac{\hbar^2}{2}\sum_{A}^{M}\frac{\nabla^2}{Mn_A}\right) + \left(-\frac{\hbar^2}{2}\sum_{i}^{N}\frac{\nabla^2}{m_i}\right) + \left(-\sum_{i}^{N}\sum_{A}^{M}\frac{Z_A e^2}{|r_i - R_A|}\right) + \left(\frac{1}{2}\sum_{i\neq j}\frac{e^2}{|r_i - r_j|}\right) + \left(\frac{1}{2}\sum_{A\neq B}\frac{Z_A Z_B e^2}{|R_A - R_B|}\right)$$

The above equation is an eigenvalues equation in 3N+3M independent variables which is in general impossible to solve exactly and needs approximations. Born and Oppenheimer in 1927 proposed that the molecular wave function can be separated into the electronic and nuclear components i.e. $\Psi(r,R) = \psi(r;R)\bullet\chi(R)$. This enables the separation of the molecular Schrödinger equation into one equation for the electronic wave

function $\psi(r;R)$ and other for nuclear wave function $\chi(R)$. The physical idea behind this is that the electrons move much faster than the nuclei, so for a given set of nuclear position the electrons adjust their positions immediately before the nuclei move. The independent variables in $\psi(r;R)$ are the coordinates of the electrons r, however, $\psi(r;R)$ depends parametrically on nuclear coordinates R thus implying that the electronic Schrödinger equation has to be solved for given nuclear geometry. The electrons can be thought of as moving in the effective instantaneous potential of the nuclei while interacting with each other. The approximation fails in systems with strong electron lattice interactions such as transition metal maganites. Thus the electronic structure can be studied by working with the electronic Hamiltonian written as

$$H = \left(-\frac{\hbar^2}{2}\sum_{i}^{N}\frac{\nabla^2}{m_i}\right) + \left(-\sum_{i}^{N}\sum_{A}^{M}\frac{Z_A e^2}{|r_i - R_A|}\right) + \left(\frac{1}{2}\sum_{i\neq j}\frac{e^2}{|r_i - r_j|}\right) \tag{3.4}$$

With the Hamiltonian figured out it is required to find out an approximate solution to the electronic Schrödinger equation $H\psi = E\psi$. The approximate solution is obtained by applying variational methods by minimizing $\frac{\langle\psi|H|\psi\rangle}{\langle\psi|\psi\rangle}$ to seek lowest estimate of the ground state energy given a choice of wavefunction. Hartree in 1927 offered one way of constructing the approximate wave function in terms of individual orbitals φ_i such that $\psi(\vec{x}_1, \vec{x}_2, \cdots \vec{x}_N) = \varphi_1(\vec{x}_1)\bullet\varphi_2(\vec{x}_2)\cdots\varphi_N(\vec{x}_N)$, where $\vec{x}_i$ include the position coordinates and spin. Applying the variational principles to $\langle\psi|H|\psi\rangle$ would

mean imposing $N(N-1)/2$ constraints due the orthonormality constraints $\langle \varphi_i | \varphi_j \rangle = \delta_{ij}$ of the orbitals. These constraints can be incorporated by considering the quantity

$$F = \langle \psi | H | \psi \rangle - \sum_{i,j} \lambda_{ij} \left[\langle \varphi_i | \varphi_j \rangle - \delta_{ij} \right] \tag{3.5}$$

and requiring that any of the derivatives of the quantity F with respect to any one of the Lagrange multipliers λ_{ij} be zero. This leads to Hartree equations which in principle determine the orbitals φ_i. The major drawback of Hartree theory is that it does take into account the indistinguishability of the electrons, thus violates the fundamental principles of quantum mechanics (Pauli's Exclusion Principle).

In order to satisfy the antisymmetry condition, the approximate wave function constructed by Hartree is improved by writing an antisymmetrized determinant wave function for a fixed number N of electrons. This is also known as the Slater determinant and written as

$$\psi = \frac{1}{\sqrt{N!}} \begin{vmatrix} \varphi_1(\vec{x}_1) & \varphi_2(\vec{x}_1) & \cdots & \varphi_N(\vec{x}_1) \\ \varphi_1(\vec{x}_2) & \varphi_2(\vec{x}_2) & \cdots & \varphi_N(\vec{x}_2) \\ \vdots & \vdots & \ddots & \vdots \\ \varphi_1(\vec{x}_N) & \varphi_2(\vec{x}_N) & \cdots & \varphi_N(\vec{x}_N) \end{vmatrix} \tag{3.6}$$

This Hartree – Fock approximation, like the Hartree approximation relies on the approximation of independent particles but still contains a major part of the physics and

is useful. So far the attempt has been to solve the Schrödinger equation more or less accurately. The approximate solution is an N-electron wave function which depends on 3N position-space co-ordinates and N spin co-ordinates. This function becomes extremely complex even for medium sized systems and can be solved only for simple electron systems such as H_2 [91].

In 1927 Thomas and Fermi working independently used a statistical model to approximate the distribution of electrons in an atom. Their formulation in terms of electron density was independent of wave function theory. In the original Thomas – Fermi method, the kinetic energy of the electrons is approximated as an explicit functional of the density, idealized as non interacting electrons in a homogenous gas with density equal to the local density at any given point. This however, was the major error within the Thomas – Fermi approach because the kinetic energy represents a substantial portion of the total energy of the system so even small error could prove to be disastrous. Both Thomas and Fermi neglected exchange and correlation among the electrons which was later incorporate by Dirac in 1930. It resulted in an atomic structure without radial shells. Although Thomas – Fermi model is considered as the basis to the modern density functional theory, the famous Hohenberg – Kohn theorem put DFT [92] on firm theoretical standing.

The approach of Hohenberg and Kohn [93] was to formulate density functional theory as an exact theory of many-body system for the ground state system. Hohenberg – Kohn formulated a universal functional $F\left[n(\vec{r})\right]$ of interacting electrons in an external potential $V_{ext}(\vec{r})$ such that the functional $E\left[n(\vec{r})\right] = F\left[n(\vec{r})\right] + \int n(\vec{r}) V_{ext}(\vec{r})\, d\vec{r}$ is

minimized by the density $n(\vec{r})$ and the minimum value of the functional E_0 is the ground state energy. The two theorems formulated by Hohenberg and Kohn are as follows:

Theorem I For any system of interacting particles in an external potential $V_{ext}(\vec{r})$, the potential $V_{ext}(\vec{r})$ is determined uniquely, except for a constant, by the ground state particle density $n_0(\vec{r})$ [94].

Theorem II The universal functional for the energy $E[n]$ in terms of the density $n(\vec{r})$ can be defined, valid for any external potential $V_{ext}(\vec{r})$. For any particular $V_{ext}(\vec{r})$, the exact ground state energy of the system is the global minimum value of this functional and the density $n(r)$ that minimizes the functional is the exact ground state density $n_0(r)$ [94].

Kohn – Sham developed methods for treating inhomogeneous system of interacting electrons [95]. These methods are exact for systems of slowly varying or high density and for the ground state, lead to self consistent equations analogous to the Hartree and Hartree – Fock equations. The exchange and correlation portions of the chemical potential of a uniform electron gas appear as an additional effective potential. Kohn and Sham separated $F\left[n(\vec{r})\right]$ into three distinct parts, so that the functional E becomes (use Hartree units $\hbar = m_e = e = 4\pi/\varepsilon_0 = 1$).

$$E\left[n(\vec{r})\right] = T_s\left[n(\vec{r})\right] + \frac{1}{2}\iint \frac{n(\vec{r}')n(\vec{r})}{\left|\vec{r}-\vec{r}'\right|} d\vec{r}' d\vec{r} + E_{XC}\left[n(\vec{r})\right] + \int n(\vec{r}) V_{ext}(\vec{r})\, d\vec{r} \qquad (3.7)$$

The kinetic energy of the non interacting electron gas with density $n(\vec{r})$ is defined as

$$T_s\left[n(r)\right] = -\frac{1}{2}\sum_{i=1}^{N}\int \psi_i^*(\vec{r})\nabla^2\psi(\vec{r})d\vec{r} \tag{3.8}$$

Variational minimization of $E\left[n(\vec{r})\right]$ and introduction of normalization constraint of electron density gives

$$\begin{aligned}&\frac{\delta}{\delta n(\vec{r})}\left[E\left[n(\vec{r})\right]-\mu\int n(\vec{r})\,d\vec{r}\right]=0\\ &\Rightarrow \frac{\delta}{\delta n(\vec{r})}E\left[n(\vec{r})\right]=\mu\end{aligned} \tag{3.9}$$

The above equation may be written in terms of an effective potential, $V_{eff}(\vec{r})$ as

$$\frac{\delta T_s\left[n(\vec{r})\right]}{\delta n(\vec{r})}+V_{eff}(\vec{r})=\mu \tag{3.10}$$

The effective potential and the potential due to exchange correlation is defined as

$$V_{eff}(\vec{r}) = V_{ext}(\vec{r}) + \int\frac{n(\vec{r})}{\left|\vec{r}-\vec{r}'\right|}d\vec{r} + V_{XC}(\vec{r})\ and\ V_{XC}(\vec{r}) = \frac{\delta E_{XC}\left[n(\vec{r})\right]}{\delta n(\vec{r})} \tag{3.11}$$

The Kohn – Sham method provides an exact method for finding the exact ground state energy of the interacting system. However, the drawback of this method is that the form of exchange correlation potential is usually unknown except for simple atoms. For practical calculations, the exchange correlation is approximated either within the local density approximation (LDA) or generalized gradient approximation (GGA) [96, 97]. Recently, the exchange correlation has been approximated within the meta generalized gradient approximation (meta-GGA), this uses the Laplacian (second derivative) of the density of the density or the kinetic energy density in addition to density and magnitude of the gradient of the density [98].

3.3.1 Local Density Approximation (LDA)

The Kohn – Sham (KS) equations while exactly incorporating the kinetic energy functional $T_s\left[n(\vec{r})\right]$, still leaves the exchange correlation functional $E_{XC}\left[n(\vec{r})\right]$ unsettled. An explicit form of the exchange correlation functional is required to solve the KS equations. Since the kinetic energy is treated rigorously in the KS formalism, the uniform electron gas formalism may be used for the unknown part of rest of the energy functional. Within the local density approximation (LDA), the exchange correlation energy of an electronic system is constructed by assuming that the exchange correlation energy per electron at a point $\vec{r}$ in the electron gas is equal to the exchange correlation energy per electron in a homogenous electron gas that has the same density as the electron gas at point $\vec{r}$. This approximation thus ignores corrections to the exchange correlation energy at point $\vec{r}$ due to inhomogenities.

The Exchange correlation functional under the LDA can be written in terms of homogenous electron gas density $n(\vec{r})$ can be written as

$$E_{XC}^{LDA}\left[n(\vec{r})\right]=\int \varepsilon_{XC}\left(n(\vec{r})\right)n(\vec{r})\,d\vec{r} \tag{3.12}$$

here $\varepsilon_{XC}\left(n(\vec{r})\right)$ is the exchange and correlation energy per particle of a homogenous electron gas density. The corresponding exchange correlation potential then becomes

$$V_{XC}^{LDA}=\frac{\delta E_{XC}^{LDA}}{\delta n(\vec{r})}=\varepsilon_{XC}\left(n(\vec{r})\right)+n(\vec{r})\frac{\delta\varepsilon_{XC}\left(n(\vec{r})\right)}{\delta n(\vec{r})} \tag{3.13}$$

substituting this in the KS equation, the Kohn – Sham local density approximation (KSLDA) which is referred to in the literature as the LDA method. The energy $\varepsilon_{XC}\left(n(\vec{r})\right)$ can be decomposed into exchange and correlation parts as

$$\varepsilon_{XC}\left(n(\vec{r})\right)=\varepsilon_{X}\left(n(\vec{r})\right)+\varepsilon_{C}\left(n(\vec{r})\right) \tag{3.14}$$

LDA is surprisingly accurate and produce good results for systems with slowly varying charge densities. LDA has a tendency to favor more homogenous systems and over binds molecules and solids. In weakly bonded systems these errors are large and bonds lengths are too short [94].

3.3.2 Local Spin Density Approximation [LSDA]

The local spin density approximation is the generalization of the local density approximation in which the spin degree of freedom is treated in a non trivial way. The exchange correlation functional within the LSDA is written as

$$E_{XC}^{LSDA}\left[n^{\uparrow}(\vec{r}),n^{\downarrow}(\vec{r})\right]=\int d^{3}\vec{r}\; n(\vec{r})\,\varepsilon_{XC}\left(n^{\uparrow}(\vec{r}),n^{\downarrow}(\vec{r})\right)$$

where (3.15)

$$n(\vec{r})=n^{\uparrow}(\vec{r})+n^{\downarrow}(\vec{r})$$

The energy $\varepsilon_{XC}\left(n^{\uparrow}(\vec{r}),n^{\uparrow}(\vec{r})\right)$ can be decomposed into exchange and correlation parts similar to the local density approximation as

$$\varepsilon_{XC}\left(n^{\uparrow}(\vec{r}),n^{\downarrow}(\vec{r})\right)=\varepsilon_{X}\left(n^{\uparrow}(\vec{r}),n^{\downarrow}(\vec{r})\right)+\varepsilon_{C}\left(n^{\uparrow}(\vec{r}),n^{\downarrow}(\vec{r})\right) \quad (3.16)$$

The LSDA can be formulated in terms of either two spin densities $n^{\uparrow}(\vec{r})$ and $n^{\downarrow}(\vec{r})$, or the total density $n(\vec{r})$ and the fractional spin polarization $\zeta(\vec{r})=\dfrac{n^{\uparrow}(\vec{r})-n^{\downarrow}(\vec{r})}{n(\vec{r})}$ [94].

3.3.3 Generalized Gradient Approximation (GGA)

The first step beyond the local density approximation is a functional of the magnitude of the gradient of the density $\left|\nabla n(\vec{r})\right|$ as well as the value of $n(\vec{r})$ at each point. Such a gradient expansion approximation (GEA) was suggested by Kohn and Sham and developed further by Herman [99]. The GEA did not lead to consistent improvement over

the LSDA. The basic problem with GEA is that the gradient in real materials is so large that the expansion breaks down.

Generalized gradient expansion (GGA) modifies the behavior at large gradients in such a way to preserve desired properties. The functional of the generalized form is represented as

$$\begin{aligned} E_{XC}^{GGA}\left[n^{\uparrow}(\vec{r}),n^{\downarrow}(\vec{r})\right] &= \int d^3\vec{r}\; n(\vec{r})\varepsilon_{xc}\left(n^{\uparrow}(\vec{r}),n^{\downarrow}(\vec{r}),\left|\nabla n^{\uparrow}(\vec{r})\right|,\left|\nabla n^{\downarrow}(\vec{r})\right|,\cdots\right) \\ &= \int d^3\vec{r}\; n(\vec{r})\varepsilon_X F_{xc}\left(n^{\uparrow}(\vec{r}),n^{\downarrow}(\vec{r}),\left|\nabla n^{\uparrow}(\vec{r})\right|,\left|\nabla n^{\downarrow}(\vec{r})\right|,\cdots\right) \end{aligned} \tag{3.17}$$

here ε_X is the exchange energy of the unpolarized homogenous electron gas and F_{XC} is dimensionless. Working in terms of dimensionless reduced density gradients of mth order defined by

$$s_m = \frac{\left|\nabla^m n(\vec{r})\right|}{(2k_F)^m n} = \frac{\left|\nabla^m n(\vec{r})\right|}{2^m\left(3\pi^2\right)^{m/3}\left(n(\vec{r})\right)^{(1+m/3)}} \tag{3.18}$$

where $k_F = 3(2\pi/3)^{1/3} r_s^{-1}$ and s_m is proportional to the mth-order fractional variation in density normalized to the average distance between the electrons r_s. The lowest order terms in the expansion of F_X has been calculated analytically as

$$F_X = 1 + \frac{10}{81}s_1^2 + \frac{146}{2025}s_2^2 + \cdots \tag{3.19}$$

Numerous forms of $F_X\left(n(\vec{r}),s\right)$ have been proposed. The three widely used forms are by Becke (B888) [100], Perdew and Wang (PW91) [101], and Perdew, Burke and Enzerhof (PBE) [102]. The implementation of the LSDA method requires specific computational frameworks. The all electron and pseudopotential methods are two approaches.

3.4 Plane Wave Pseudopotential Method

The plane wave pseudopotential method is a reliable tool to study the properties of a broad class of materials. This method uses plane wave expansion of the Blöch functions. The advantages of plane wave basis set are that there is no basis set superposition error, the periodic boundary conditions are trivially implemented, the forces can be obtained easily, the calculation of the Hamiltonian matrix elements is fast and plane waves are eigenfunctions of the kinetic energy operator.

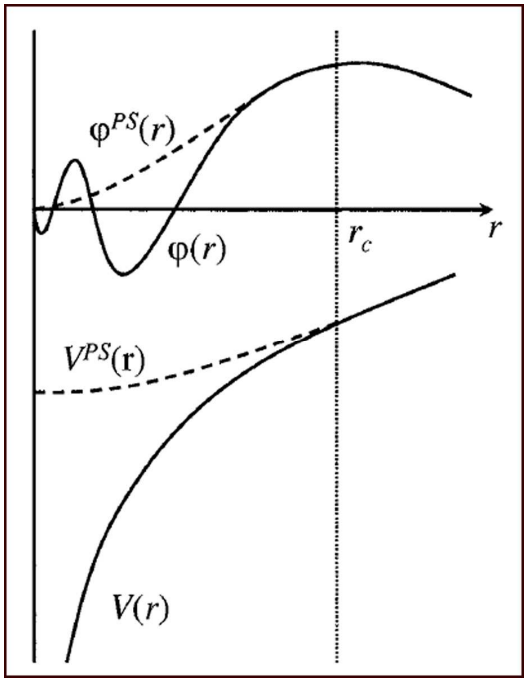

Figure 3.1 Schematic illustration of the replacement of the all electron wavefunction and core potential by pseudo wavefunction and pseudo potential [103]

The pseudopotential approach removes the core electrons and the strong nuclear potential and replaces them with a weaker pseudopotential which acts on a set of pseudo wave functions rather than true wave functions. The pseudopotential approach [104] has its roots in well known fact that the valence electrons play dominant role in chemical bonding and is based on orthogonalised plane wave (OPW) method [105]. An OPW is defined as linear combination of a plane wave and core wave functions summed over all core levels with Blöch wave vector **k**, with the assumption that the core wave functions are known (generally obtained from the tight binding approximation of calculated atomic levels) In OPW method, the eigenstate of the Schrödinger equation was taken as a linear combination of OPW's.

In the pseudopotential approach, the exact wave function for the valence level is written as linear combination of the OPW's. Assuming the ϕ_k^v to be the plane wave part of the expansion

$$\phi_{\vec{k}}^{v}\left(\vec{r}\right)=\sum_{\vec{K}} c_{\vec{K}} e^{i.\left(\vec{k}+\vec{K}\right).\vec{r}} \tag{3.20}$$

from OPW formalism, the OPW is defined by

$$\begin{aligned} \phi_{\vec{k}} &= e^{i\vec{k}.\vec{r}} + \sum_{c} b_c \psi_{\vec{k}}^{c}\left(\vec{r}\right) \\ b_c &= -\int d\vec{r}\ \ \psi_{\vec{k}}^{c*}\left(r\right).e^{i\vec{k}.\vec{r}} \end{aligned} \tag{3.21}$$

The exact valence wave function can be written as

$$\psi_{\vec{k}}^{v}(\vec{r}) = \phi_{\vec{k}}^{v}(\vec{r}) - \sum_{c}\left(\int dr'\ \psi_{\vec{k}}^{c*}(\vec{r}')\phi_{\vec{k}}^{v}(\vec{r})\right)\psi_{\vec{k}}^{c}(\vec{r}) \tag{3.22}$$

This satisfies the Schrödinger equation with eigenvalues $\varepsilon_{\vec{k}}^{v}$

$$H\ \psi_{\vec{k}}^{v} = \varepsilon_{\vec{k}}^{v}\ \psi_{\vec{k}}^{v} \tag{3.23}$$

solving the above Schrödinger equation the following expression is obtained

$$H\phi_{\vec{k}}^{v} - \sum_{c}\left(\int d\vec{r}'\ \psi_{\vec{k}}^{c*}(\vec{r})\phi_{\vec{k}}^{v}(\vec{r})\right)H\psi_{\vec{k}}^{c}(\vec{r}) = \varepsilon_{\vec{k}}^{c}\left(\phi_{\vec{k}}^{v} - \sum_{c}\left(\int d\vec{r}'\ \psi_{\vec{k}}^{c*}(\vec{r})\phi_{\vec{k}}^{v}(\vec{r})\right)\psi_{\vec{k}}^{c}(\vec{r})\right) \tag{3.24}$$

Since for the exact core levels, one can write $H\ \psi_{\vec{k}}^{c} = \varepsilon_{\vec{k}}^{c}\ \psi_{\vec{k}}^{c}$, the above equation becomes

$$\left(H + V^{R}\right)\phi_{\vec{k}}^{v}(\vec{r}) = \varepsilon_{\vec{k}}^{v}(\vec{r})\phi_{\vec{k}}^{v}(\vec{r}) \tag{3.25}$$

This is the effective Schrödinger equation satisfied by ϕ_{k}^{v} which is the smooth part of the Blöch function.

Some of the cumbersome terms have been buried in the term V^R and is defined as

$$V^R\psi = \sum_c \left(\varepsilon_k^v - \varepsilon_c\right)\left(\int d\vec{r}' \psi_{\vec{k}}^{c*}(\vec{r})\psi(\vec{r})\right)\psi_{\vec{k}}^{c*}(\vec{r}) \tag{3.26}$$

Also as ϕ_k^v can be approximated by linear combination of a small number of plane waves, one might be tempted in employing the nearly free electron theory to find the valence levels of Hamiltonian $H + V^R$. This forms the starting point for pseudopotentials calculations and analysis. The pseudopotential is defined as the sum of actual periodic potential and V^R [77].

The disadvantage of plane wave method is that its usage in the all electron treatment is almost impossible because of the strong oscillations of the wave function in the core region. This would require too large a basis set to compute. The pseudopotentials are constructed such that there are no radial nodes in the pseudo wave function in the core region and that the pseudo wave functions and the pseudopotentials are identical to the all electron wave function and potential outside a cutoff radius. Care should be taken so that the scattering properties of the pseudo wave functions are identical to that of the ion and core electrons. This is achieved using non-local pseudopotential which uses a different potential for each angular momentum component of the pseudopotential. Such pseudopotentials conserving the normalization factor are known as norm conserving pseudopotentials. The utility of this approach to systems containing highly localized valence orbitals has been limited, because of the difficulty of representing the pseudo wave functions in a plane wave basis. Since the norm conserving condition requires that the total pseudo charge inside the core matches that of the all electron wave function, it is

sometimes impossible to construct a pseudo wave function much smoother than the all electron one. Alternate approaches using fully non local separable pseudopotential based on given semi local one has been suggested [106].

David Vanderbilt [107] constructed first principles pseudopotentials in which the non local pseudopotentials are generated directly such that (1) they take the form of a sum of few separable terms (2) It becomes local and vanishes outside the core and (3) The scattering properties and their energy derivatives are by construction, correct at several energies spanning the range of occupied states. (4) The norm conserving constraint is removed so that so that the smoothness of the pseudo wave functions can be optimized. (5) The pseudopotential itself becomes involved in the self consistent screening process. These potentials are known as Vanderbilt's ultra-soft pseudopotentials.

3.5 Projector Augmented Wave (PAW) Method

The linear augmented plane wave (LAPW) method provides an efficient representation of the highly inhomogeneous wave functions of the all electron electronic structure calculations. It is constructed by partitioning the wave function around the atom in two parts namely the sphere around each atom where the wave function is rapidly varying and the remaining as interstitial region where the wave functions are smooth. Each basis function is then defined as a plane wave in the interstitial region connected smoothly to the linear combination of atomic like wave functions in the spheres.

The projector augmented wave method is an extension of the augmented wave methods and the pseudopotential approach which combines them into a unified electronic

structure method. Just as in the OPW formulation one can define a smooth part of the valence wave function $\tilde{\psi}_i^v(\vec{r})$ and a linear transformation $\psi^v = T\tilde{\psi}^v$ that relates the set of all electron valence functions $\psi_j^v(\vec{r})$ to the smooth function $\tilde{\psi}_i^v(\vec{r})$. The transformation is assumed to be unity except with a sphere centered on the nucleus, $T = 1 + T_0$. The superscript v and the labels are omitted for the sake of simplicity. Using Dirac notation from now onwards the expansion of each smooth function $|\tilde{\psi}\rangle$ in partial waves m within each sphere can be written as

$$|\tilde{\psi}\rangle = \sum_m c_m |\tilde{\psi}_m\rangle \tag{3.27}$$

with the corresponding all electron function

$$|\psi\rangle = T|\tilde{\psi}\rangle = \sum_m c_m |\psi_m\rangle \tag{3.28}$$

Hence the full wave function in all space can be written as

$$|\psi\rangle = |\tilde{\psi}\rangle + \sum_m c_m \{|\psi_m\rangle - |\tilde{\psi}\rangle\} \tag{3.29}$$

If the transformation T is required to be linear, then the coefficients must be given by a projection in each sphere

$$c_m = \left\langle \tilde{P}_m \middle| \tilde{\psi} \right\rangle \tag{3.30}$$

for some set of projection operators $\tilde{p}$. If the projection operators satisfy the biorthogonality condition,

$$\left\langle \tilde{p}_m \middle| \tilde{\psi}_{m'} \right\rangle = \delta_{mm'} \tag{3.31}$$

then the one center expansion $\sum_m \left| \tilde{\psi}_m \right\rangle \left\langle \tilde{p}_m \middle| \tilde{\psi} \right\rangle$ of the smooth function $\tilde{\psi}$ equals $\tilde{\psi}$ itself.

Just as for pseudopotentials, there are many possible choices for the projectors. The difference from pseudopotentials, however, is that the transformation T still involves the full all electron wave function. The expression applies equally well to the core and the valence states.

$$T = 1 + \sum_m \left\{ \left| \psi_m \right\rangle - \left| \tilde{\psi}_m \right\rangle \right\} \left\langle \tilde{p}_m \right| \tag{3.32}$$

The general form of the PAW equations can be written in terms of transformation for any operator $\hat{A}$ in the original all electron problem one can introduce a transformed operator $\tilde{A}$ that operates on the smooth part of the wave function [80].

$$\tilde{A} = T^{\dagger} \hat{A} T = \hat{A} + \sum_{mm'} \left| \tilde{p}_m \right\rangle \left\{ \left\langle \psi_m \middle| \hat{A} \middle| \psi_{m'} \right\rangle - \left\langle \tilde{\psi}_m \middle| \hat{A} \middle| \tilde{\psi}_{m'} \right\rangle \right\} \left\langle \tilde{p}_m \right| \tag{3.33}$$

This is very similar to the pseudopotential operator. Specific functional forms are used to display important chemical properties, given the electron charge density.

3.6 Electron Localization Function (ELF)

The study of electron localization is required to systematically study the concept of chemical bonds ubiquitous in quantum chemistry specially pair electron localization in the spirit of Lewis structures. ELF was introduced by Becke and Edgecombe [108] in 1990. The original formula is based on the Taylor expansion of spherically averaged conditional same-spin pair probability density to find an electron close to a same spin reference electron. The main aspect of this formulation is that the ELF so defined is a property of the same spin pair density. Topological classification and rationalization of ELF was proposed by Silvi and Savin [109] a few years later.

Becke's Proposal and Interpretation

Pauli's principle suggests that movement of electrons of same spin is more strongly correlated than that between electrons of different spins. Therefore, it seems convenient to study the electron pair density for electrons of same spin and that of different spins separately. The Hartree-Fock probability of finding two particles of the same spin σ simultaneously at positions 1 and 2 in a multi-electron system is

$$P_2^{\sigma\sigma}(1,2) = \rho_\sigma(1)\rho_\sigma(2) - \left|\rho_1^\sigma(1,2)\right|^2 \tag{3.34}$$

Here $P_2^{\sigma\sigma}(1,2)$ is the same spin pair probability and $\rho_1^{\sigma}(1,2)$ is the σ-spin one body density matrix of the Hartree-Fock determinant.

$$\rho_1^{\sigma}(1,2) = \sum_i^{\sigma} \psi_i^*(1)\psi_i(2) \tag{3.35}$$

The summation is restricted to orbitals of spin σ only. The conditional probability of finding another σ spin electron at position 2, such that an electron of spin σ is located at position 1 with certainty is given by dividing the pair probability by total σ-spin density at position 1.

$$\begin{aligned} P_{cond}^{\sigma\sigma}(1,2) &= \frac{P_2^{\sigma\sigma}(1,2)}{\rho_{\sigma}(1)} \\ &= \rho_{\sigma}(1) - \frac{\left|P_1^{\sigma}(1,2)\right|^2}{\rho_{\sigma}(1)} \end{aligned} \tag{3.36}$$

Both the Hartree-Fock density and the density matrix are invariant with respect to the unitary transformation of occupied orbitals and thus the pair probability is invariant as well. When the position of the electron 2 becomes the reference point i.e. $\rho_1^{\sigma}(1,1) = \rho_1^{\sigma}(1)$ and the integrated value of its squared magnitude $\int \left|\rho_1^{\sigma}(1,2)\right|^2 d2 = \rho_1^{\sigma}(1)$ ensures, respectively, that the conditional probability of finding a second σ-spin electron at the reference point vanishes which is also reflection of Pauli's exclusion principle.

$$P_{cond}^{\sigma\sigma}(1,1) = 0 \tag{3.37}$$

and that the total conditional probability is given by

$$\int P_{cond}^{\sigma\sigma}(1,2) d2 = N_{\sigma} - 1 \tag{3.38}$$

N_σ is the total number of σ-spin electrons in the system. The above equation 3.38 implies that if a σ-spin electron is at position 1, then the total probability of finding another σ-spin electron elsewhere is $N_\sigma - 1$. Since the electron-electron interaction depends on the distance between the electrons, it is convenient to change the co-ordinate system to ones defined by $\vec{r} = \frac{1}{2}(\vec{r}_1 + \vec{r}_2)$ and $\vec{s} = (\vec{r}_1 - \vec{r}_2)$. The Taylor expansion of the spherically averaged conditional pair probability is given as

$$P_{cond}^{\sigma\sigma}(\vec{r}, \vec{s}) = \frac{1}{3}\left[\tau_\sigma - \frac{1}{4}\frac{(\nabla\rho_\sigma)^2}{\rho_\sigma}\right]s^2 + \ldots \tag{3.39}$$

The positive definite kinetic energy is defined as $\tau_\sigma = \sum_i^\sigma |\nabla\psi_i|^2$. The Taylor expansion above of spherically averaged pair probability provides information on the electron localization. The smaller the probability of a second like-spin electron near the reference point, the more highly localized is the reference electron.

The electron localization is thus related to the minimum value of the expression

$$D_\sigma = \tau_\sigma - \frac{1}{4}\frac{(\nabla\rho_\sigma)^2}{\rho_\sigma} \tag{3.40}$$

This is a probability density and is necessarily non negative. The relationship between electron localization and above equation 3.40 is an inverse relationship. The following definition of electron localization function was proposed by Becke and Edgecombe which have somewhat more desirable features.

$$ELF = \left(1+\chi_\sigma^2\right)^{-1} \tag{3.41}$$

where $\chi = {D_\sigma}/{D_0}$ and $D_0 = \frac{3}{5}\left(6\pi^2\right)^{2/3}\rho_\sigma^{5/3}$, with D_0 corresponding to uniform electron gas with spin density equal to the local value of $\rho_\sigma(\vec{r})$. The range of ELF lies between zero and one. A value close to one corresponds to region of space where there is high probability of finding electron localization (bonding), whereas an ELF value close to one half corresponds to a region of electron gas like behavior (non bonding).

CHAPTER 4

CHARACTERIZATION METHODS

4.1 X-ray Diffraction (XRD)

X-ray diffraction is non-destructive technique and is based on elastic scattering of x-rays from structures that have long range order. X-rays have wavelengths from ~0.1 to ~100 Å and located between γ-radiation and UV radiation in the electromagnetic spectrum. X-rays are produced using x-ray tubes, where the electromagnetic waves are produced from impacts of high energy electrons with a metal target. However, such sources have low efficiency and their photon flux is limited by thermal properties of the target material. Synchrotron sources produces x-rays with intensities which are three orders of magnitude higher. These sources are extremely bright, very weakly divergent and limited by the electron current in the high energy beam. Another advantage of the synchrotron source is in the distribution of beam intensity with the wavelength. The high intensity of beam in a broad range of photon energies allows one to select photons ranging from infrared to hard x-rays up to 100 KeV.

X-ray diffraction measurements are performed to study the atomic structure of materials. The crystallographic structure of a material is a three dimensional repetition of arrangement of atoms with minimal volume, known as primitive unit cell. The unit cell is defined in real space by three vectors $\vec{a}_1, \vec{a}_2$ and $\vec{a}_3$ known as the crystal axis. The positions of different atoms relative to the cell origin are given by the cell vectors $\vec{r}_1, \vec{r}_2, \vec{r}_3 \ldots \vec{r}_n$. Fourier transformation provides useful information on the structure. The Fourier representation of real space lattice is known as reciprocal lattice.

Reciprocal lattice plays an important role in the analytical studies of periodic structures. In terms of the crystal axis $\vec{a}_1, \vec{a}_2$ and $\vec{a}_3$, a set of reciprocal lattice vectors can be defined as $\vec{b}_1$, $\vec{b}_2$ and $\vec{b}_3$ such that $\vec{b}_1 = \frac{\vec{a}_2 \times \vec{a}_3}{\vec{a}_1.\vec{a}_2 \times \vec{a}_3}, \vec{b}_2 = \frac{\vec{a}_3 \times \vec{a}_1}{\vec{a}_1.\vec{a}_2 \times \vec{a}_3}$ and $\vec{b}_3 = \frac{\vec{a}_1 \times \vec{a}_2}{\vec{a}_1.\vec{a}_2 \times \vec{a}_3}$. The lattice vectors in the real and reciprocal space are related by generalized expression $\vec{a}_i.\vec{b}_j = \delta_{ij}$ [110].

X-ray diffraction involves the measurement of the intensity of x-rays scattered from electrons bound to the atoms. Waves scattered by atoms at different positions reach the detector with relative phase shift, hence the measured intensities yield information about their relative position. Structural information in powder diffraction can be obtained using Bragg equation $n\lambda = 2d \sin\theta$ which describes the principle of x-ray diffraction in terms of reflection of x-rays by a set of lattice planes characterized by the index triplet *hkl* (Figure 4.1).

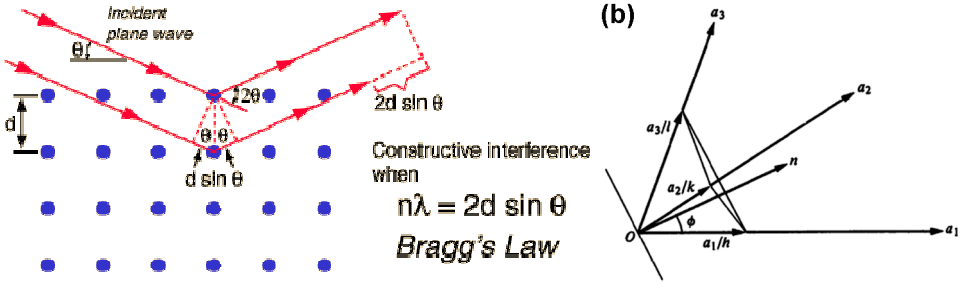

Figure 4.1 (a) Illustration of geometry used for simplified derivation of Braggs law, (b) representation of the crystallographic planes *hkl*. [111]

Miller Indices (*hkl*) was first introduced by British mineralogist William Hallowes Miller and is used to identify the crystallographic planes. By a set of crystallographic planes *hkl* a parallel set of equidistant planes one of which passes through the origin, and the next nearest making intercepts a_1/h, a_2/k and a_3/l on the three crystallographic axes are

implied. Two properties of a set of *hkl* planes involved in using Braggs law are the orientation of planes and their spacing. A simple representation of both properties is obtained by introducing a vector H_{hkl} perpendicular to the *hkl* planes and whose magnitude is reciprocal of the spacing. The H_{hkl} vector in terms of the reciprocal vectors and Millers indices is defined as $\vec{H}_{hkl} = h\vec{b}_1 + k\vec{b}_2 + l\vec{b}_3$. The spacing of the planes d_{hkl} is the perpendicular distance between planes and can be written in terms of the H_{hkl} vector as $d_{hkl} = \frac{1}{\left|\vec{H}_{hkl}\right|}$. Assuming that lengths of the crystal axis is known and the angles between them, the distance between the panes in terms of usual crystallographic notations can be written for a general triclinic lattice below [111].

$$\frac{1}{d_{hkl}^2} = \frac{1}{\left(1 + 2\cos\alpha\cos\beta\cos\gamma - \cos^2\alpha - \cos^2\beta - \cos^2\gamma\right)} \times \left\{ \begin{array}{l} \frac{h^2\sin^2\alpha}{a^2} + \frac{k^2\sin^2\beta}{b^2} + \frac{l^2\sin^2\gamma}{c^2} + \frac{2hk}{ab}\left(\cos\alpha\cos\beta - \cos\gamma\right) \\ + \frac{2kl}{bc}\left(\cos\beta\cos\gamma - \cos\alpha\right) + \frac{2lh}{ac}\left(\cos\gamma\cos\alpha - \cos\beta\right) \end{array} \right\}$$

The variables are defined as a_1=a, a_2=b, a_3=c and α_{23}=α, α_{31}=β, and α_{12}=γ. For a hexagonal lattice (a=b, α=β=90°, γ=120°) which is the focus of study of this research work, the above general formula modifies to

$$\frac{1}{d_{hkl}^2} = \frac{4}{3}\left(\frac{h^2 + hk + k^2}{a^2}\right) + \frac{l^2}{c^2}$$

The atomic structure probed by shining x-ray on the sample results in scattering of the incident x-rays from the material. The intensity of the scattered light can be formulated in a simple manner by considering the diffraction of plane polarized x-rays from a small crystal. Since the source is at a large distance from the crystal, the incident x-rays can be assumed to be plane waves with wavelength λ [Figure 4.2].

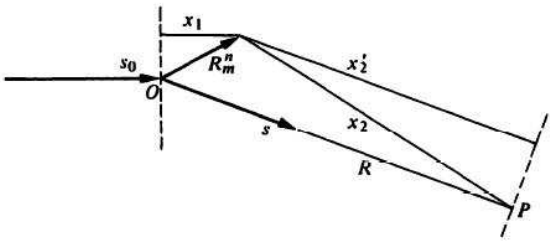

Figure 4.2 Diffraction of a parallel primary beam by a small crystal [111].

Neglecting a 180° jump in phase in the scattering process, the instantaneous value of the electric field at the point of observation due to the unmodified scattering from the atom is given by $\varepsilon_p = \frac{E_0 e^2}{mc^2 R} f_n \cos\left[2\pi\upsilon t - \frac{2\pi}{\lambda}(x_1 + x_2)\right]$. Assuming that the point of observation is at a large distance R from the crystal at O the scattered beam can also be considered to be a plane wave, and hence $(x_1 + x_2) = (x_1 + x_2')$. In terms of the complex exponential, the instantaneous field at P due to the unmodified scattering from the atom is given by $\varepsilon_p = \frac{E_0 e^2}{mc^2 R} f_n e^{i\{2\pi\upsilon t - (2\pi/\lambda)[R-(s-s_0)\cdot(m_1\bar{a}_1 + m_2\bar{a}_2 + m_3\bar{a}_3 + r_n)]\}}$. The resultant field at P due to all atoms in the crystal can be obtained by summing over n to include all atoms in the unit cell, and sum over m_1, m_2 and m_3 to include all unit cells. For simplicity the cell is assumed to be a parallelepiped with edges N_1a_1, N_2a_2 and N_3a_3.

Separating the four summations, the instantaneous field is expressed by

$$\varepsilon_p = \frac{E_0 e^2}{mc^2 R} e^{i2\pi\left[\upsilon t-(R/\lambda)\right]} \sum_n f_n e^{(2\pi i/\lambda)(\vec{s}-\vec{s}_0).\vec{r}_n} \sum_{m_1=0}^{N_1-1} f_n e^{(2\pi i/\lambda)(\vec{s}-\vec{s}_0).m_1\vec{a}_1}$$
$$\times \sum_{m_2=0}^{N_2-1} f_n e^{(2\pi i/\lambda)(\vec{s}-\vec{s}_0).m_2\vec{a}_2} \sum_{m_3=0}^{N_3-1} f_n e^{(2\pi i/\lambda)(\vec{s}-\vec{s}_0).m_3\vec{a}_3}$$

The summation over n involves the positions of all atoms in the unit cell and hence it varies from one structure to the other. The summations over m_1, m_2 and m_3 have the form of geometric progressions. The instantaneous field at P can be written as

$$\varepsilon_p = \frac{E_0 e^2}{mc^2 R} e^{i2\pi\left[\upsilon t-(R/\lambda)\right]} F \frac{e^{(2\pi i/\lambda)(\vec{s}-\vec{s}_0).N_1\vec{a}_1}-1}{e^{(2\pi i/\lambda)(\vec{s}-\vec{s}_0).\vec{a}_1}-1} \frac{e^{(2\pi i/\lambda)(\vec{s}-\vec{s}_0).N_2\vec{a}_2}-1}{e^{(2\pi i/\lambda)(\vec{s}-\vec{s}_0).\vec{a}_2}-1} \frac{e^{(2\pi i/\lambda)(\vec{s}-\vec{s}_0).N_3\vec{a}_3}-1}{e^{(2\pi i/\lambda)(\vec{s}-\vec{s}_0).\vec{a}_3}-1}$$

The complex conjugate of the instantaneous filed at P is

$$\varepsilon_P^* = \frac{E_0 e^2}{mc^2 R} e^{-i2\pi\left[\upsilon t-(R/\lambda)\right]} F^* \frac{e^{-(2\pi i/\lambda)(\vec{s}-\vec{s}_0).N_1\vec{a}_1}-1}{e^{-(2\pi i/\lambda)(\vec{s}-\vec{s}_0).\vec{a}_1}-1} \frac{e^{-(2\pi i/\lambda)(\vec{s}-\vec{s}_0).N_2\vec{a}_2}-1}{e^{-(2\pi i/\lambda)(\vec{s}-\vec{s}_0).\vec{a}_2}-1} \frac{e^{-(2\pi i/\lambda)(\vec{s}-\vec{s}_0).N_3\vec{a}_3}-1}{e^{-(2\pi i/\lambda)(\vec{s}-\vec{s}_0).\vec{a}_3}-1}$$

The complex conjugate of the structure factor is $F = \sum_n f_n e^{-(2\pi i/\lambda)(\vec{s}-\vec{s}_0).\vec{r}_n}$. The amplitude of the field at point P is $E^2 = \varepsilon_P \varepsilon_P^*$. The Intensity at the point of observation is written as $I_p = E^2 c/8\pi$. The intensity of the primary beam can be written as $I_0 = E_0^2 c/8\pi$. The above expression was derived for primary beam polarized with electric field perpendicular to the plane of paper. A similar derivation for the primary beam with

electric field polarization within the plane of the paper would have resulted in additional factor of $\cos^2 2\theta$. For an unpolarized light, E_0 takes all orientations introducing a polarization factor of $\left(1+\cos^2 2\theta\right)/2$. For an unpolarized primary beam of intensity I_0, the intensity I_p from a small parallelepiped crystal is given by

$$I_p = I_e F^2 \frac{\sin^2(\pi/\lambda)(\vec{s}-\vec{s}_0).N_1\vec{a}_1}{\sin^2(\pi/\lambda)(\vec{s}-\vec{s}_0).\vec{a}_1} \frac{\sin^2(\pi/\lambda)(\vec{s}-\vec{s}_0).N_2\vec{a}_2}{\sin^2(\pi/\lambda)(\vec{s}-\vec{s}_0).\vec{a}_2} \frac{\sin^2(\pi/\lambda)(\vec{s}-\vec{s}_0).N_3\vec{a}_3}{\sin^2(\pi/\lambda)(\vec{s}-\vec{s}_0).\vec{a}_3}$$

where $I_e = I_0 \frac{e^4}{m^2c^4R^2}\left(\frac{1+\cos^2 2\theta}{2}\right)$ and FF^* has been abbreviated by F^2. The structure factors depend upon the atomic positions represented by the cell vectors $\vec{r}_n$. For the *hkl* reflection one is interested in the value of the structure factor when the Braggs law is satisfied for this set of planes. Expressing the cell vectors in terms of fractional coordinates, and using the $(\vec{s}-\vec{s}_0)$ value which correspond to an *hkl* –reflection, the expression for the structure factor is written as $F_{hkl} = \sum_n f_n e^{2\pi i(hx_n+ky_n+lz_n)}$. The intensity of the Bragg's peak is given by $|F_{hkl}|^2$.

The line profile analysis can be used to investigate the microstructure and lattice defects in materials. The main study is related to the study of crystalline domain size, shape and the size distribution, planar defects (twin and stacking faults). For a perfect infinite crystal the reciprocal lattice is made up of points each representing a set of planes with Miller indices (*hkl*). Diffraction takes place when the incident and diffracted beams are such that the scattering vector $d^* = (\nu-\nu_0)/\lambda$ connects the origin with an (*hkl*) point.

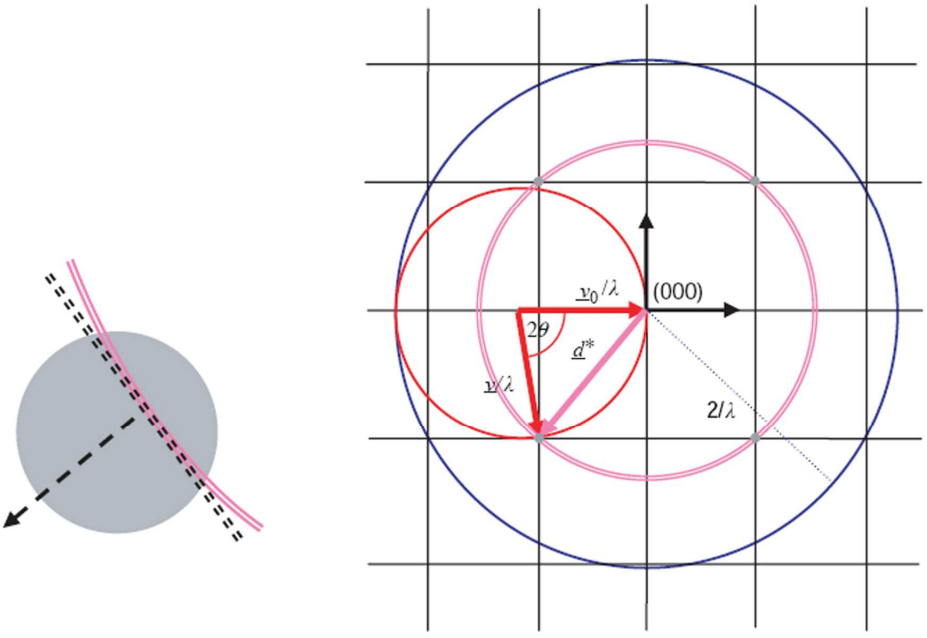

Figure 4.3 Reciprocal space (2D) representation of the diffraction condition: Ewald sphere (radius 1/λ), limiting sphere (radius 2/λ) and powder diffraction sphere (double line radius d*). Left: Enlargement of the intersection between powder diffraction sphere and reciprocal space point with approximating tangent plane. The arrow shows the direction of expansion of the diffraction sphere during a powder diffraction measurement [112].

In powder diffraction, this condition holds for all equivalent points lying on the Ewald sphere leads to the concept of peak multiplicity and systematic overlap. The size of the points, for a perfect crystal, is uniquely determined by instrumental factors and absorption, so the diffraction intensity is confined to a small region around each point, and the FWHM is quite small as illustrated below (Figure 4.4).

When the crystalline domains have a finite extension the diffracted intensity is no longer confined to a point, but spread over a region whose size and shape are related to the crystallite size and shape. If the crystalline domains of a cubic phase are cubes of edge D=Na (N is a positive no.), the corresponding reciprocal space have the same

symmetry and the diffracted intensity in the reciprocal space is give by the so called interference function, for a (00l) point the intensity can be written as

$$Y\left(d^{*}\right) \propto \frac{\sin^{2}\left(\pi N a s_{ool}\right)}{\left(\pi a s_{ool}\right)^{2}} \tag{4.1}$$

The expression is different for different (hkl) and crystallites shapes thus providing intensity profiles with different width and shapes [112].

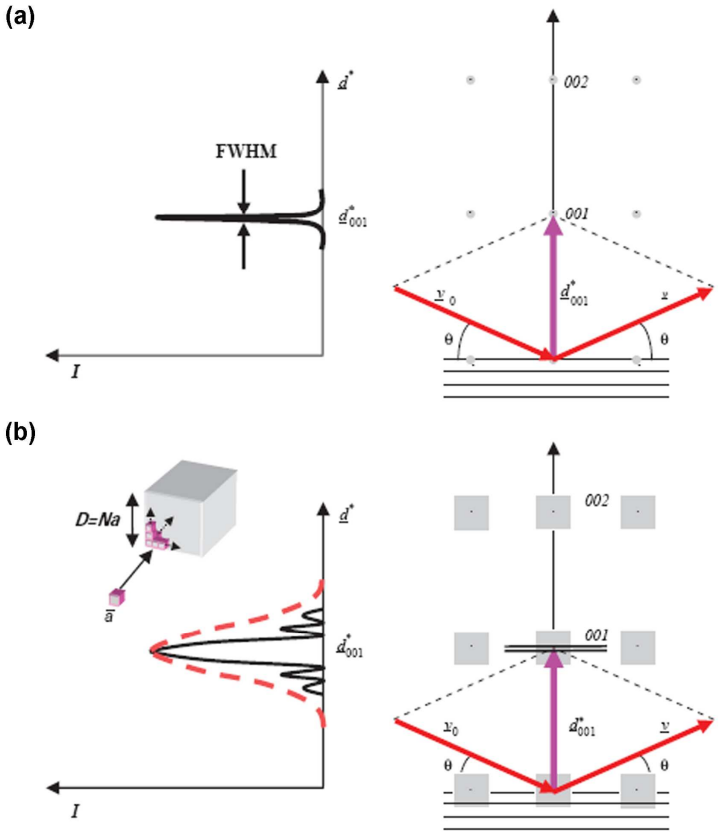

Figure 4.4 (a) Schematic representation of the (001) diffraction condition (right) and amplitude of the diffracted intensity (left) in reciprocal space for an ideally perfect crystal. (b) For cubic crystalline domains of edge D (left inset). The profile of a dispersed system of cubic crystallites is sketched (dash) out [112].

4.2 Electron Microscopy

Microscopy is visual perception of objects. The invention of microscopes dates back to 1590 in Netherlands. In 1873, German physicist Ernst Abbe published his theory of the formation of images by microscopes in which he related the diffraction limited resolving power of the microscope as $d_0 = 0.61\lambda / n\sin\alpha$, where λ = wavelength of the electromagnetic wave, n = refractive index and α = half angle subtended by the objective at the object. The typical magnification of an optical microscope is up to 1500x with a theoretical resolution limit of about 200 nm. For visualization of nano scaled objects smaller wavelengths of probe beam is required. Utilizing the wave nature of particles, electrons with wavelengths $\lambda = h / p$ can fill this role.

A beam of moving electrons can be regarded as a beam of invisible radiation which, given the means of focusing it could be used to form an image. The wavelength varies inversely with the square root of the accelerating voltage. The driving force behind the development of electron microscopes was the desire to exploit shorter wavelength radiations to reveal finer structural details. The generation, manipulation and use of electron beams can only take place in vacuum. The direction of travel of a moving electron can be altered either by applying a magnetic or an electric field. This makes possible two different types of lenses in electron-optical systems, the magnetic lenses and the electrostatic lenses.

A beam of electrons from an electron gun is focused by a condenser lens on to a specimen. In the transmission electron microscope (TEM) the electron transmitted through an entire image field are focused by objective and projector lenses into an enlarged image on a fluorescent screen. In the scanning electron microscope (SEM) a

finely focused beam of electrons is scanned across the specimen and gives rise to electron-matter interactions which are used to reconstruct the image from the signal.

In optical microscopes, the light falling on an object is reflected, transmitted, scattered, absorbed, or re-emitted at another wavelength. The main modes of light microscopy result from these effects. However, in electron microscopy, the electron bombardment produces a large number of effects from the target material. The incident electron beam interacts with the sample and are significantly scattered by them. Most of the energy of the incident beam ends up heating the sample. The electrons undergo two types of scattering namely (a) elastic and (b) inelastic. In elastic scattering, the electron trajectory changes but the energy and momentum is conserved. This process is known as electron back scattering. In Inelastic scattering, the trajectory of the incident electrons is slightly perturbed but the energy is lost through interactions with valence or lightly bound electrons of the atoms in the sample. Inelastic scattering produces diverse effects such as (a) Phonon excitation (heating), (b) cathodoluminescence (visible light fluorescence), (c) continuum radiation (bremsstrahlung), (d) characteristics x-ray radiations, (e) Plasmon production (secondary electrons), and (f) Auger electron production. Below two types of electron microscopes namely, the transmission electron microscope (TEM) and the scanning electron microscope (SEM) are briefly discussed [113].

4.2.1 Transmission Electron Microscope (TEM)

The first TEM was built by Max Knoll and Ernst Ruska in 1931. A sketch of Ruska's design from his original notebook is shown (Figure 4.5 (a)). In a TEM a beam of electrons is transmitted through an ultra thin sample. The electron beam interacts with the specimen as it passes through the sample.

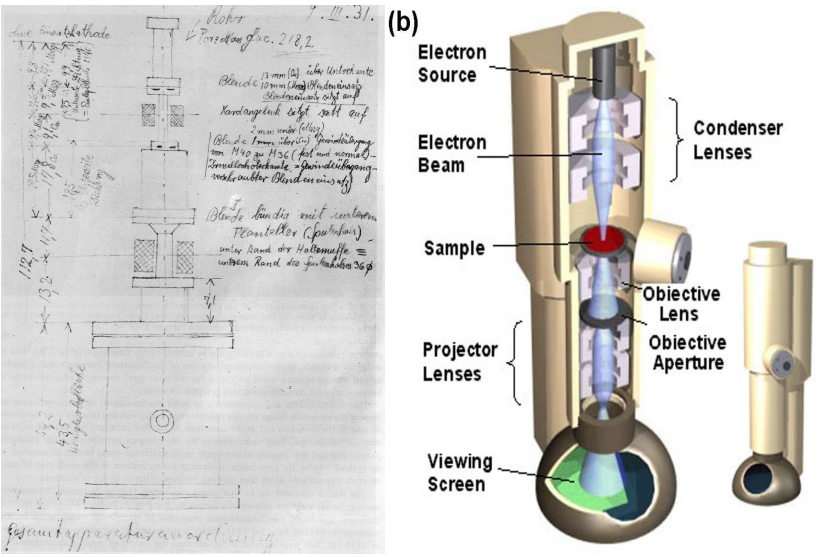

Figure 4.5 (a) Sketch of the first electron microscope originally from Ruska's notebook in 1931 [Wikipedia], (b) cross section of modern TEM column [http://barrett-group.mcgill.ca/teaching/nanotechnology/nano02.htm].

The sample is deposited on a standard TEM grid (3.05 mm diameter) made of copper, molybdenum, gold or platinum. The TEM samples are required to be at most few nanometers thick. High quality samples have thickness comparable to the mean free path of the electrons travelling through the sample. Imaging methods in TEM utilize the information contained in the electron waves exiting from the sample to form the image. The observed intensity of the image, I, assuming sufficiently high quality of imaging device, can be approximated as proportional to the time-average amplitude of the electron wave function, the wave function of the exit beam is indicated by ψ.

$$I(x) = \frac{k}{t_1 - t_0} \int_{t_0}^{t_1} \psi\psi^* dt \tag{4.3}$$

Different imaging methods attempt to modify the electron waves exiting from the sample to obtain useful information. Thus the observed image depends not only on the amplitude of the beam, but also the phase of the electrons. High resolution image requires thin samples and higher energies of incident electrons.

By adjusting the magnetic lenses such that the back focal plane of the lens is placed on the imaging device, a diffraction pattern can be generated. For thin crystalline samples, an image is produced which either may consist of pattern of dots indicating crystalline sample or may consist of series of rings indicating poly crystalline or amorphous material. These images provide information about the space group symmetries for crystalline materials.

4.2.2 Scanning Electron Microscope (SEM)

The earliest SEM was constructed in late 1930s and early 1940s. A very fine probe of electrons with energies from few hundred eV to tens of keV is focused at the surface of the specimen and scanned across it in a ‘raster’ or pattern of parallel lines. A wide range of phenomenon occurs on interaction of electron beam with the sample and signal due to electrons or radiations can be collected for every position of the incident electron probe. The magnification produced by a SEM is the ratio between the dimensions of the final image display and the field scanned on the specimen. In a typical SEM the magnification varies from 20X to 100 000X at a working distance of 11mm.

The SEM is most commonly operated in low energy (< 50 eV) secondary electron (SE) mode. These electrons are ejected from the K shell of the sample atoms by inelastic

scattering and originate within a few nanometers from the sample surface. Such electrons are detected using scintillator-photomultiplier system Everhart-Thornley detectors.

Back scattered electron (BSE) are high energy electrons that are reflected or back scattered by elastic scattering. SEM can be operated by collecting these electrons. Heavy elements back scatter electrons more than the lighter elements and thus appear brighter in BSE images. Everhart-Thornley detectors are inefficient for BSE electron detection, dedicated BSE detectors (semiconductor or scintillator types) are positioned above the same in a “doughnut” type arrangement.

4.3 UV – Vis Spectroscopy

UV – Vis spectroscopy involves the spectroscopy of photons in the UV – Vis region of the electromagnetic spectrum. Different molecules absorb radiations of different wavelengths. An absorption spectrum shows a number of absorption bands corresponding to structural groups within the molecule. The absorption of UV-Visible radiations corresponds to the excitation of outer electrons to the excited states (Figure 4.6). Three types of electronic transitions can be considered namely (a) transitions involving p, s and n electrons, (b) transitions involving the charge transfer electrons, and (c) transitions involving d and f electrons.

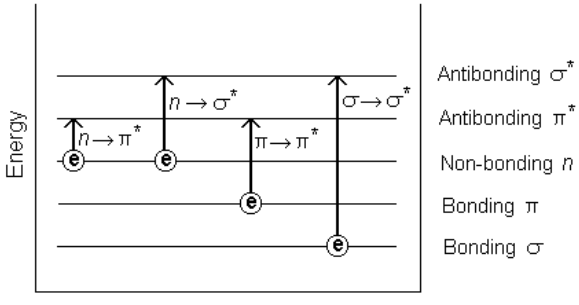

Figure 4.6 Possible electron transitions containing p, s and n electrons.

In this method the spectrometer measures the intensity of light passing through the sample and compares it to the original intensity of the light (before passing the sample). The ratio $\%T = I / I_0$ is called the transmittance while the absorbance can be obtained using the Beer's Law $I = I_0 e^{-\mu x}$.

4.4 Raman Spectroscopy

C. V. Raman in 1928 discovered Raman effect, which is inelastic scattering of photons from molecules. Raman spectroscopy is used to study vibrational, rotational and other low frequency modes in a system. Raman effect occurs due to the interaction of electromagnetic field of the incident radiation with the molecule. This is a two photon scattering process involving one photon absorption and one photon emission. In Raman scattering the final state is different usually by a change in the vibrational state, the electronic state being changed.

The electric field of the incident radiation polarizes the molecule and induces a dipole moment (μ_{in}) in the atom or molecule.

$$\mu_{in} = \alpha E \tag{4.4}$$

At some distance Δr away from the molecule's equilibrium geometry, the instantaneous polarization α is given as

$$\mu_{in} = \alpha E \tag{4.5}$$

$$\alpha = \alpha_0 + \left(\frac{\partial \alpha}{\partial r}\right)\Delta r \tag{4.6}$$

If the molecule is vibrating or rotating in some sinusoidal fashion, Δr can be written in terms of vibrational frequency as

$$\begin{aligned} &\Delta r = r_{\max} \cos\left(2\pi \upsilon t\right) \\ &r_{\max} - \textit{maximum vibrational amplitude} \end{aligned} \tag{4.7}$$

The sinusoidal behavior of the electric field can be written as

$$E = E_0 \cos\left(2\pi \upsilon_{in} t\right) \tag{4.8}$$

E_0 is the amplitude and υ_{in} is the frequency of the electric field. Substituting equations 4.2, 4.3 and 4.4 in equation 4.1 the following expression is obtained

$$\begin{aligned} \mu_{in} &= \alpha_0 E_0 \cos\left(2\pi \upsilon_{in} t\right) + E_0 r_{\max}\left(\frac{\partial \alpha}{\partial r}\right)\cos\left(2\pi \upsilon t\right)\cos\left(2\pi \upsilon_{in} t\right) \\ &= \alpha_0 E_0 \cos\left(2\pi \upsilon_{in} t\right) + \frac{E_0 r_{\max}}{2}\left(\frac{\partial \alpha}{\partial r}\right)\left(\cos\left(2\pi t\left(\upsilon + \upsilon_{in}\right)\right) + \cos\left(2\pi t\left(\upsilon - \upsilon_{in}\right)\right)\right) \end{aligned} \tag{4.9}$$

This can be used as a dipole moment operator in a transition moment integral. Analyzing the above equation it is seen that the first term contains υ_{in}, which is the frequency of the incoming light. This relates the outgoing scattered photon to the incoming photon with the same frequency (elastic scattering of light). This explains the Rayleigh scattering. The

second term contains two cosine terms one containing $\upsilon+\upsilon_{in}$ which relates to outgoing scattered photon with increased frequency (inelastic scattering, Stokes) and the last term containing $\upsilon-\upsilon_{in}$ which represents scattered photon with reduced frequency (inelastic, antiStokes).

The Intensity of scattered radiations from a system of randomly oriented molecules is given by the rotational average of the intensities expression

$$I\left(k^{'}\right)=\frac{NIk^{4}}{16\pi^{2}\varepsilon_{0}^{2}}\begin{bmatrix}10\left|\vec{e}.\vec{\vec{e}}^{'}\right|^{2}\alpha_{\lambda\lambda}^{(0)}\left(\omega,-\omega\right)\alpha_{\mu\mu}^{-(0)}\left(\omega,-\omega\right)\\+3\left(3-2\left|\vec{e}.\vec{\vec{e}}^{'}\right|^{2}+3\left|\vec{e}.\vec{e}^{'}\right|^{2}\right)\alpha_{\mu\lambda}^{(2)}\left(\omega,-\omega\right)\alpha_{\mu\lambda}^{-(2)}\left(\omega,-\omega\right)\end{bmatrix}$$

It is to be noted that $\alpha_{ij}^{\upsilon'\upsilon}$ is i,j- symmetric for conventional Raman scattering and the rotational averaging is then essentially the same as that for Rayleigh scattering, giving the scattered intensity as

$$I\left(k^{'}\right)=\frac{NIk'^{4}}{1440\pi^{2}\varepsilon_{0}^{2}}\left[10\left|\vec{e}.\vec{\vec{e}}^{'}\right|^{2}\alpha_{\lambda\lambda}^{(0)\upsilon'\upsilon}\alpha_{\mu\mu}^{-(0)\upsilon'\upsilon}+3\left(3-2\left|\vec{e}.\vec{\vec{e}}^{'}\right|^{2}+3\left|\vec{e}.\vec{e}^{'}\right|^{2}\right)\alpha_{\mu\lambda}^{(2)\upsilon'\upsilon}\alpha_{\mu\lambda}^{-(2)\upsilon'\upsilon}\right]$$

where I is the irradiance and N_υ is the number of molecules in the initial vibrational state υ. For non-totally symmetric modes, the scalar part $\alpha_{\mu\lambda}^{(0)\upsilon'\upsilon}$ is zero; the entire scattering intensity comes from the symmetric term. Under the near resonant conditions, when the incident energy $\hbar ck$ is close to one of the molecular excitation energies the vibrational energies cannot be ignored and $\alpha_{ij}^{\upsilon'\upsilon}$ has an antisymmetric as well as symmetric part .

Rotational averaging gives an angular dependence similar to that for two photon absorption from two beams. The scattered intensity expression becomes

$$I\left(k^{'}\right)=\frac{NIk'^{4}}{1440\pi^{2}\varepsilon_{0}^{2}}\left[A\alpha_{\lambda\lambda}^{\upsilon'\upsilon}\alpha_{\mu\mu}^{-\upsilon'\upsilon}+B\alpha_{\mu\lambda}^{\upsilon'\upsilon}\alpha_{\mu\lambda}^{-\upsilon'\upsilon}+C\alpha_{\mu\lambda}^{\upsilon'\upsilon}\alpha_{\mu\lambda}^{-\upsilon'\upsilon}\right]$$

here A, B and C are polarization dependent coefficients. In terms of the irreducible parts of $\alpha_{\mu\lambda}^{\upsilon'\upsilon}$, the intensity expression can be written as

$$I\left(k^{'}\right)=\frac{NIk'^{4}}{1440\pi^{2}\varepsilon_{0}^{2}}\left[\frac{1}{3}\left(3A+B+C\right)\alpha_{\lambda\lambda}^{(0)\upsilon'\upsilon}\alpha_{\mu\mu}^{-(0)\upsilon'\upsilon}+\left(B-C\right)\alpha_{\mu\lambda}^{(1)\upsilon'\upsilon}\alpha_{\mu\lambda}^{-(1)\upsilon'\upsilon}+\left(B+C\right)\alpha_{\mu\lambda}^{(2)\upsilon'\upsilon}\alpha_{\mu\lambda}^{-(2)\upsilon'\upsilon}\right]$$

The three terms are the contributions from scalar, antisymmetric, and symmetric scattering. The selection rules follow from a consideration of the integral $\left\langle\chi_{o\upsilon'}\left|\alpha_{\lambda\mu}^{00}\right|\chi_{o\upsilon}\right\rangle$ associated with the transition $\left|\phi_{0}\right\rangle\left|\chi_{o\upsilon'}\right\rangle\leftarrow\left|\phi_{0}\right\rangle\left|\chi_{o\upsilon}\right\rangle$. For fundamental transitions $\upsilon'-\upsilon=\pm1$, the product of the vibrational wavefunctions transform as the corresponding normal mode coordinate [114].

4.5 X-ray Absorption Spectroscopy (XAS)

X-ray absorption spectroscopy (XAS) is a widely used experimental technique for determining the local atomic and/ or electronic structure of materials using synchrotron radiations which are highly intense and provide tunable x-ray energy beams. In this technique x-ray beam hits a sample which could be in liquid, gaseous or condensed phase. The oscillating field of the electromagnetic radiation interacts with the electrons in

the atoms and either gets scattered by the electrons or gets absorbed and excite the electrons (Figure 4.7).

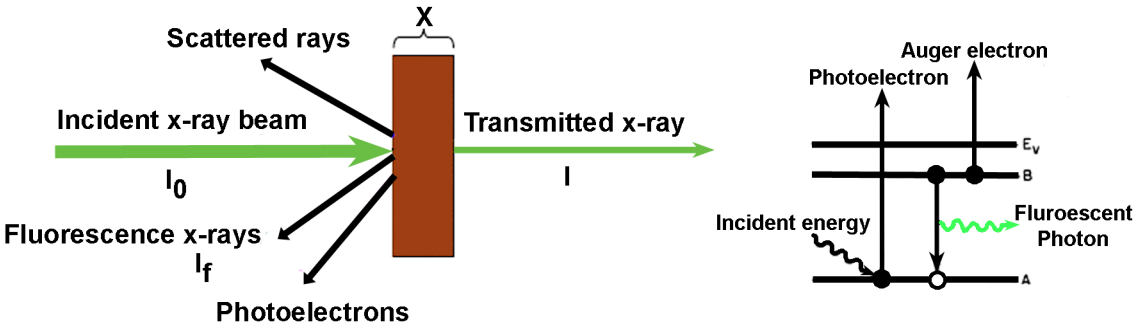

Figure 4.7 Schematic showing different phenomena on interaction of incident x-ray beam with sample.

When discussing the x-ray absorption, the absorption coefficient, μ which give the probability that x-rays will be absorbed according to the Beer's Law $I = I_0 e^{-\mu x}$, where I_0 is the intensity of the incident beam, x is the sample thickness and I is the intensity of the transmitted beam, is of primary concern. At most x-ray energies the, the absorption coefficient $\mu = P_0\sigma$ (P_0 is number density and σ is atomic absorption cross-section) is a smooth function of energy, with a value that depends on the sample density ρ, the atomic number Z, atomic mass A and the x-ray energy E as

$$\mu \approx \frac{\rho Z^4}{AE^3} \tag{4.10}$$

When the incident x-ray has energy equal to the binding energy of a core-level electron, there is a sharp line in absorption: an absorption edge corresponding to the promotion of this core level to the continuum. Since every atom has core-level electrons

with well defined binding energies, one can select the element to probe by tuning the x-ray energy to the appropriate absorption edge. Following an absorption event, the atom is said to be in an excited state, with one of the core electron levels left empty (core hole), and a photo-electron. The excited state eventually decays within a few femtoseconds through two main mechanisms namely as x-ray fluorescence and Auger effect.

In x-ray fluorescence, a higher energy core level electron fills the deeper core hole ejecting an x-ray of well defined energy. The fluorescence energies so emitted are characteristics of the atom and used to identify the atoms in the system along with quantifying their concentrations. The second process for de-excitation of core hole is predominantly the Auger effect, in which an electron drops from a higher electron level and a second electron is emitted into the continuum. In the hard x-ray regime (> 2keV), x-ray fluorescence is more likely the path to de-excitation while in the soft x-ray regimes Auger process is dominant. The energy dependence of the absorption coefficient μ(E) in transmission can be determined as μ(E) = log (I_0/I) and in x-ray fluorescence (or Auger emission) as $\mu(E) \propto I_f / I_0$.

XAS is generally thought to be composed of two distinct portions namely, the near-edge spectra (XANES) typically lying within 30 eV of the main absorption edge dominated by strong photon electron scattering and the extended fine-structure (EXAFS). The limiting energy that divides XANES from EXAFS is by no means exactly defined since the transition from one regime to the other is smooth. A representative XAFS spectrum for fluorine K-edge is shown below (Figure 4.8).

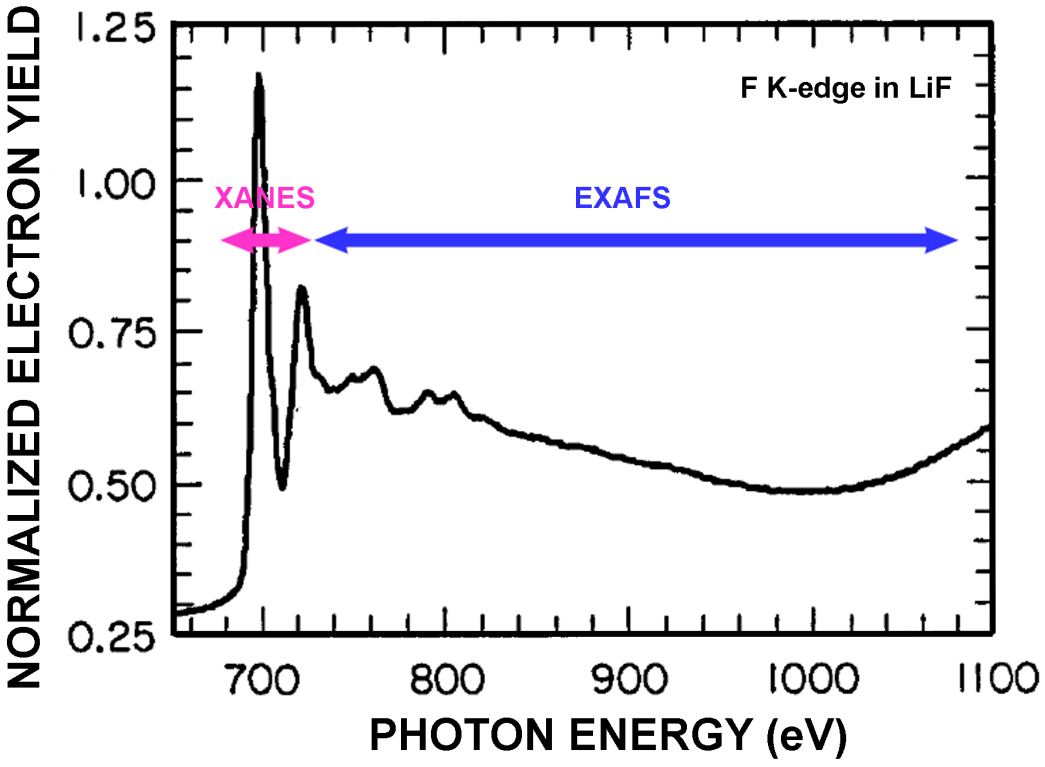

Figure 4.8 Fluorine K-edge XAFS spectrum for LiF [115].

XANES is of great interest as it is capable of providing local chemical and atomic structure in complex and disordered materials. In this kind of spectrometry interaction of photons with matter are studied by measuring the photoabsorption coefficient. For incident light with polarization $\vec{\varepsilon}$ and frequency ω the absorption cross section given by Fermi golden rule is $\sigma = 4\pi^2\alpha\hbar\omega\sum_f \left|\langle i|\vec{r}.\hat{\varepsilon}|f\rangle\right|^2 \delta\left(E_f - E_i + \hbar\omega\right)$. Here the $|i\rangle, |f\rangle$, E_i and E_f denote the initial and final states and their energies. On excitation of the atom using a x-ray source, the core shell electrons can be excited first to empty bound level (localized) and then into the continuum. This results in sharp and broad features respectively. The photoelectrons are sensitive to the charge distribution and arrangement of the neighboring atoms around the absorbing atom.

The high energy region can be more readily interpreted quantitatively. For the EXAFS, one is interested in the oscillations well above the absorption edge and is defined as follows.

$$\chi(E) = \frac{\mu(E) - \mu_{atomic}(E)}{\mu_{atomic}(E)} \tag{4.11}$$

In a molecule or solid, a part of the photo-electron wave may be backscattered from the neighboring atoms thereby modulating the matrix element for the absorption. The back scattered wave may interfere with the out going wave constructively or destructively, depending on the wave vector and distance (Figure 4.8).

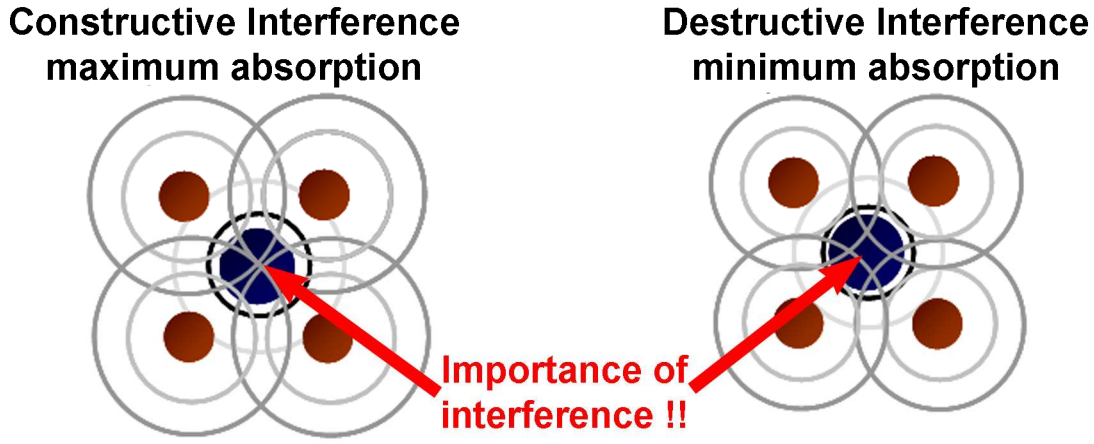

Figure 4.9 Schematic showing constructive and destructive interference of photo-electron scattering.

The presence of photoelectron scattered back from the neighboring atoms will alter the absorption coefficient and is the origin of XAFS. X-ray absorption is a transition between the initial quantum state $\langle i|$ (with an x-ray and core electron) to a final state $|f\rangle$

(with a core hole and a photoelectron). Fermi Golden rule is a way to calculate transition rate from an initial eigenstate to final eigenstate. The absorption coefficient is thus described as

$$\mu(E) \propto \left|\langle i|H|f\rangle\right|^2 \tag{4.12}$$

H represents the interaction term. The core level electrons being very tightly bound to the absorbing atom, the initial state is not altered by the presence of neighboring atoms; however, the final state is influenced because the photoelectrons are able to see the neighbors. Hence, decomposing the final state into two parts, one the "bare atom" portion $|f_0\rangle$ and the other due to the effect of neighboring atoms $|\Delta f\rangle$ as

$$|f\rangle = |f_0\rangle + |\Delta f\rangle \tag{4.13}$$

Expanding equation 4.8 using equation 4.9 the following expression is obtained

$$\mu(E) \propto \left|\langle i|H|f_0\rangle\right|^2 \left[1 + \langle i|H|\Delta f\rangle \frac{\langle f_0|H|i\rangle^*}{\left|\langle i|H|f_0\rangle\right|^2} + \text{ complex conjugate}\right] \tag{4.14}$$

Comparing the above equation 4.10 to the definition of EXAFS (equation 4.7), the "bare atom absorption" can be written as $\mu_0 = \left|\langle i|H|f_0\rangle\right|^2$, which depends only on the absorbing atom irrespective of the presence of neighboring atoms.

The fine structure χ can be written as

$$\chi(E) \propto \langle i | H | \Delta f \rangle + CC \tag{4.15}$$

The interacting Hamiltonian can be written from the field theory as:

$$H = \frac{-e}{mc} \vec{A}.\vec{p} + \frac{e^2}{2mc^2} \vec{A}.\vec{A} - \vec{\mu}.\vec{B} \tag{4.16}$$

For low intensities in zero magnetic fields, the interaction term needed is $\vec{A}.\vec{p}$, where $\vec{A}$ is a quantized vector potential and reduces to a term that is proportional to e^{ikr}. The initial state is a tightly bound core-level which can be approximated by delta function. The change in final state is just the wave function of the scattered photoelectron. Putting all these together [116] a qualitative expression for EXAFS is obtained below

$$\chi(E) \propto \int dr \delta(r) e^{ikr} \psi_{scatt}(r) = \psi_{scatt}(0) \tag{4.17}$$

In a real system usually more than one type of neighboring atoms surround a particular atom which is accommodated in the XAFS formalism by summing the contributions from each scattering atom type. The final form of the EXAFS expression for a system with a single shell of neighbors is given by equation 4.18.

$$\chi(k) = \sum_j N_j e^{-2k^2\sigma_j^2} \frac{f_j(k)}{kR_j^2} \sin\left(2kR_j + \delta_j(k)\right) \tag{4.18}$$

where j represents the individual coordination shell of identical atoms at approximately the same distance from the central atom. The higher order terms correspond to multiple scattering events [116].

CHAPTER 5

DENSITY FUNCTIONAL STUDIES OF CARBON NANOSTRUCTURES

5.1 Introduction

DFT has been successfully used to study the structural and electronic properties of carbon nanostructures namely SWCNTs [117] and GNRs [118] to mention a few. The properties of SWCNTs are known to depend on the rolling/chiral angle [38]. The availability of a wide range of properties for different SWCNTs produced during synthesis imposes bottleneck and has stranded the development of carbon nanotube devices [119]. Recently a lot of effort such as chemical functionalization [120], dielectrophoresis [121] use of bimetallic catalysts for growth [122], has been made in production/extraction of monodispersed single walled carbon nanotubes. However, theoretical predictions have shown that it is very difficult to produce SWCNTs using a bottom – up approach (building up from atomic level) because the thermal vibration of the catalyst particles and the complex nature of growth prevent the preparation of monodispersed SWCNTs. The search for alternative methods is highly desirable for the preparation of monodispersed SWCNTs.

5.2 Computational Details

First Principles calculations have been performed using Vienna ab-initio simulation package (VASP) [123] within the LDA. The calculations were performed using the plane wave basis set. The BZ was sampled using the Monkhorst – Pack scheme.

For ionic relaxations, the conjugate gradient (CG) method was used and the forces acting on the atoms are calculated using the Hellmann – Feynman theorem. The convergence criteria were set such that the forces in the optimized structure were less than 0.001 eV/Å. For the convergence criteria for the electronic self consistency cycle a value of 10^{-7} was taken. Complete relaxation was done by relaxing the lattice as well as the atomic positions without preserving the symmetry of the super cell. The carbon nanotubes bundles were modeled using a hexagonal cell such that each super cell consisted of one nanotube with vacuum layer of about 3.3 Å. The GNRs were modeled in orthorhombic cells ensuring a vacuum layer of more than 10 Å between the two ribbons. SWCNTs were subjected to hydrostatic pressure by equating the diagonal elements of the stress tensor to the desired pressure values. The pressure was increased in steps of 2GPa. GNRs were sandwiched between two rigid graphene sheets representing rigid substrates [124] and pressure was applied by physically moving the two rigid layers in steps ~ 1 Å. The electron localization function was calculated using the formulation of Savin and Silvi [109].

At graphitic separations vdW interactions are expected to become significant. The lattice constants calculated for normal and compressed nanotube bundles using above mentioned DFT methods were compared with those using the Lennard – Jones (LJ) potentials $V = \sigma^2 \iint \left(-\frac{A}{r^6} + \frac{B}{r^{12}} \right) dS_1 dS_2$ (A = 15.2 eV Å, B = 24×10^3 eV Å and σ = 0.3724) [125, 126] which take into account the vdW interactions. The plot (Figure 5.1) shows the equilibrium lattice constants (minima) for different nanotubes, in good agreement to the DFT calculations [127].

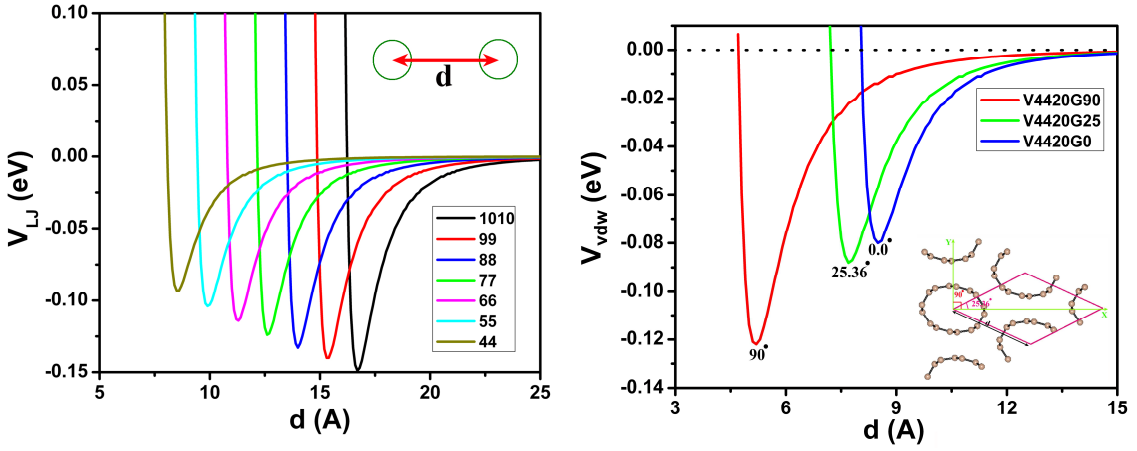

Figure 5.1 LJ potentials calculated for nanotube bundles with different chirality. 1010 denotes (10, 10) SWCNT. Potentials plotted for (4, 4) SWCNT at different lattice angles.

5.3 Edge Reactivity of Armchair and Zigzag Graphene Nanoribbons

The edges in graphene nanoribbons are primarily armchair or zigzag or a combination of the two for the most general case. The properties of edge carbon atoms in large hexagonally symmetric systems depend strongly on the local electronic structure [128]. Hence one may expect varying reactivity for different type of edges in the nanoribbons. Understanding the reactivity can be achieved through electron localization function (ELF).

ELF was first introduced in 1990 [108] is a “chemically intuitive” way to analyze the electron localization and has values in the range 0 – 1. A high value implies the existence of a localized electron pair and that there exists a high probability of finding two electrons of opposite spins in a given region of space and for which there is a small probability of exchange with other electrons that are outside of this region. The ELF is calculated for both armchair (Figure 5.2) and zigzag edged nanoribbons (Figure 5.3).

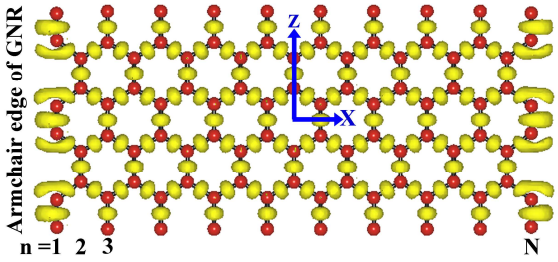

Figure 5.2 Electron localization function for 19AGNR with ELF value plotted at 0.75. The Z axis represents the ribbon axis. The Plot of ELF shows that the ELF at the edges tends to heal.

The ELF is plotted at value of 0.75 and the ribbon axis is plotted along the z axis.

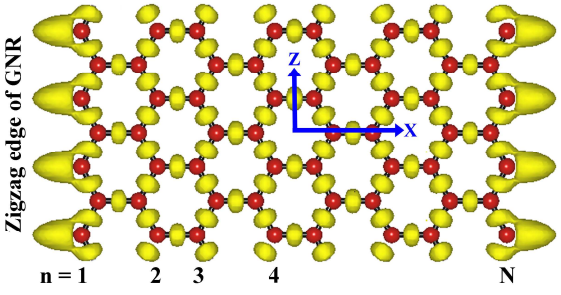

Figure 5.3 Electron localization function for 8ZGNR with ELF value plotted at 0.75. The Z axis represents the ribbon axis. Highly reactive edge dangling bonds are observed.

The core and binding point attractors are found to be located at positions indicated by atoms and the regions shown by the isosurface between pair of atoms respectively. The ELF for ZGNRs shows the presence of highly directional edge dangling bonds where as for the AGNRs, the dangling bonds seem to heal at the edges hence passivating the edges [129]. Experimental evidences in form of scrolled and staggered edges of graphene [130] have been observed.

Attempts have been made to exploit the edge reactivity of GNRs to form carbon nanotubes. Theoretical studies of site specific functionalization of graphene nanoribbons have indicated the possibilities of the formation of carbon nanotubes [131]. Experiments based on this concept have shown the formation of nano scrolls instead of nanotubes

[132]. The two major probable reasons for failure of this proposed method of site specific functionalization is that it is difficult to precisely functionalize the nanoribbons experimentally at specific sites at atomic scale (problems such as steric hindrance come into play). However, the concept is important in the sense that it is investigated for the first time a top down approach for the formation of nanotubes.

5.4 Reconstructing Graphene Nanoribbons to form Tailored Single Walled Carbon Nanotubes

Recent experiments have suggested the closing of edges of graphene multi-layers at very high temperatures [133, 134]. Motivated by these experimental results, a novel conceptual methodology for preparation of SWCNTs is proposed [135]. This methodology simplifies the top down process of nanotubes by using bilayered GNRs instead of mono-layered GNR. In this method the nanotubes are produced either by self interaction of the reactive zigzag edges of graphene nanoribbons or by uniaxially compressing the bilayer nanoribbons normal to ribbon surface, between a pair of rigid surfaces for armchair edges of the graphene nanoribbons to form carbon nanotubes (Figure 5.4).

The advantage of using bilayered system is that now rolling angle is limited to a rotation of only 90° at edges of each nanoribbon. Bi-layers of AGNRs at graphitic separation enclosed in a cell were considered as precursors for zigzag SWCNTs. The cell was chosen such that the separation between the bilayered nanoribbons in the adjacent cells was at least 10 Å. Such large separation ensures minimal interactions between the bilayers in adjacent cells.

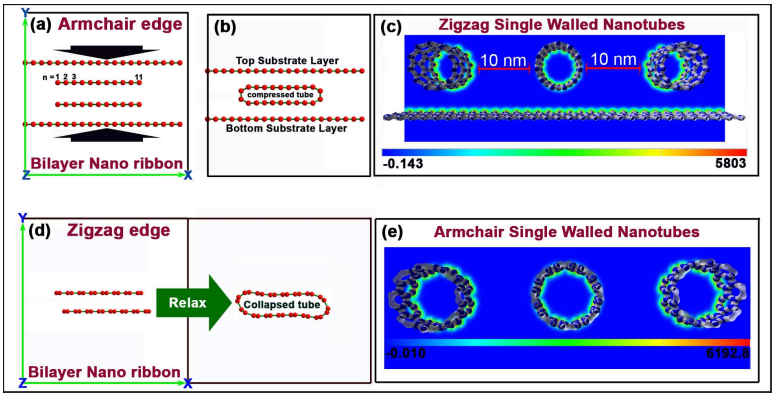

Figure 5.4 Proposed method for preparation of patterned carbon nanotubes by reconstructing the edges of graphene nanoribbons.

These nanoribbons were compressed between a pair of graphene sheets representing highly rigid surfaces, by moving these sheets in discrete steps towards each other.

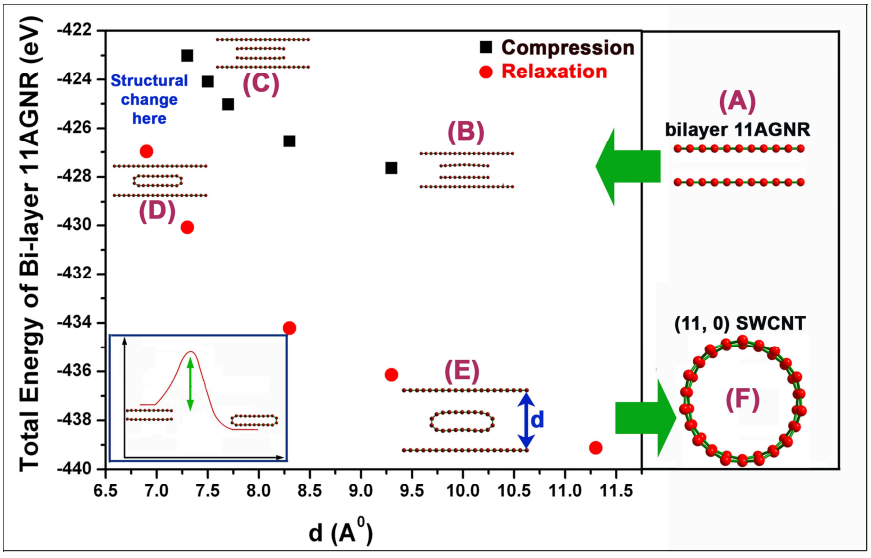

Figure 5.5 Variation of total energy of the bilayered 11AGNR is plotted as function of top and bottom substrate layer separation "d". The bilayer (represented by A) patterned on lower substrate is compressed graphene sheets (shown as B). As "d" decreases, the total energy of the compressed bilayered system (shown as C) is found to increase. Once "d" is reduced sufficiently, bonds form at edges to form compressed tubular structure (shown as D). Relaxing "d" lowers the energy and tubes start to inflate (shown as E). Finally tube acquires a circular tubular cross-section (shown as F) on complete relaxation.

It is observed that as the separation between the sheets representing the rigid surfaces “d” decreases an increase in the total energy of the bilayer is observed (Figure 5.5). On the basis of previously reported experimental results [136] the pressure on the compressed nanotube was estimated to be in the range of 7 GPa – 10 GPa.

In order to understand this process, the ELF, electronic band structure and projected density of states for the bilayered GNRs is investigated below. The ELF is calculated for armchair bilayered GNR and plotted along different planes at reduced separation (Figure 5.6). It is observed that for bilayer AGNRs there is no overlap of the ELF at normal graphitic separation of 3.3 Å. However, at reduced separation of 2.4 Å corresponding to the distance between the two ribbons in the bilayered ribbon, the electron cloud of each of the nanoribbon constituting the bilayered system starts to overlap with each other only at the edges (plane B, Figure 5.6). No overlap of electron cloud is observed at other sites (plane C and D, Figure 5.6). The ELF on the plane (plane A, Figure 5.6) containing the nanoribbon shows the healed edges of the AGNR.

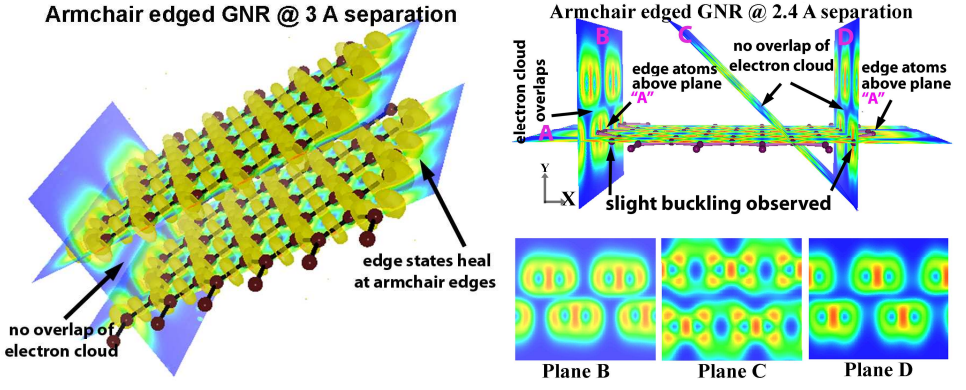

Figure 5.6 ELF plotted along different planes for 11AGNR at different separations.

Finite element model [137] has predicted the presence of edge ripples of about 1.2 Å for mono-layered nanoribbons with armchair edges. Considering the bilayered GNR as

composed of two identical nanoribbons and assuming normal modes of vibration, it would mean that the nanoribbons will start to interact with each other at a separation of about 2.4 Å. Hence the normal graphitic separation of the armchair edged bilayered graphene nanoribbons need to be reduced to about 2.4 Å. Calculations have shown that when the bilayered AGNR is compressed from normal graphitic separations to about 2.4 Å, the bilayered AGNR system slips into compressed tubular cross section without further compression.

For monolayer ZGNR the predicted amplitude of edge ripples using the finite element model [137] is ~2.4 Å. Bilayered GNR system may be considered as a combination of two mono-layered GNRs vibrating with amplitude of ~ 2.4 Å. Such a bilayered system with highly reactive edges can be considered to be unstable at normal graphitic separation of 3.3 Å (Figure 5.7). Our calculations have shown that the bilayered ZGNRs are unstable at normal graphitic separation and form nanotubes instantaneously. Our calculations for bilayered ZGNRs are well supported by the nudged elastic band method calculation [138] which takes into account the interaction of a mono-layered GNR with its image.

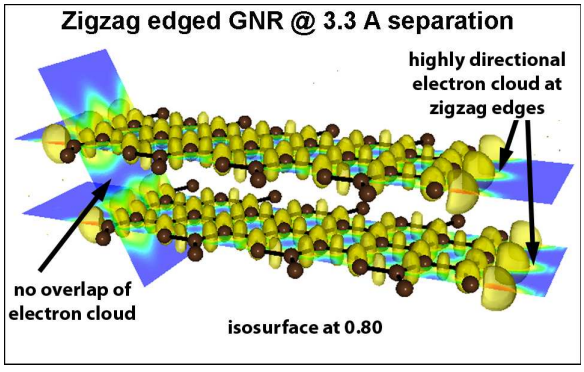

Figure 5.7 ELF for ZGNR at 3.3 Å separation.

The formation of nanotubes from bilayered GNRs is accompanied by rehybridization of the carbon atoms from sp^2 to sp^3 hybrid state. In order to develop a further insight into this process of rehybridization, the electronic band structure and the site projected *lm* decomposed electronic density of states is analyzed. The density of states near the Fermi level provides a quantitative estimate of the chemical reactivity for a given system [139]. All structures with edge states crossing the Fermi level or in its immediate vicinity are expected to be highly reactive. The band structure plot shows that the bilayer 11AGNR has a very small band gap at the Fermi level (Figure 5.8 (a)). The edges of these nanoribbons were terminated by hydrogen atoms to look at the edge states. It is observed that the edge states corresponding to the dangling bonds lie far away from the Fermi level making them relatively chemically inert. Bilayered 11 AGNR when compressed forms semiconducting (11, 0) zigzag SWCNT, which is observed in the electronic band structure diagram (Figure 5.8 (b)).

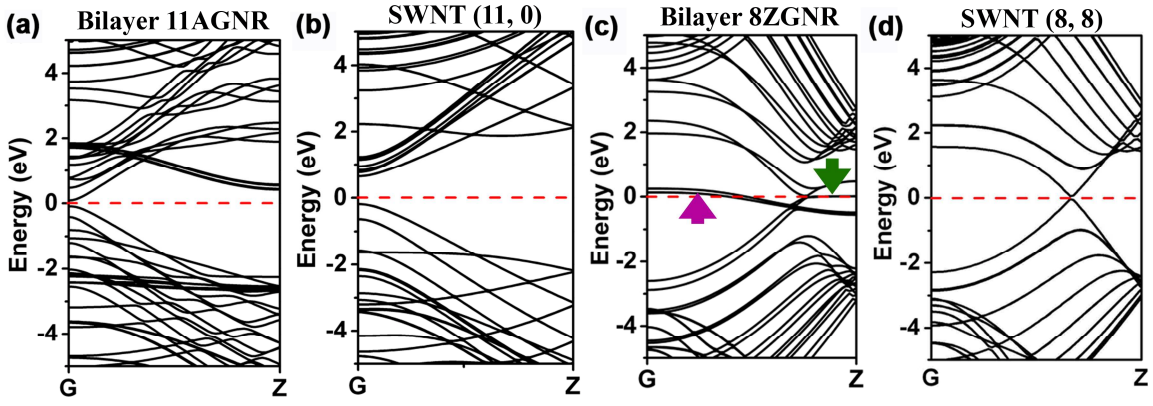

Figure 5.8 Electronic band structure diagram for (a) Bilayered 11AGNR, (b) (11, 0) zigzag SWCNT, (c) Bilayered 8 ZGNR and (d) (8, 8) armchair SWCNT. Magenta arrow indicates the states due to dangling edge bonds while the Green arrows indicate localized edge states.

The band structure of bilayered 8ZGNR shows the availability of edge dangling states as well as bands due to the localized edge states (Figure 5.8 (c)) at the Fermi level suggesting highly reactive edges. At normal graphitic separation a small split is observed in the states representing the edge dangling bonds marked by magenta arrows and the localized edge states marked by green arrows. As the layers approach each other the split increases further and finally metallic bands structure of armchair SWCNT is observed (Figure 5.8 (d)) due to crossing of bands corresponding to π and π^* orbitals.

Site projected partial density of states (PDOS) was analyzed in details to understand the process of rehybridization in the nanotube formation. Representative plots of PDOS have been shown indicating the changes in the PDOS with interaction induced sp^3 hybrid character of the edge atoms in bilayered 11AGNR. Narrowing of the electronic band gap of bilayered 11AGNR at reduced separation is observed while compressing the bilayered system. This can be understood due to the p_y electron states which lie closer to the Fermi level as seen in the site projected PDOS (Figure 5.9). The p_y orbitals are oriented normal to the plane of the GNRs. Modification of PDOS corresponding to s, p_x, p_y and p_z orbitals is also observed. At reduced separation of 2.4 Å a significant increase in the DOS for the p_y orbital is observed indicating rehybridization of the edge atom.

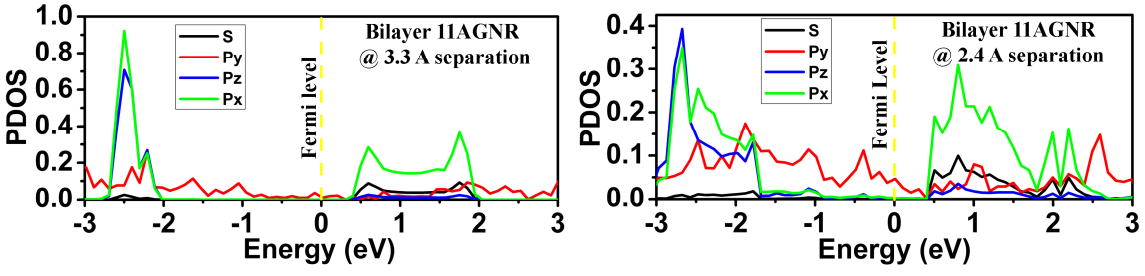

Figure 5.9 Site projected electron density of states at one of the edge atom at different interlayer separation for the bilayered AGNR system.

5.5 From Isolated to Bundled Single Walled Carbon Nanotubes

Properties of isolated single walled carbon nanotubes have been extensively studied. However, carbon nanotubes like to remain bundled such that the separation between the walls of two nanotubes is ~ 3.3 Å. The formation of nanotubes is understood to be due to the strong van der Waals interactions. Experimental studies have shown recently that the width of line widths of the Raman G' modes increases with bundling [140]. The effects of bundling on the electronic properties of isolated single walled carbon nanotubes were predicted for (10, 10) SWCNT using tight binding model as early as 1998. The properties of single walled carbon nanotubes modify when bundled because each nanotube can feel the potential due to the other nanotube as a result of this the Hamiltonian is perturbed, the quantum mechanical level repulsion leads to the opening of a pseudo gap for armchair metallic SWCNTs [141].

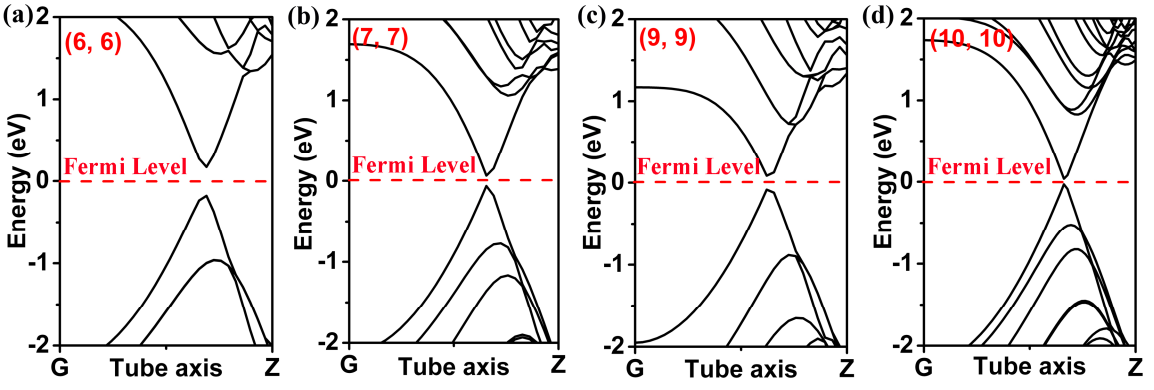

Figure 5.10 Electronic band structure diagram for bundles of different armchair single walled carbon nanotubes.

The effect of bundling is observed not only in armchair SWCNTs but also zigzag SWCNTs. Ab initio density functional calculations have shown the opening of band gap in small and large diameter nanotubes (Figure 5.10). Modification of electronic band structure in semiconducting nanotubes is also observed.

5.6 Effect of Hydrostatic Pressure on Bundled Single Walled Carbon Nanotubes

SWCNTs have remarkable mechanical properties and shows extraordinary strength along the axial direction with commonly accepted axial Young's modulus value of ~1TPa [142, 143]. Radial deformation of carbon nanotubes has attracted a lot of attention due to its possible influence on the electronic properties. The deformation of large diameter SWCNTs under pressure to interacting elliptic, racetrack and peanut shaped cross-sections have been reported both experimentally [144]and theoretically [145, 146]. These structural changes for large diameter nanotubes have also been observed indirectly using Raman spectroscopy, and directly using x-rays [147] and neutron diffraction [148] experiments.

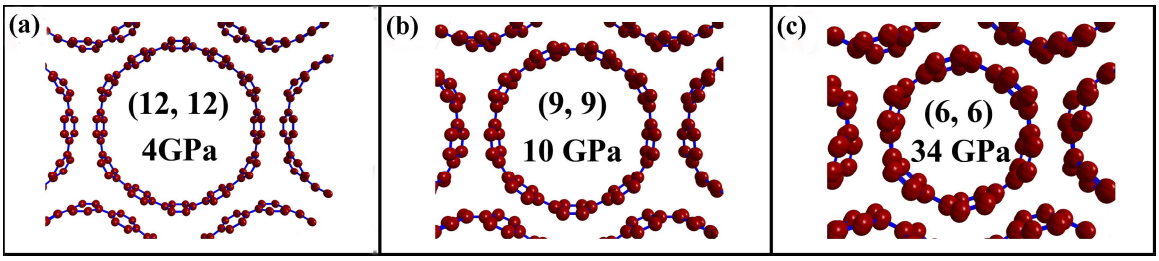

Figure 5.11 Hexagonal cross-section for (a) (12, 12) (b) (9, 9) and (c) (6, 6) armchair nanotubes at different hydrostatic pressure.

It is observed that some nanotubes behave distinctly as compared to others. Studies have shown that carbon nanotubes with chiral indices (3n+3, 3n+3) when subjected to hydrostatic pressure form hexagonal cross sections. This phenomenon is observed in small as well a larger diameter SWCNTs (Figure 5.11).

The onset of the hexagonal cross-section phase decreases as the diameter of the nanotubes increases due to the decreasing stiffness of the nanotube [127]. This hexagonal cross-section is a reversible metastable phase and is expected to convert to peanut/ racetrack cross-section at higher pressure. The onset of cross-section phase is gradual and

no abrupt changes in the energy or volume is observed. Direct observation of the presence of hexagonal cross-sections has been reported in literature [149].

5.7 Quasi Two Dimensional Form of Carbon: A Novel Phase

Carbon is known to exist in many stable one, two and three dimensional allotropic forms. High pressure experiments on carbon nanotubes have been conducted to explore the possibilities of presence of additional stable phases of carbon. Super-hard form of carbon along with addition unidentified phases have been observed. There is a need to understand these unidentified phases of carbon expected to have superior mechanical properties. The study of SWCNTs under pressure has gained significant momentum in order to search for novel forms of carbon other than diamond, graphite, carbon nanotubes etc. consisting of mixture of sp^2 and sp^3 hybrid states of carbon atoms. Recent ab-initio studies have predicted the formation of interlinked structures of only small diameter zigzag single walled carbon nanotubes [150].

In order to search for the novel phases of carbon containing mixture of sp^2 and sp^3 hybridized carbon atoms; systematic studies of hydrostatic pressure on a large number of SWCNT bundles were performed. It is observed that as the pressure is increased on the carbon nanotube bundles, novel interlinked structures comprising of mixture of sp^2 and sp^3 hybridized carbon atoms is observed for large as well as small diameter nanotubes. The formation of novel interlinked quasi two dimensional structures is accompanied by abrupt changes in energy and volume with pressure for both small and large diameter nanotubes [127] (Figure 5.12).

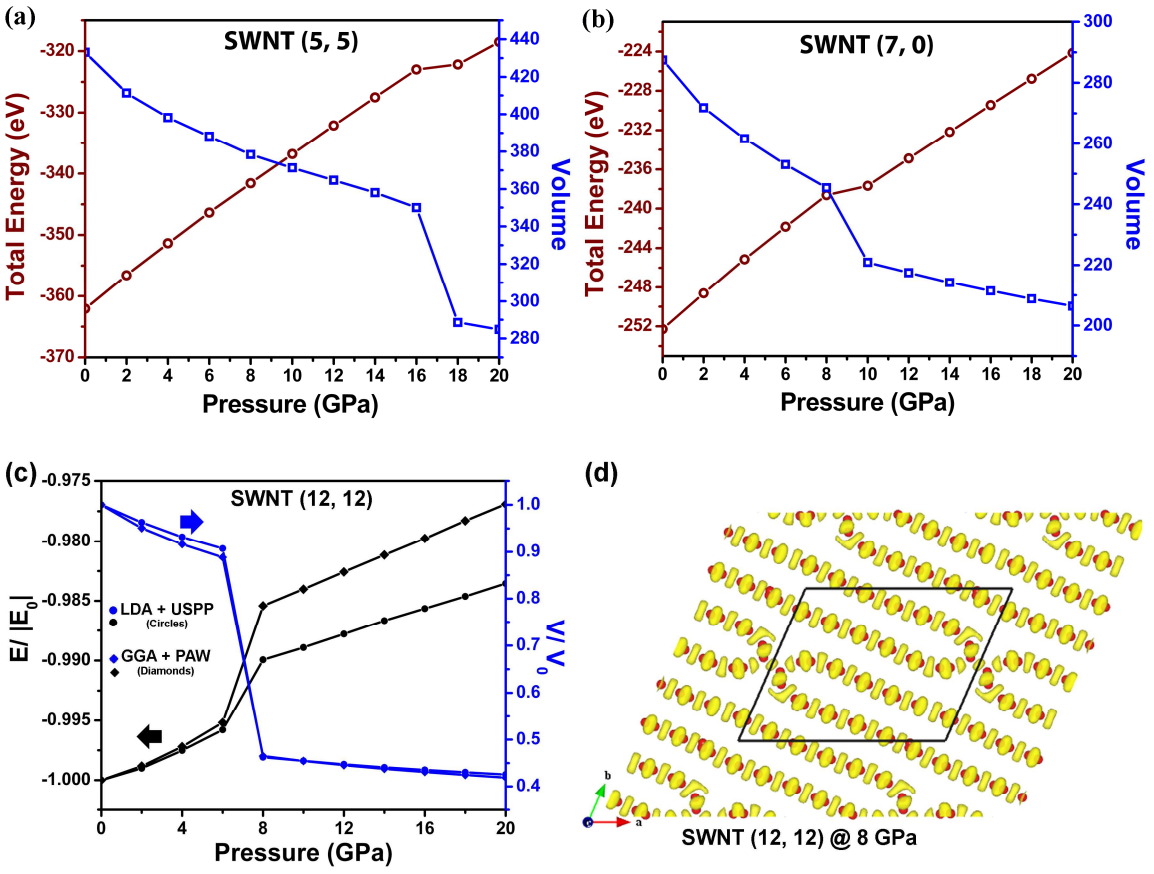

Figure 5.12 Abrupt changes in energy and volume observed with hydrostatic pressure for (a) armchair (5, 5) SWCNT, (b) zigzag (7, 0) SWCNT, (c) armchair (12, 12) SWCNT and (d) ELF showing interacting quasi two dimensional interlinked structure.

The abrupt changes in total energy – pressure and volume – pressure diagrams suggests first order phase transformation indicating formation of a new structural phase. At the onset of these structural phase transformations the nanotube forms chemical bonds with each other. The atoms at highly stressed edges link tetrahedrally by forming bonds with similarly stressed atoms in the neighboring nanotubes. The stability of this novel phase was verified by releasing the hydrostatic pressure. It is observed that when the pressure is released to ambient conditions, the interlinked structure is maintained. These observations are supported by recent experimental observations of quenchable superhard

phase of carbon obtained by cold compression [151]. The Raman spectra of experimentally reported quenchable superhard carbon phase have two broad peaks centered at 1581 cm^{-1} and 1355 cm^{-1} with the peak intensity of 1355 cm^{-1} (D band) much higher than that at 1581 cm^{-1}(G band). Studies on amorphous tetrahedral carbon films have shown that the ratio of the intensity of the peak in D band to that in the G band indicates the ratio of sp^2/sp^3 bonding [152]. The quasi two dimensional sheets of interlinked nanotubes obtained in our calculations are found to have sp^3 bonding only at stressed edges. These observations are in accordance with the ratio of the peak intensity in the Raman spectra of the compressed samples reported earlier [151].

Changes in electronic properties are expected to occur with changes in the atomic structure. The $\pi - \pi^*$ hybridization effect is understood to be a small contributing factor in changing the already existing band gap [153]. In order to understand the modification of the electronic properties the electronic band structure along with the partial density of states (PDOS) is analyzed. An Abrupt phase transition is observed at a critical pressure P_c around 10 GPa for (7, 0) nanotube. A detailed investigation of the electronic properties at 6 GPa and 10 GPa for this system reveals that at 6 GPa the distance between the adjacent atoms at the highly curved edges is about 2.76 Å hence the possibility of bond formation at this stage can be ruled out. The plot of electron localization function (Figure 5.13 (a)) shows that the tubes are not bonded to the neighbors under these conditions. The lectronic band structure clearly shows (inset of Figure 5.13 (a)) the presence of a small band gap at 6 GPa. These individual carbon nanotubes are semiconducting [154] under ambient conditions. As the pressure is increased the symmetry of the nanotubes break such that highly directional charge distributions occurs at stressed edges resulting in

strong bond formation between the atoms at highly stressed atoms with their neighbors in adjacent tubes as seen in ELF plot (Figure 5.13 (b)).

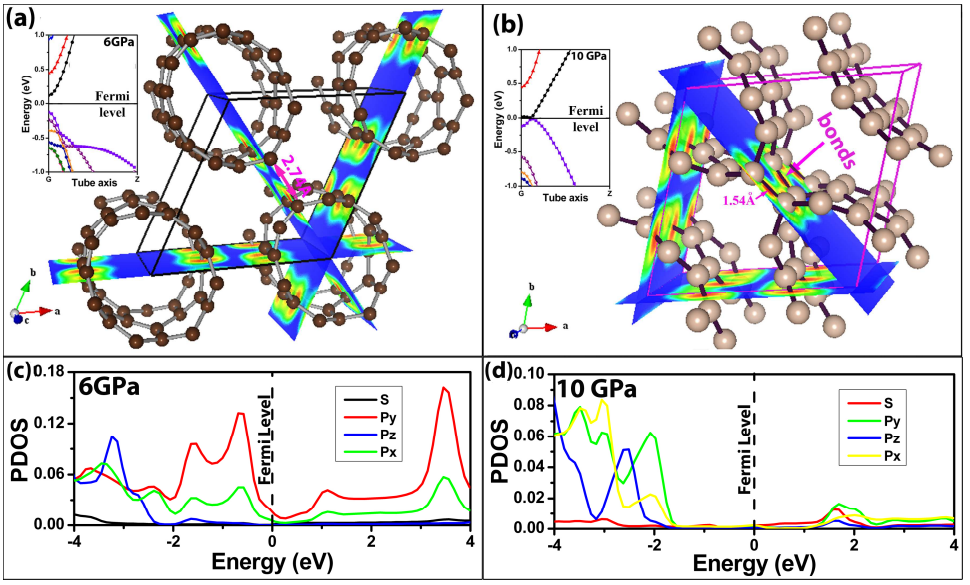

Figure 5.13 (a) Electron localization function (ELF) for (7, 0) nanotube at 6 GPa. The nanotubes are not bonded to each other however, interaction cannot be ruled out at separation of about 2.74 Å. The electronic band structure inset shows a small bandgap at the Fermi level. (b) ELF shows the interlinking of the tubes due to bond formation at 10 GPa along with the crossing of the conduction and the valence band at the Fermi level in the inset. The unit cells are marked with black (Fig. a) and pink (Fig. b) lines. PDOS for one of the highly stressed edge atom (c) at 6 GPa and (d) at 10 GPa.

This is accompanied by crossing of the lowest conduction and valence band at the Fermi level indicating metallic state of the interlined structure along the axis. It is interesting to note that the nanotubes interlink to form 2D layers of interlinked flattened tubes. Although no bond formation is observed between the sheets themselves, the sheets may interact with each other due to reduced separation between them. The PDOS at the highly stressed sites at 6 GPa (Figure 5.13 (c)) and at 10 GPa (Figure 5.13 (d)) is analyzed to understand the role of these atoms and the states associated with these atoms. It is found that at 10 GPa the states move far away from the Fermi level. This is in accordance with the observation that the edge carbon atoms become stable sp^3 hybridized

as found in diamond. The contribution to the DOS at the Fermi level is almost insignificant due to the pure p_x, p_y and p_z orbitals at highly stressed edge atoms hence most of the contribution to the DOS at Fermi level due to pure p_x, p_y and p_z orbitals is expected from other atoms at flattened surfaces.

When (5, 5) SWCNT is compressed the symmetry of the nanotube is lost and the band gap widens to about 0.26 eV (inset of Figure 5.14 (a)) indicating semiconducting behavior at about 16 GPa. At this stage the neighboring tubes with separation of about 2.3 Å are not linked to each other as seen in the ELF plot (Figure 5.14 (a)) however, increased interaction among the nanotubes can be seen. As the pressure is increased the tubes in the neighboring atoms link with each other forming highly interacting sheets as also observed in zigzag (7, 0) nanotube. However, in this case the polygon enclosing the tetrahedral carbon atoms are slightly distorted, as seen in (Figure 5.14 (b)). At this stage, this sheet composed of interlinked (5, 5) nanotubes is found to show metallic properties with bands crossing the Fermi level. Interlinking of nanotubes is also found to occur for larger nanotubes as discussed earlier.

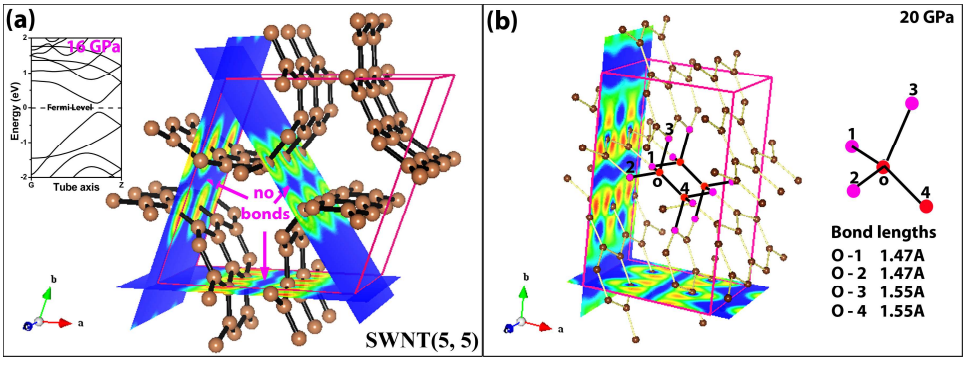

Figure 5.14 (a) Electron localization function (ELF) for (5, 5) nanotube at 16 GPa. The nanotubes are not bonded to each other however, interaction cannot be ruled out at separation of about 2.74 Å. The electronic band structure inset shows a small bandgap at the Fermi level. (b) ELF shows the interlinking of the tubes due to bond formation at 20 GPa. The unit cells are marked with pink lines. Bonds labeled O-1 implies bond length from atom O to atom 1.

The breaking of symmetry depends on the chiral indices of the nanotubes which determines the formation of directional bonds and hence the interlinking of nanotubes under compression. The nanotubes thus form interlinks with the neighboring tubes when highly directional dangling bonds are formed at the stressed edges of the cross-sections. The availability of highly directional dangling bonds in close vicinity enables bond formation thereby reducing the energy of the system causing abrupt changes in the energy – pressure diagrams.

CHAPTER 6

DENSITY FUNCTIONAL STUDY OF BORON NANORIBBONS

6.1 Introduction

The general perception of a boron sheet is that it occurs in a buckled plane of a triangular lattice to form monolayer boron sheet [155]. It had been demonstrated that the reconstructed {1221} sheets of boron are more stable than the idealized {1212} sheets [156]. Investigations of bare boron clusters have revealed that the two basic units of boron, hexagonal and pentagonal pyramids may hold the key to form stable boron structures [157, 158]. Recently it has also been shown theoretically that monolayer sheets of boron are composed of triangular and hexagonal motifs attached to the lattice [159]. This novel form of sheet known as 'α sheets' has been predicted to be energetically more stable than the flat triangular sheets and has also successfully interpreted the stability of B_{80} fullerenes [160]. Constraining one of the dimensions of these sheets to form boron nanoribbons (BNRs) is expected to reveal interesting properties due to the edges as also observed in graphene nanoribbons [63, 161].

6.2 Computational Details

DFT calculations have been performed using VASP [123]. First principle spin restricted calculations within the LDA with plane wave basis set were carried out using highly efficient ultra soft pseudo potentials (USPP) employing the exchange correlation form of Ceperley and Alder as parameterized by Perdew and Zunger. Calculations were also verified using PAW potentials with exchange correlation of Perdew-Burke-Ernzerhof

(PBE) within the GGA formalism as well as with exchanges correlation of Ceperley and Alder within the LDA. A super cell approach is used such that the distance between two nanoribbons is about 2 nm so as to minimize the interactions between neighboring nanoribbons. The geometry was relaxed using the conjugate gradient algorithm and K – points sampling was done using the Monkhorst Pack scheme. K-point mesh of 1x1x31 was taken to calculate the electronic structure. To assess the charge localization and bonding, the electron localization function (ELF) has been calculated using the formulation of Savin and Silvi [109].

The charge transfer in the system was studied using Bader charge analysis, an intuitive scheme to divide molecules into atom purely based on electronic charge density [162, 163, 164]. This formulation was provided by Richard Bader. Bader charge analysis has been used to calculate the total electronic charge on each atomic site in the 'α-sheet' lattice.

6.3 Nomenclature of Boron Nanoribbons

The nomenclature followed for naming the BNRs merits a small review before proceeding any further. The BNRs are categorized by the arrangement of atoms and hence the width of the nanoribbons. These nanoribbons are derived from 'α-sheet' (Figure 6(a)). The nomenclature criteria similar to that of the graphene nanoribbons [60] are followed. Boron nanoribbons with linear edges are named as N_zLBNR where N_z is specified by the number of zigzag chains across the ribbon width (Figure 6(b)) by including additional boron atoms across the ribbon width at the vacant sites in 'α-sheets'.

For the LBNRs, the atoms at the edges have four neighbors as seen in the B_{20} double ring structure [165].

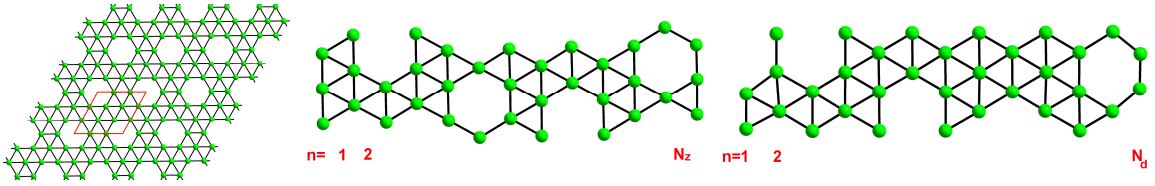

Figure 6.1 (a) 'α-sheet' of boron showing unit cell marked in red (b) linear edged BNR (c) armchair edged BNR.

The armchair edged BNRs are obtained by cutting 'α-sheets' along cells containing vacant sites. Likewise the armchair edged BNRs, N_dABNR are named after the number of dimer lines N_d of additional center boron atoms across the ribbon width (Figure 1(c)).

6.4 Structural Stability and Anti-Aromaticity in Boron Nanoribbons

Cyclic systems with 4nπ electrons that do not fit Huckel's 4n+2 rule for aromaticity are known as anti-aromatic [166] systems. Nanoribbons of approximately the same width up to ~1nm were constructed by restricting the edges of the reconstructed {1221} and the 'α-sheets' in order to compare the stability of both the structures. Based on ab initio calculations it is found that the nanoribbons with linear edges obtained from 'α–sheets' are more stable with respect to those obtained from the reconstructed {1221} sheets by ~0.4eV/atom and those obtained from triangular sheets by ~0.11 eV/atom. The electronic band structure and density of states showed that both the systems having linear edges are metallic. The delocalization of the π orbital from the ELF plot (Figure 6.2(a)) is seen to

be more in nanoribbons derived from α sheets as compared to those from the reconstructed {1221} sheets containing weaker square interlinks (Figure 6.2(b)).

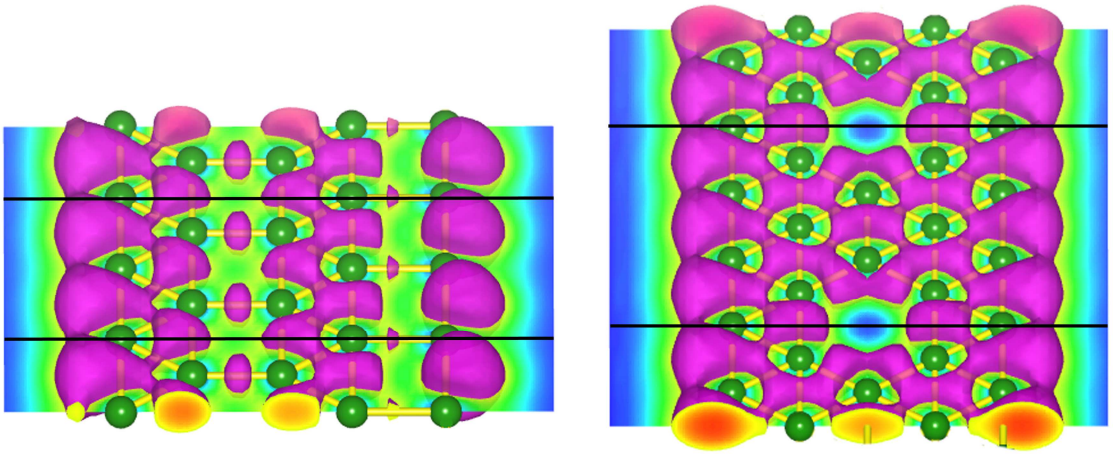

Figure 6.2 Electron localization function plotted for nanoribbon obtained from (a) the reconstructed {1221} sheet (b) the 'α-sheet'.

This delocalization of the π orbital is understood to provide stability to the 'α-sheet'. Boron has an electronic configuration of $1s^2 2s^2 p^1$ and undergoes sp^2 hybridization. This leaves one empty p orbital and the chemical bonding of boron is electron deficient in character. This results in three center triangular BBB units to form an important constituent of boron atomic structures. The instability of reconstructed {1221} nanoribbons can be understood due to the anti-aromaticity associated to the presence of triangle-square-triangle network. The isosurface of the ELF is plotted at value of 0.7. The absence of dangling bonds at the edges in either of the nanoribbons (Figure 6.2(a) and Figure 6.2(b)) suggests that the linear edges of nanoribbons are stable.

The stability of the boron nanoribbons derived from 'α-sheet' is also compared to the nanoribbon structures based on triangular sheets. Flat nanoribbons formed using triangular sheets were relaxed completely. It is observed that these form one of the local

minimum energy states and hence is a metastable state. The positions of the atoms were displaced randomly by about 10% along the three co-ordinate axis and then relaxed we found that a lower energy structure using both USPP and PAW potentials and remains puckered towards the center of the ribbon while it tries to flatten towards the free edges. These structures were however found to be metastable when compared to those obtained from the 'α sheets', with energy/atom 0.04 eV higher. In these puckered structures the atoms towards the edges release the stress by pushing the neighboring atoms away from them. This is observed as increased puckering height of 0.93 Å (Figure 6.3) as compared to 0.82 Å reported earlier for puckered infinite sheets. This tends to form flattened structure toward the ribbon edges while still maintaining the triangular lattice. The atoms at the center remain buckled as the atoms towards the center are pushed inside by atoms at both the edges

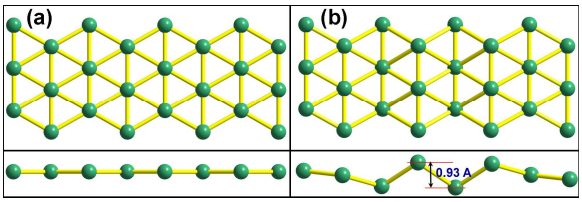

Figure 6.3 Atomic lattice for (a) atomically flat and (b) puckered nanoribbons obtained from triangular sheets.

The stability of the BNRs obtained from the 'α sheets' is determined by the energy of formation, which is defined as $\Delta E = E_{BNRs} - E_{\alpha-sheet}$ for LBNRs with different widths derived from the 'α-sheet'. The energy of formation was calculated using both PAW (GGA) and USPP (LDA) potentials for LBNRs with different widths (Figure 6.4(a)). A similar trend for energy of formation is observed in nanoribbons with LBNRs with asymmetric edges (Figure 6.4(b)). It is observed that the symmetric LBNRs are

more stable as compared to the LBNRs with asymmetric edges. Defining the "hexagon hole density" similar to that for 'α-sheet' as in equation 6.1

$$\eta = \frac{no.\,of\ \ hexagon\,holes}{No.\,of\ \ atoms\,in\,unit\,cell\,of\ \ origional\,triangular\,lattice} \tag{6.1}$$

For nanoribbons with symmetric linear edges, as η approaches a value of 1/9, the LBNRs achieve stability as one approach an infinite 'α-sheet'. The value of η = 1/9 is important because the hexagonal sites can be most symmetrically placed in infinite 'α-sheet'. The inverse of the width also varies linearly with η. Similar trends in variation of η are observed for boron nanoribbons with asymmetric linear edges (Figure 6.4 (b)). The calculated value using GGA-PAW potentials are in excellent agreement with previously published theoretical results [167].

The stability of the nanoribbons is found to increases with increasing width of the nanoribbons and the energy of formation decrease as inverse of the ribbon width. In order to understand the increasing stability of the nanoribbons with increasing width, the bond formation in these nanoribbons is revisited. This can be understood due to increasing the aromaticity by increasing the number of hexagonal boron motifs in the structure. From a doping perspective, the three centered triangular motifs act as donors with surplus of electrons in the antibonding state, while the two centered hexagonal motifs acts as acceptors thus explaining the stability with increasing width of the nanoribbon. Bader charge was calculated for atoms in a unit cell of 'α-sheet'.

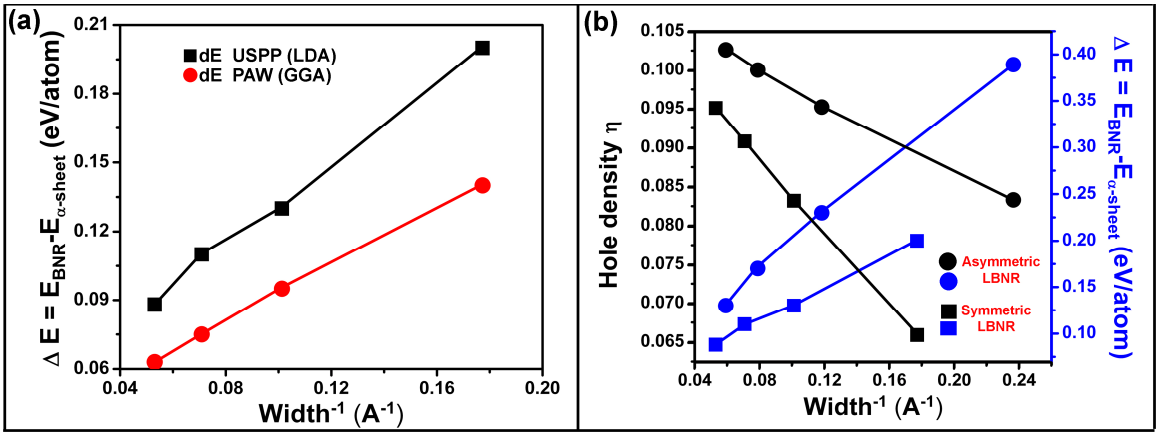

Figure 6.4 (a) Variation of inverse of width with energy of formation shows that the stability of the LBNR is inversely proportional to the width of the nanoribbon. (b) Increase in hole density (η) and stability with increasing width of the nanoribbon for LBNRs with symmetric edges represented by boxes and that for LBNRs with asymmetric edges represented by circles.

A Helium atom, being inert, neither attracts nor donates charge, was placed inside the hole of the hexagonal motif of bare boron 'α-sheet' to determine the transfer of charge from the donor to the acceptor site. It was found that the charge of the He atom increased by ~0.2 electrons while the charge on corresponding boron atom in the bare boron sheet was found to decrease by ~0.5 electrons with rest of the charge being distributed to the neighboring boron atoms on the hexagonal ring. In pure boron 'α-sheet' all the ~0.5 electron charge was found to distribute on the neighboring atoms forming the hexagonal ring.

6.5 Electronic and Atomic Structure of Boron Nanoribbons from 'α-sheet'

The electronic and atomic structure of LBNRs and ABNRs derived from 'α sheet' is further investigated. Each edge atom in LBNRs has four neighboring atoms (Figure 6.5 (a)) for 4LBNR. The electronic band structure and total density of states (TDOS) of

4LBNR is plotted (Figure 6.5 (b)). Similar to boron sheets, the LBNRS are metallic with bands crossing over from conduction band to valence band across the Fermi level. A comparison of the electronic band structure plot and TDOS with 7LBNR and 10LBNR (Figure 6.5 (c) and Figure 6.5 (d)) respectively has been made. Larger concentration of the electronic bands near the Fermi level is observed with increasing width indicating increasing stability of the nanoribbons with the width.

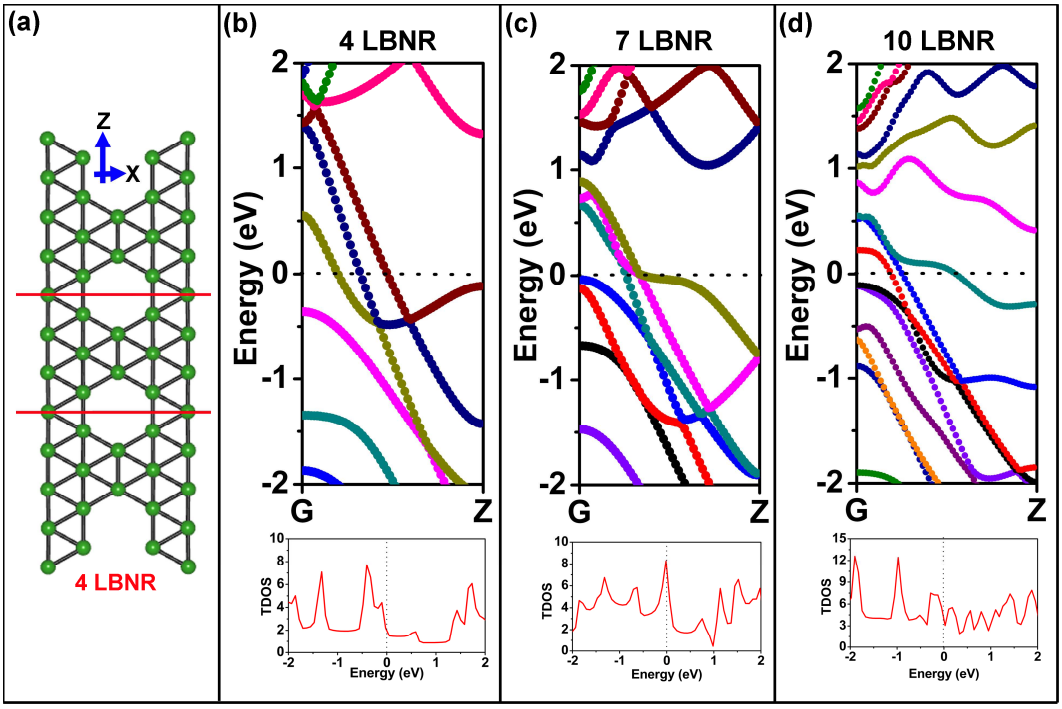

Figure 6.5 (a) Atomic structure of isolated bare 4LBNR with unit cell marked by two red lines across the cross-section. The electronic band structure and the TDOS are shown for (b) 4LBNR, (c) 7LBNR, and (d) 10 LBNR. The Fermi level is adjusted to 0 eV. G is the Gamma point and the ribbon axis is along the Z axis. The Fermi level has been adjusted to 0 eV and is shown by dotted line.

The electronic structure of the armchair edge nanoribbons is investigated to understand their properties. Each edge atoms on the apex in ABNR is surrounded by three neighbors while each atom at the bowl of the edge is surrounded by five atoms. This offers the possibility of edge dangling bonds and the electronic states corresponding

to the edge dangling bonds in the electronic band structure diagram. Further investigation of armchair edged nanoribbons revealed the occurrence of semiconducting behavior in 7ABNR. The electronic band structure of 7ABNR (Figure 6.6 (b)) shows the presence of indirect band gap of about 0.37 eV.

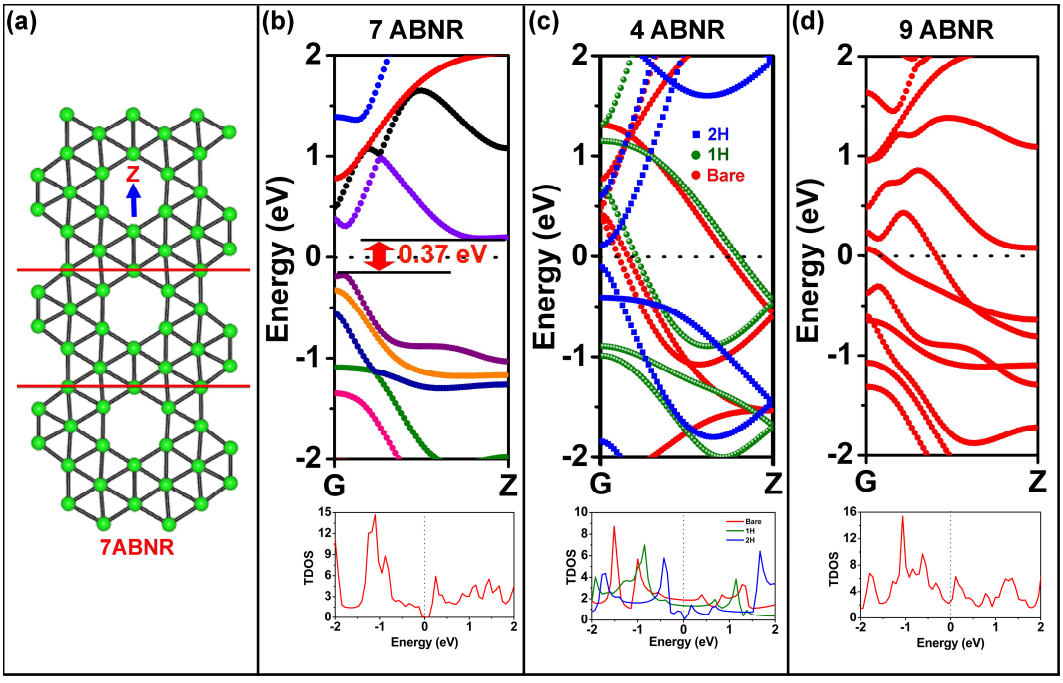

Figure 6.6 (a) Atomic structure of bare 7ABNR with unit cell marked by red lines. (b) Electronic band structure for bare 7ABNR shows indirect band gap of 0.37 eV (c) Electronic band structure for bare 4ABNR and each edge atom saturated by 1H (Olive circles) and 2H atoms (Blue squares). (d) Electronic band structure for bare 9ABNR. The Fermi level is adjusted to 0 eV. G is the Gamma point and the ribbon axis is along the Z axis. The Fermi level is adjusted to 0 eV and shown by dotted line.

It is interesting to note that this semiconducting behavior is neither observed for the narrower 4ABNR nanoribbon as seen in the electronic band structure diagram (Figure 6.6 (c)) nor in wider nanoribbon 9ABNR (Figure 6.6 (d)). The electronic band structure for both these ribbons displays metallic character. Since each apex atom in the armchair edged nanoribbon has three nearest neighbors, up to two Hydrogen (H) atoms can be added to study the contribution of the armchair edges in the band structure of boron

nanoribbons [168, 61]. The changes in the stability and electronic properties of simplified 4ABNR are explored by saturating each apex atom by 1H and 2H atoms. The electronic band structure diagram (Figure 6.6(c) (Olive circles)) shows that although 4ABNR remains metallic when saturated by 1H atom, the number of states crossing the Fermi level decreases with the modification of electronic band structure, thereby indicating the presence of edge states due to the armchair edges near the Fermi level. The optimized B-H bond length was found to be about 1.18 Å, this is very close to the B-$H_{terminal}$ bond length in Diborane [169].However, when 2H atoms are used to saturate the armchair edges the opening of band gap at the Fermi level (Figure 6.6(c) (Blue squares)) is observed indicating semiconducting behavior of the 2H saturated 4ABNR. It is observed that addition of one more H atoms leads to slight weakening of the B-H bond. The stability of the nanoribbons is found to decrease as the edges are saturated with increasing number of H atoms.

CHAPTER 7

ATOMIC AND ELECTRONIC STRUCTURE OF GRAPHENE OXIDE (GO): COMBINED COMPUTATIONAL AND EXPERIMNTAL APPROACH

7.1 Introduction

GO is an important material to study not only because it shows interesting and extraordinary properties by itself, but the underlying graphene sheet also show excellent properties from the perspectives of both fundamental and applied research [135, 170]. There has been much speculations on the chemical structure of GO based only on indirect experimental interpretations [82]. Several attempts have been made experimentally to understand the structural and electronic properties of GO. Based on the analysis of these experimental results several different models have been suggested in which planar graphene sheet have been proposed to bind to oxygen atoms through different functional groups including recently claimed in-plane five- and six- membered-ring lactols [171]. The chemical structure and hence the electronic properties of GO remains a much debated topic to date. The study of GO is important as preliminary investigations suggest interesting promising application and hence a detailed investigation will enable tailoring its properties and help in unleashing its potential device applications.

7.2 Synthesis and Characterization Methodology of GO

GO samples were synthesized by following the modified Hummers method [172] in which large area graphite flakes (Alfa Aesar, 10 mesh, 5g) were oxidized using $NaNO_3$ (3.75g), concentrated H_2SO_4 (375ml) and $KMnO_4$ (22.5g) and vigorously stirred at room temperature for about 72 hrs. Further 700ml of 5 wt% H_2SO_4 solution was added with

continued stirring. The oxidation was further completed by reacting with H_2O_2 (5 wt%) solution under vigorous stirring. The sample was washed several times with 3 wt% HCl in Millipore^{TM} water by ultrasonication and centrifugation. The sample was washed finally with Millipore^{TM} water under ultrasonication and centrifugation at 18,000 RPM many times. This resulted in the suspension of GO flakes in distilled water.

The sample obtained was dried and checked for impurities using energy dispersive x-ray analysis. SEM measurements were performed using JEOL SEM 5300 scanning electron microscope. The chemical composition of the prepared GO samples was determined by CHNS and O measurement. In this technique sample is placed in a tin sample boat. Combustion additive of tungstic anhydride or tin powder is added. The combustion conditions are optimized by increasing oxygen purge and the combustion time. Carbon, hydrogen and nitrogen composition is determined using Perkin-Elmer 2400 element analyzer. The analyzer converts these elements to simple gasses. The product gasses are separated under steady state conditions and measured as a function of thermal conductivity. The oxygen content is determined by pyrolysis to convert oxygen to carbon monoxide. The carbon monoxide is then separated from the pyrolozates under steady state conditions and measured as function of thermal conductivities. The C:O ratio using this technique was determined to be ~2.7:1. The structural phase of GO has been studied using transmission electron microscopy (TEM), selected area electron diffraction (SAED) and synchrotron radiation based x-ray diffraction (XRD) measurements. X-ray diffraction measurements were performed at X14A beam line while the XAS measurements were done at U4B beamline at the National Synchrotron Light Source (NSLS) at Brookhaven national laboratory (BNL). The UV-Vis absorption spectrum was recorded using a

Shimadzu UV-3600 spectrophotometer. The micro Raman measurements were performed using a 2400 grating SPEX 500M spectrometer coupled with liquid nitrogen cooled Spectrum1 CCD detector together with SONY DXC101 camera.

7.3 Computational Details

First principle spin restricted calculations were performed using VASP [123] that implements the pseudopotential approximation and plane wave basis set into the framework of density functional theory. A high energy cutoff of 550 eV was chosen for the plane wave basis. The atoms were relaxed using the CG algorithm such that the forces on each atom were smaller than 0.001 eV/Å. Highly accurate PAW potentials using exchange correlation of Ceperley and Alder were used. The irreducible BZ was sampled using K points generated by the Monkhorst Pack scheme. The accuracy of the calculations were verified by comparing the DOS calculated for AB stacked graphite using VASP (PAW+PBE potentials) to the all electron treatment implemented in WEIN2k [173] (Figure 7.1).

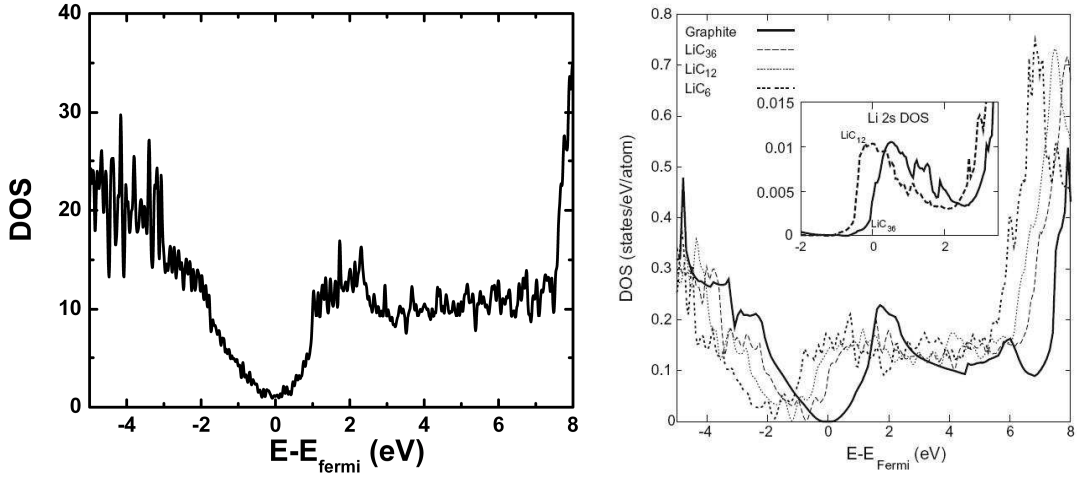

Figure 7.1 DOS calculated for AB stacked graphite using VASP (PAW+PBE potentials) and WEIN2k [173]

The comparison shows the presence of all the essential features in DOS calculated using VASP. The electron localization function (ELF) has been calculated using the formulation of Savin and Silvi [109].

7.4 Atomic Structure of GO: DFT Calculations

The chemical composition of the prepared GO samples determined by CHNS and O measurement provided constraints on structural model for theoretical investigations using ground state DFT. several different models were then constructed by sandwiching graphene sheet between layers of oxygen atoms such that the oxygen atoms are as far apart from each other as possible in the unit cell to avoid interactions amongst themselves. The structure was relaxed completely by minimizing the forces to achieve ground state. The ground state energies of different structures obtained from an exhaustive set of structures were compared to determine the lowest ground state structure. The lowest energy relaxed structure is shown (Figure 7.2 (a)).

Analyzing the relaxed structure it is observed that the oxygen atoms are distributed unequally on both sides of the buckled graphene sheets. Formation of 1, 2 – epoxy bonds as seen in the ELF plot (Figure 7.2(b)) and 1, 3 – diether bridges as seen in ELF plot (Figure 7.2(c)) causes ripples on the graphene sheet straining the graphene lattice with C – C bond lengths up to ~1.52Å. The formation of such 1, 3 – diether bridges due to binding of oxygen dimers have also been reported in ab initio studies of carbon nanotubes [174]. The O – O bond length in the 1, 3 – diether bonds are typically 1.49 Å which is much larger than the experimental bond length of free O_2 (1.207 Å).

Formation of epoxy bonds was found to occur in all configurations of atomic arrangement that were studied.

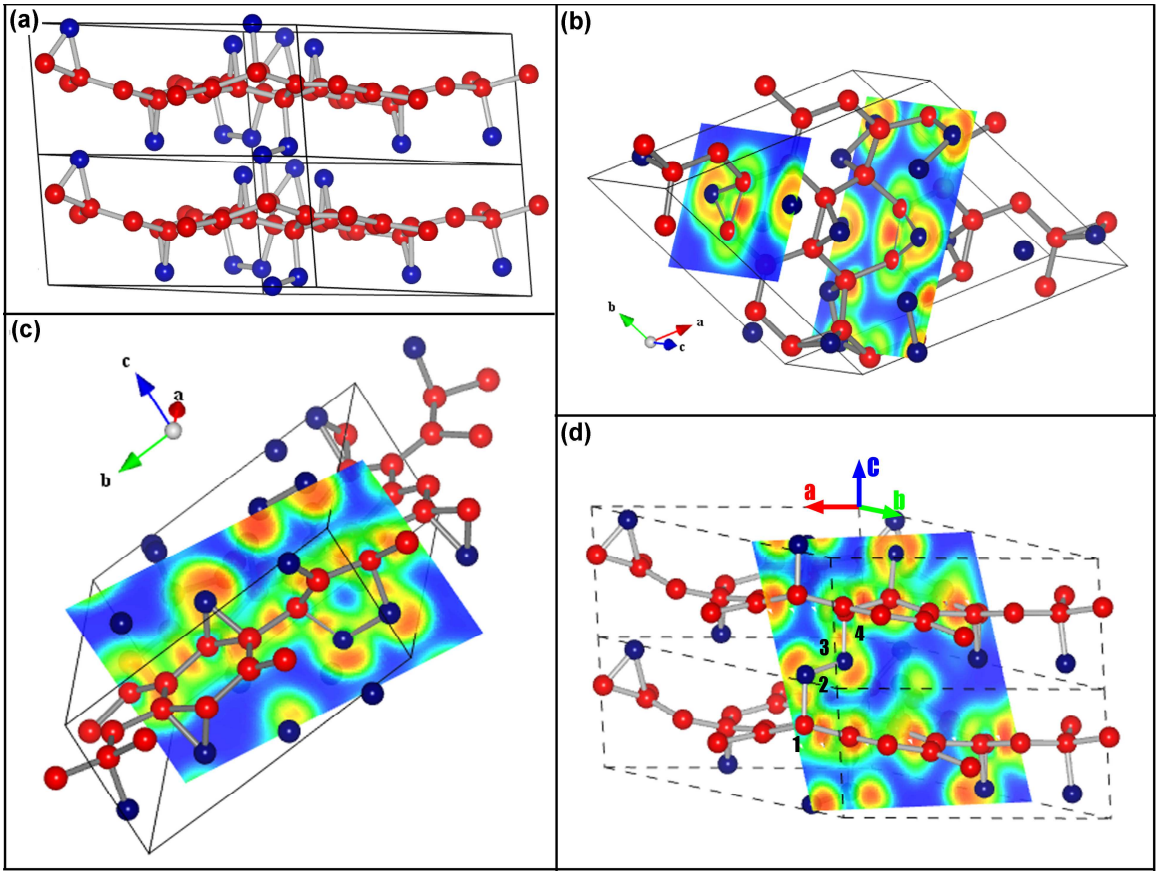

Figure 7.1 (a) Two unit cells showing the relaxed geometry for the lowest ground state atomic structure with oxygen atoms marked as blue and carbon atoms marked as red. Slice showing the ELF for (b) 1, 2 – epoxide bonds, (c) 1, 3 – diether, and (d) peroxide like linkages between different sheets.

It is observed that the GO sheets tend to stick to each other due to the formation of peroxide (R – O – O – R) like linkages between the two mono-layered GO sheets with the O – O bond lengths ~ 1.5 Å. The formation of epoxy bonds is supported by NMR measurements which have shown a ^{13}C chemical shift of ~59.7 ppm corresponding to the chemical shift of ^{13}C epoxide [175, 176]. Based on the calculations it is found that the intercalation of some of free oxygen atoms between two GO sheets is unlikely to occur as

they tend to increase the overall energy of the structure. Analysis of the ab initio calculations leads to the following two major conclusions about the nature of chemical bonding of oxygen with the graphene sheets in GO:

1) Oxygen is bonded to the graphene sheets by 1, 2-epoxide and 1, 3-diether bonds causing the buckling of the graphene sheets.

2) The few layer GO sheets themselves are linked to each other by weak peroxide like linkages.

7.5 Structural Characterization of GO

The structural coherence of the sample was investigated using TEM. GO sample was deposited on the standard holey – carbon – film covered copper grids and loaded into the microscope for TEM measurements to study the GO lattice. The TEM images showed large surface area GO sheets stretching over a few hundred to a few thousand of square nanometers. The TEM image (Figure 7.3 (a)) illustrates large folded sheet of GO sample. The electron diffraction rings obtained from SAED measurements yielded ‘d’ spacing of about 1.2 Å and 2.1 Å. X-ray powder diffraction measurements were performed using synchrotron source with the wavelength of 0.72838 Å for the powdered samples of GO and graphite samples.

The finely powdered sample of GO was placed in Kapton capillary tubes for XRD measurements. The x-ray pattern of the Kapton tube is shown, which was used as the sample holder (Figure 7.3 (c)). The XRD pattern of graphite shows the presence of sharp peaks indicating highly crystalline structure of graphite (Figure 7.3 (d)), while that of GO (Figure 7.3 (e)) shows a combination of broader peaks at higher ‘d’ spacing along with few very sharp features at smaller ‘d’ spacing.

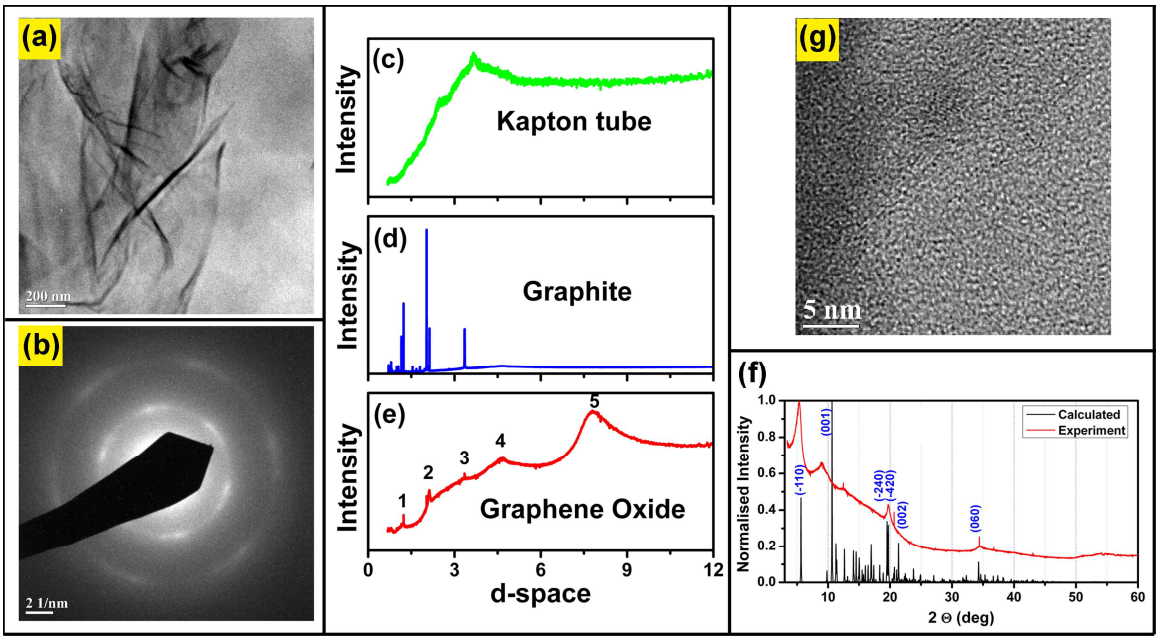

Figure 7.3 (a) TEM micrograph of GO nano sheets (b) electron diffraction pattern from SAED measurements for GO sample. X-ray diffraction pattern for (c) Kapton tube (sample holder), (d) graphite and (e) GO sample measured on X14A beamline of NSLS at BNL using wavelength of 0.72838 Å. The peak positions marked '1' through '5' corresponds to d pacing of 1.2 Å, 2.1 Å, 3.35 Å, 4.65 Å and 7.89 Å respectively. (f) Comparison of calculated (black) and measured (red) x-ray diffraction pattern. (g) HRTEM image of GO.

The XRD peaks marked as '1' and '2' (Figure 7.3 (e)) correspond to the 'd' spacing of 1.2 Å and 2.1 Å as also obtained from SAED measurements. The XRD pattern was calculated for the relaxed structure obtained (Figure 7.2(a)) using DFT is found to be in good qualitative agreement with the measured pattern (Figure 7.3(f)). The presence of broader diffraction peaks in the diffraction pattern indicates very short range atomic coherence. There is a loss of coherence between graphene-like layers. However, in-plane peaks are sharper, showing larger in-plane structural coherence as also observed in a representative HRTEM image (Figure 7.3(g)).

SEM images were acquired to study the surface morphology of the GO samples. The micrographs reveal large area wrinkled sheets (inset Figure 7.4). Energy dispersive

x-ray spectroscopy (EDS/EDX) was performed to perform the elemental analysis. The EDS spectrum reveals the presence of peaks corresponding to carbon, oxygen and silicon (Figure 7.4). The presence of large silicon peak is understood to arise due to the silicon substrate on which the sample was deposited. The absence of any other peaks indicates that the sample is not contaminated with impurities.

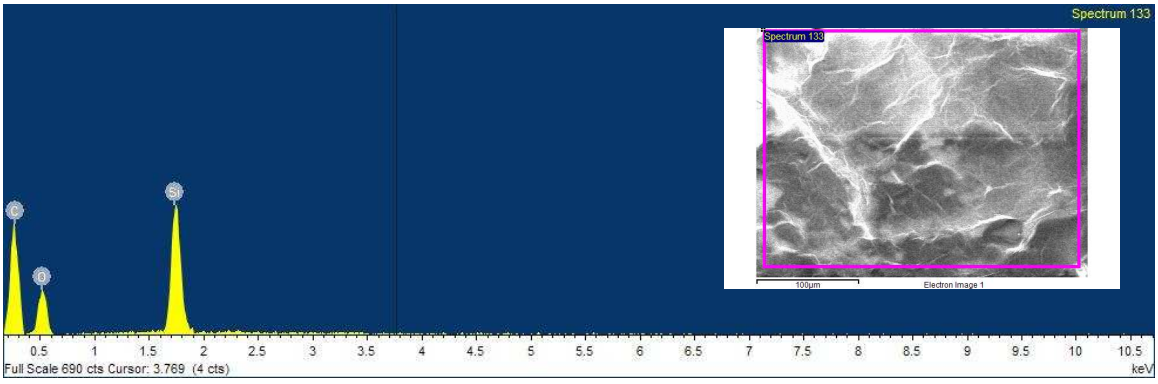

Figure 7.4 EDX/EDS spectrum for the GO sample. The inset shows the SEM micrograph of large area wrinkled sheet.

7.6 Optical Characterization of GO

UV-Vis-NIR absorption spectrum of suspension of GO in distilled water was recorded to estimate the transitions from ground state to the excited states of the chromophores in the sample. The spectrum obtained is in agreement with the previously reported results with characteristic sharp absorption peak at about 233 nm and a broad shoulder at ~290 – 305 nm (Figure 7.5 (a)). The absorption peak at ~233 nm has been assigned to the $\pi \rightarrow \pi^*$ transition of the C = C bonds in the previously reported results. This assignment of the absorption peak at ~233 nm to the $\pi \rightarrow \pi^*$ transition of the C = C bonds seems reasonable in accordance with the predicted structure of our density functional calculation results and are logical when compared to the UV-Vis absorption spectrum of graphene which shows absorption peak ~270nm [177]. This blue shift of the absorption

peak can be understood due to the reduced electronic conjugation increasing the HOMO and LUMO further away. This broad shoulder in the range 295 – 305 nm to the $n \rightarrow \pi^*$ transitions is understood to be due to the presence of epoxide (C – O – C) and peroxide (R – O – O – R) like linkages which is also in accordance to the ab initio calculations.

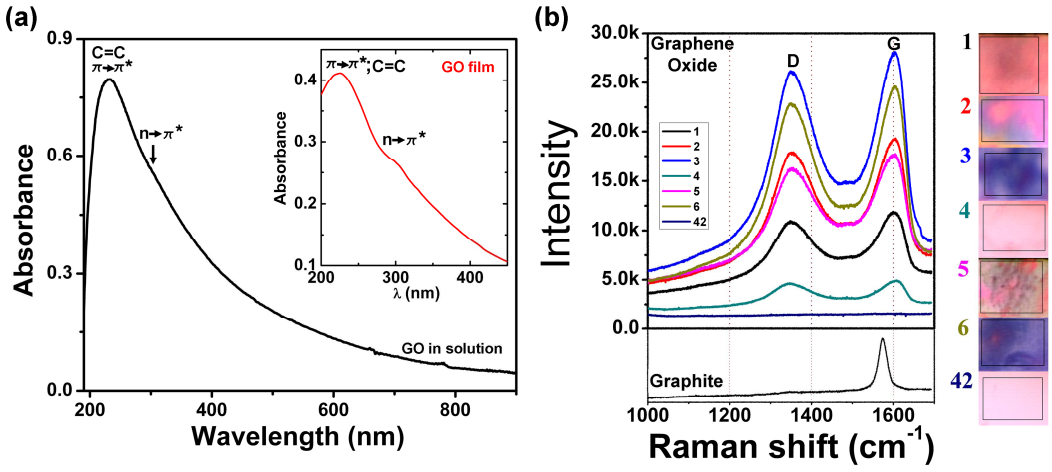

Figure 7.5 (a) UV-Vis absorption spectra of aqueous GO solution with sharp absorption peak ~ 233 nm and a shoulder in the range ~ 295 nm – 305 nm. The inset shows the absorption spectra for GO film indicating the prominence of shoulder in the film sample. (b) Micro Raman measurements for different layers of GO with D band ~1349 cm^{-1} and G band at ~1602 cm^{-1}. The inset below shows the micro Raman spectrum for Graphite flakes with sharp G band at ~ 1574 cm^{-1}.

The broad shoulder becomes very prominent when the spectrum was recorded for a film sample due to the formation of large number of peroxide like linkages in multilayered GO. The broadening of the peaks is also observed with the ageing of the sample over a long period. However, on ultrasonicating and vortexing the aged solution the shoulder diminishes indicating the formation of monolayer GO sheets.

Raman spectroscopy has been employed for non destructive estimation of sample thickness. Micro Raman spectroscopy has been used to qualitatively differentiate different layers of GO in conjugation with an optical microscope. The sample was excited

using green 514.5 nm wavelength of Ar^+ laser. The Raman spectra of GO shows first order D and G bands at 1349 cm^{-1} and 1602 cm^{-1}, where as graphite flakes displays prominent G peak due to tangential vibration of the as the only feature at 1574 cm^{-1} (Figure 7.5 (b)). The D band at ~ 1349 cm^{-1} is very prominent in GO indicating the reduction in size of the in plane sp^2 domains. The Raman spectra were taken at different places on the sample to correlate the optical contrast. The optical contrast between different GO layers was obtained by shining light from a normal white light source and the images were captured using a camera. The intensity of Raman signal was found to change with the sample thickness as observed by different optical contrast detected in the camera. No appreciable shift in the peaks was observed with sample thickness.

7.7 Electronic Structure of GO

The use of soft x-ray measurements can be used to extract the formal valence, co-ordination and subtle geometric distortions. Thus the XANES spectrum can be used to probe the unoccupied band structure of the material. The XANES spectrum for GO sample is measured (Figure 7.6(a)). Since in XANES measurement the electrons are excited to the unoccupied bound and continuum states, the XANES spectrum is analyzed by comparing it to the partial density of states (PDOS) of atoms involved in different types of chemical bonds. The 2p (PDOS) (Figure 7.6(b)) was calculated for the optimized GO structures as well as the most stable Bernal (AB) stacked graphite supercell containing 24 carbon atoms. Before discussing the results any further a sharp rise in the x-ray absorption spectra at ~286.2 eV is noted indicating the K shell threshold of carbon. The C K-edge absorption edge is proportional to density of unfilled p states.

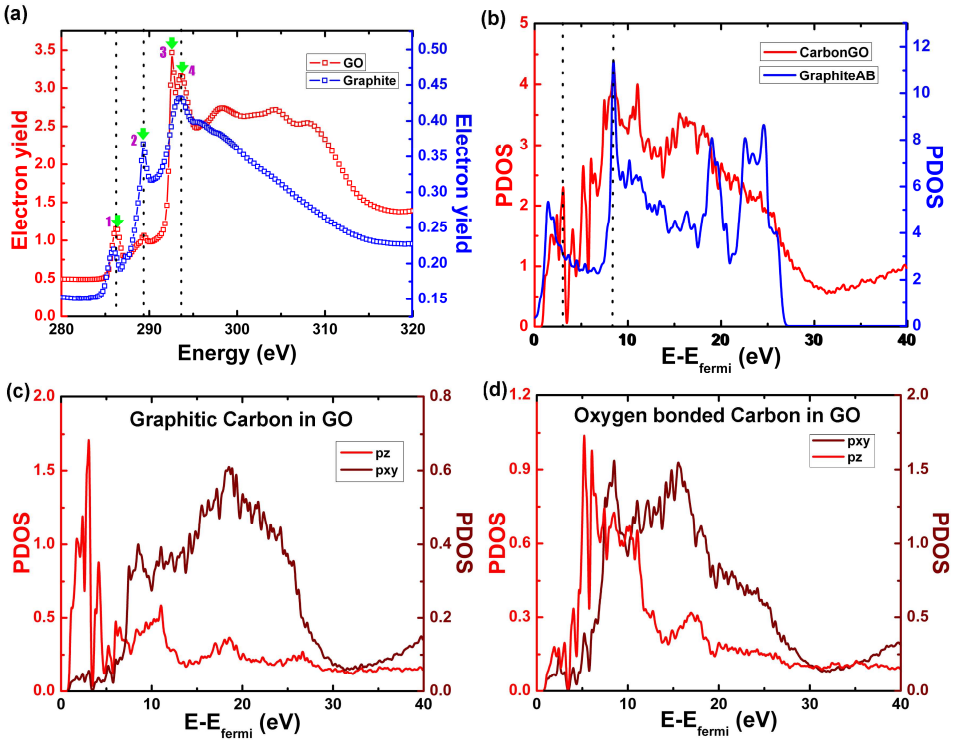

Figure 7.6 (a) The carbon K-edge XANES cross section of GO. The peaks are indicated by green arrows and labeled '1'-'4'. The absorption edge at 286.2 eV marked as '1' is due to $1s \rightarrow \pi^*$. The broadening of absorption peak at ~289.3 eV marked as '2' corresponds to C – O and C – O – O – C linkages while the absorption peaks around 292.5 eV and ~293.5 eV marked as '3' and '4' respectively indicates presence of σ* and high energy π* resonances. (b) Calculated PDOS for p orbitals for carbon atoms in the relaxed GO structure and the Bernal stacked graphite. (c) Calculated PDOS for graphitic carbon atoms in GO. (d) Calculated PDOS for carbon atoms bonded to oxygen atoms forming 1, 2-epoxy; 1, 3-diether and peroxide like linkages in GO.

The site projected PDOS for graphitic carbon atoms (Figure 7.6(c)) shows a prominent edge corresponding to the edges at 286.2 eV in the XANES spectra marked as '1' (Figure 7.6(a)); hence, this can be assigned to the out of plane $1s \rightarrow \pi^*$ transition indicating the presence of graphitic regions. The hypsochromic shift of the absorption edge observed in the experiment for GO is also observed in the calculated site projected PDOS for the carbon atoms in the relaxed GO lattice (Figure 7.6(b)) indicating reduced electronic conjugation (higher ionization).

Analysis of site projected PDOS for carbon atoms indicate that the absorption peaks at 292.5eV and 293.5 eV marked as '3' and '4' (Figure 7.6(a)) are associated with the presence of σ^* and high energy π^* resonances in agreement with the electron energy loss spectra (EELS) in GO [82] sample and is also observed in graphite [178, 179] samples. Along with the π^* and σ^* resonance peaks an additional broadened peak at ~289.3 eV marked as '2' (Figure 7.6(a)) was observed. A detailed analysis of the site projected PDOS (Figure 7.6(d)) for carbon atoms linked to oxygen atoms in the relaxed GO lattice reveal that this broadening of the absorption peak at ~289.3 eV in the measured XANES spectrum is related to the 1, 2 epoxy; 1, 3 diether and peroxide like linkages in accordance with previously reported results for C – O bonds [180] and C – O – C bonds [181]. This is in agreement with the previously reported results that the species containing ether groups are more thermally stable than species containing π^*carbonyl orbitals [182]. These observations support the nature of oxygen bonding as predicted by our density functional calculations. The peak itself at ~289.3 eV marked as '2' (Figure 7.6(a)) in GO matches exactly with the corresponding sharp peak in graphite and has been attributed to the inter layer state by theoretical predictions [183]. Similar features have been reported previously in carbon K-edge near edge XAS studies of graphite [184, 185] in agreement to the measurements.

The oxygen K-edge near edge x-ray absorption (XAS) spectrum was used to further develop insight into the nature of oxygen bonding with the graphene sheet in GO [172]. Three distinctive features in the O K-edge XAS spectrum at ~540.5 eV, ~536.7 eV, and ~533.2 eV are observed (Figure 7.7(a)).

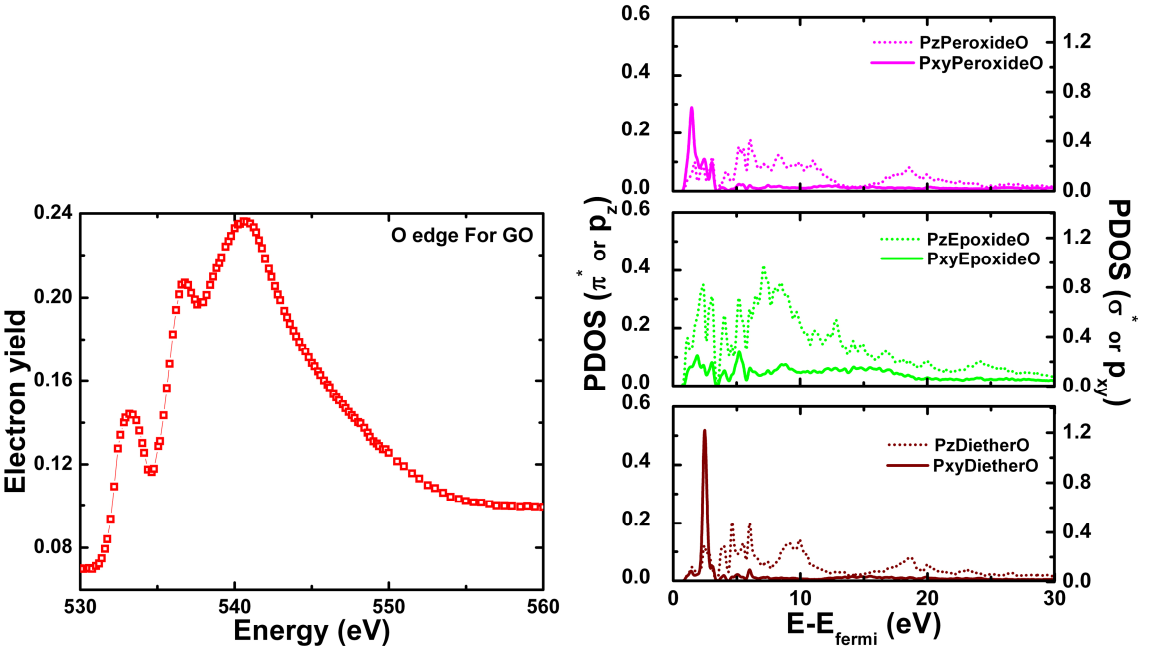

Figure 7.7 (a) Oxygen K-near edge XANES spectrum for GO sample shows absorption resonances at ~533.2 eV, ~536.7 eV, and ~540.5 eV. (b) Site projected PDOS for Oxygen atoms bonded to puckered graphene sheets. The dotted lines show the pz, while the solid lines display the pxy component.

Detailed analysis of the PDOS of the oxygen atoms (Figure 7.7(b)) shows that the absorption peaks at ~540.5 eV may possibly be due to higher order π^* (p_z) resonance of the 1, 2 – epoxy, 1, 3 – diether and the peroxide like linkages in the GO sample, while the peak at and ~536.7 eV seems to arise form $\sigma^*(p_{xy})$ resonance of diether bonds. Where as the absorption peak at 533.2 we believe may be possibly due to the $\sigma^*(p_{xy})$ or $\pi^*(p_z)$ resonance of the C – O bonds from the peroxide and epoxide bonds respectively. The O K-edge XANES spectrum is expected to be modified for purely monolayer sheets of graphene with the disappearance of peaks corresponding to σ^* (p_{xy}) resonances due to the disruption of peroxide like linkages. No absorption edges corresponding to that of molecular oxygen [186] are observed suggesting the possibility of intercalation of molecular oxygen can be ignored safely.

CHAPTER 8

SUMMARY AND FUTURE WORK

8.1 Summary of the Electronic and Atomic Structure Studies

Density functional studies were performed on different nanostructures of carbon such as nanoribbons and nanotubes. These studies were further extended to other nanosystems such as functionalized graphene sheets namely GO and nanosystems made of boron. Experiments were performed to compliment the findings obtained using DFT calculations.

GNRs are widely accepted as precursors to single walled nanotubes. A novel method describing the production of chirality/ diameter controlled SWCNTs from bilayered GNRs have been investigated using ground state DFT. The proposed method may also be used to prepare an array of such tailored SWCNTs. It is observed that the unsaturated edges of zigzag edged graphene nanoribbons are highly reactive due to the presence of states corresponding to unsaturated dangling bonds near the Fermi level. Interactions between the layers in the bilayered system due to intrinsic edge reactivity coupled with the presence of dangling bonds is found to be responsible for nanotube formation. However, in the case of armchair edged nanoribbons, the dangling bonds at the edges are healed slightly as well as the amplitude of the intrinsic edge ripples is also found to be smaller, demanding an external stimulus to overcome the energy barrier of ~0.1 eV/atom for nanotube formation. The proposed study explores pressure as an external stimulus to achieve this. The advantage of the proposed method is that it does not require any precise functionalization or rolling of the nanoribbons for nanotube formation.

SWCNTs contains sp^3 hybridized carbon atoms with one unsaturated sp^3 hybrid orbital. This makes the nanotubes 'sticky' in order to saturate the dangling sp^3 hybrid orbital. Thus the carbon nanotubes like to be bundled; however, the interaction between two nanotubes is understood to be mostly vdW interactions. This bundling of the nanotubes is understood to perturb the Hamiltonian at any k point where two bands cross, resulting in opening of a pseudo band gap at the Fermi level for armchair SWCNTs. The band structure is also found to be influenced in the case of zigzag SWCNTs. This opening of the band gap is in agreement with the previously reported experimental and tight binding results.

Systematic studies of the effect of hydrostatic pressure on SWCNT bundles have suggested that nanotubes with chiral indices (3n+3, 3n+3) deform to hexagonal cross-sections at very low pressures before deforming to flattened racetrack/ peanut shaped cross-sections. Analysis reveals that the hexagonal cross-section phase is a metastable phase and the prediction of occurrences of such phases is in agreement to the experiment results published by other groups.

High pressure studies on SWCNTs have brought to light a highly stable and a novel quasi two-dimensional phase of carbon containing interacting flattened sheets of interlinked carbon nanotubes. The occurrence of a high pressure phase of carbon similar to that investigated using DFT techniques is in agreement with the experimentally observed phase under extremely high pressures conditions reported recently. Theoretical results indicate that the formation of such phase is marked by abrupt changes in the relative energy/Pressure and relative volume/ pressure graphs indicating first order phase transition. The formation of the interlinked quasi two-dimensional phase is dictated by

breaking of symmetry assisting in availability of highly localized electron cloud density enabling in formation of interlinked structures. The formation of this novel phase is also found to influence the electron band structure.

The atomic and electronic structure studies were extended to boron nanosystems and functionalized carbon nanostructures. The structural stability of boron nanoribbons was studied. It is observed that nanoribbons obtained from the 'α-sheet' stabilize due to the localization of the π electrons. Charge transfer from the donor three centered triangular motifs to the acceptor two centered hexagonal motifs was understood to provide stability to these nanoribbons. This was also observed as increasing stability of nanoribbons with the width of the ribbon which was associated with increasing acceptor hexagonal sites into the structure. DFT studies also have indicated the presence of semiconducting boron nanostructures.

GO belongs to the category of functionalized carbon nanosystems with random functionalization. A combined theoretical and experimental approach was adopted to determine the chemical structure and local electronic structure of this material. Structural optimization has revealed that the ground state structure of GO is a puckered sheet linked to oxygen atoms by epoxy and diether bonds. Multilayered sheets of graphene oxide are understood to be linked by peroxide like linkages. Structural characterizations such as TEM, SAED and XRD have shown the absence of long range order in the atomic structure of GO, hence indicating random functionalization of the underlying graphene sheets in GO. Synchrotron radiation was used to study the electronic structure of GO based on carbon and oxygen K-edge XANES spectra. DFT derived site projected PDOS has been utilized to interpret and understand the electronic states. The data exhibits

characteristics spectral features reflecting the specific properties of unoccupied PDOS in GO and point to its unique structural features relative to graphene.

8.2 Proposed Future Studies

Comprehensive studies of carbon and boron nanostructures have been presented using ground state DFT techniques and state of the art synchrotron radiation based techniques. The current research topic which is still being explored is GO. The following tasks needs to be completed as a future work to substantiate our present findings on this material.

a) Accurate simulations of XANES at O and C K-edges using multiple scattering methods.

b) Simulation of infrared (IR) and Raman spectra.

c) More detailed structural analysis using wide angle x-ray diffraction measurements up to long $q = 4\pi \sin\theta/\lambda$. The pair distribution function method will enable both local and long range structure determination $0 \rightarrow 50$ Å [187].

d) Extension of present studies of graphene and boron nanoribbons to other systems such as silicon.

e) Acquisition and studies of single chirality single walled carbon nanotubes under pressure to test the DFT predictions. Studies will include XRD, IR and x-ray absorption measurements.

REFERENCES

1 Feynman, R.P., There's plenty of room at the bottom. *Proceedings of the American Physical Society Annual Meeting* (1959).

2 Kroto, H.W., Heath, J.R., O'Brien, S.C., Curl, R.F., & Smalley, R.E., C60: Buckminsterfullerene. *Nature* 318 (6042), 162 (1985).

3 Iijima, S., Helical microtubules of graphitic carbon. *Nature* 354 (6348), 56 (1991).

4 Novoselov, K.S. *et al.*, Electric field effect in atomically thin carbon films. *Science* 306 (5696), 666 (2004).

5 Sofo, J.O., Chaudhari, A.S., & Barber, G.D., Graphane: A two-dimensional hydrocarbon. *Physical Review B* 75 (15), 153401 (2007).

6 Kim, P. & Lieber, C.M., Nanotube nanotweezers. *Science* 286 (5447), 2148 (1999).

7 JensenK, Kim, K., & ZettlA, An atomic-resolution nanomechanical mass sensor. *Nature Nanotechnology* 3 (9), 533 (2008).

8 Rueckes, T. *et al.*, Carbon nanotube-based nonvolatile random access memory for molecular computing. *Science* 289 (5476), 94 (2000).

9 Qi, P. *et al.*, Towards large arrays of multiplex functionalized carbon nanotube sensors for highly sensitive and selective molecular detection. *Nano Letters* 3 (3), 347 (2003).

10 Kaul, A.B., Wong, E.W., Epp, L., & Hunt, B.D., Electromechanical carbon nanotube switches for high-frequency applications. *Nano Letters* 6 (5), 942 (2006).

11 Kymakis, E. & Amaratunga, G.A.J., Single-wall carbon nanotube/conjugated polymer photovoltaic devices. *Applied Physics Letters* 80 (1), 112 (2002).

12 Keefer, E.W., Botterman, B.R., Romero, M.I., Rossi, A.F., & Gross, G.W., Carbon nanotube coating improves neuronal recordings. *Nature Nanotechnology* 3 (7), 434 (2008).

13 Bianco, A., Kostarelos, K., & Prato, M., Applications of carbon nanotubes in drug delivery. *Current Opinion in Chemical Biology* 9 (6), 674 (2005).

14 Michael, G.S., Falls, E.M., Ziober, B.L., & Bau, H.H., Carbon nanopipettes for cell probes and intracellular injection. *Nanotechnology* 19 (1), 015101 (2008).

15 Yan, Q. *et al.*, Intrinsic current-voltage characteristics of graphene nanoribbon transistors and effect of edge doping. *Nano Letters* 7 (6), 1469 (2007).

16 Sevincli, H., Topsakal, M., & Ciraci, S., Superlattice structures of graphene-based armchair nanoribbons. *Physical Review B* 78 (24), 245402 (2008).

17 Dikin, D.A. *et al.*, Preparation and characterization of graphene oxide paper. *Nature* 448 (7152), 457 (2007).

18 Eda, G., Fanchini, G., & Chhowalla, M., Large-area ultrathin films of reduced graphene oxide as a transparent and flexible electronic material. *Nature Nanotechnology* 3 (5), 270 (2008).

19 Shin, H.-j., Choi, J.-y., & Yoon, S.-m., United States (2009).

20 Robinson, J.T. *et al.*, Wafer-scale reduced graphene oxide films for nanomechanical devices. *Nano Letters* 8 (10), 3441 (2008).

21 Liu, Z., Robinson, J.T., Sun, X., & Dai, H., PEGylated nanographene oxide for delivery of water-insoluble cancer drugs. *Journal of the American Chemical Society* 130 (33), 10876 (2008).

22 Liu, Z. *et al.*, Nonlinear optical properties of graphene oxide in nanosecond and picosecond regimes. *Applied Physics Letters* 94 (2), 021902 (2009).

23 Lu, G., Ocola, L.E., & Chen, J., Gas detection using low-temperature reduced graphene oxide sheets. *Applied Physics Letters* 94 (8), 083111 (2009).

24 Fan, X. *et al.*, Deoxygenation of exfoliated graphite oxide under alkaline conditions: A green route to graphene preparation. *Advanced Materials* 20 (23), 4490 (2008).

25 Tse, J.S., Solid-state chemistry: Boron charged under pressure. *Nature* 457 (7231), 800 (2009).

26 Oganov, A.R. *et al.*, Ionic high-pressure form of elemental boron. *Nature* 457 (7231), 863 (2009).

27 Eremets, M.I., Struzhkin, V.V., Mao, H.-k., & Hemley, R.J., Superconductivity in Boron. *Science* 293 (5528), 272 (2001).

28 Kunstmann, J. & Quandt, A., Broad boron sheets and boron nanotubes: An ab initio study of structural, electronic, and mechanical properties. *Physical Review B* 74 (3), 035413 (2006).

29 Lau, K.C., Pandey, R., Pati, R., & Karna, S.P., Theoretical study of electron transport in boron nanotubes. *Applied Physics Letters* 88 (21), 212111 (2006).

30 Ciuparu, D., Klie, R.F., Zhu, Y., & Pfefferle, L., Synthesis of pure boron single-wall nanotubes. *The Journal of Physical Chemistry B* 108 (13), 3967 (2004).

31 Boustani, I. & Quandt, A., Nanotubules of bare boron clusters: Ab initio and density functional study. *Europhysics Letters* 39 (5), 527 (1997).

32 Becke, A.D., Density-functional thermochemistry. III. The role of exact exchange. *The Journal of Chemical Physics* 98 (7), 5648 (1993).

33 Tretiak, S., Triplet state absorption in carbon nanotubes: A TD-DFT study. *Nano Letters* 7 (8), 2201 (2007).

34 Rao, A.M. *et al.*, Diameter-selective raman scattering from vibrational modes in carbon nanotubes. *Science* 275 (5297), 187 (1997).

35 Jishi, R.A., Dresselhaus, M.S., & Dresselhaus, G., Symmetry properties of chiral carbon nanotubes. *Physical Review B* 47 (24), 16671 (1993).

36 Zhang, Z. & Lieber, C.M., Nanotube structure and electronic properties probed by scanning tunneling microscopy. *Applied Physics Letters* 62 (22), 2792 (1993).

37 Olk, C.H. & Heremans, J.P., Scanning tunneling spectroscopy of carbon nanotubes. *Journal of Materials Research* 9 (2), 259 (1994).

38 Hamada, N., Sawada, S.-i., & Oshiyama, A., New one-dimensional conductors: Graphitic microtubules. *Physical Review Letters* 68 (10), 1579 (1992).

39 Saito, R., Fujita, M., Dresselhaus, G., & Dresselhaus, M.S., Electronic structure of graphene tubules based on C60. *Physical Review B* 46 (3), 1804 (1992).

40 Wilder, J.W.G., Venema, L.C., Rinzler, A.G., Smalley, R.E., & Dekker, C., Electronic structure of atomically resolved carbon nanotubes. *Nature* 391 (6662), 59 (1998).

41 Venema, L.C. *et al.*, Spatially resolved scanning tunneling spectroscopy on single-walled carbon nanotubes. *Physical Review B* 62 (8), 5238 (2000).

42 Odom, T.W., Huang, J.-L., Kim, P., & Lieber, C.M., Structure and electronic properties of carbon nanotubes. *The Journal of Physical Chemistry B* 104 (13), 2794 (2000).

43 Odom, T.W., Huang, J.-L., Kim, P., & Lieber, C.M., Atomic structure and electronic properties of single-walled carbon nanotubes. *Nature* 391 (6662), 62 (1998).

44 Kim, P., Odom, T.W., Huang, J.-L., & Lieber, C.M., Electronic density of states of atomically resolved single-walled carbon nanotubes: Van Hove singularities and end states. *Physical Review Letters* 82 (6), 1225 (1999).

45 Murakami, Y., Einarsson, E., Edamura, T., & Maruyama, S., Polarization dependence of the optical absorption of single-walled carbon nanotubes. *Physical Review Letters* 94 (8), 087402 (2005).

46 Pichler, T. *et al.*, Localized and delocalized electronic states in single-wall carbon nanotubes. *Physical Review Letters* 80 (21), 4729 (1998).

47 Bronikowski, M.J., Willis, P.A., Colbert, D.T., Smith, K.A., & Smalley, R.E., presented at the The 47th international symposium: Vacuum, thin films, surfaces/interfaces, and processing NAN06, Boston, Massachusetts (USA), 2001 (unpublished).

48 O'Connell, M.J. *et al.*, Band gap fluorescence from individual single-walled carbon nanotubes. *Science* 297 (5581), 593 (2002).

49 Bethune, D.S. *et al.*, Cobalt-catalysed growth of carbon nanotubes with single-atomic-layer walls. *Nature* 363 (6430), 605 (1993).

50 Dresselhaus, M.S., Dresselhaus, G., Jorio, A., Souza Filho, A.G., & Saito, R., Raman spectroscopy on isolated single wall carbon nanotubes. *Carbon* 40 (12), 2043 (2002).

51 Holden, J.M. *et al.*, Raman scattering from nanoscale carbons generated in a cobalt-catalyzed carbon plasma. *Chemical Physics Letters* 220 (3-5), 186 (1994).

52 Iijima, S. & Ichihashi, T., Single-shell carbon nanotubes of 1-nm diameter. *Nature* 363 (6430), 603 (1993).

53 Tohji, K. *et al.*, Purifying single-walled nanotubes. *Nature* 383 (6602), 679-679 (1996).

54 Jorio, A. *et al.*, Structural (n, m) determination of isolated single-wall carbon nanotubes by resonant raman scattering. *Physical Review Letters* 86 (6), 1118 (2001).

55 Kosynkin, D.V. *et al.*, Longitudinal unzipping of carbon nanotubes to form graphene nanoribbons. *Nature* 458 (7240), 872 (2009).

56 Tapaszto, L., Dobrik, G., Lambin, P., & Biro, L.P., Tailoring the atomic structure of graphene nanoribbons by scanning tunnelling microscope lithography. *Nature Nanotechnology* 3 (7), 397 (2008).

57 Li, X., Wang, X., Zhang, L., Lee, S., & Dai, H., Chemically derived, ultrasmooth graphene nanoribbon semiconductors. *Science* 319 (5867), 1229 (2008).

58 Yang, X. *et al.*, Two-dimensional graphene nanoribbons. *Journal of the American Chemical Society* 130 (13), 4216 (2008).

59 Jiao, L., Zhang, L., Wang, X., Diankov, G., & Dai, H., Narrow graphene nanoribbons from carbon nanotubes. *Nature* 458 (7240), 877 (2009).

60 Nakada, K., Fujita, M., Dresselhaus, G., & Dresselhaus, M.S., Edge state in graphene ribbons: Nanometer size effect and edge shape dependence. *Physical Review B* 54 (24), 17954 (1996).

61 Son, Y.-W., Cohen, M.L., & Louie, S.G., Energy gaps in graphene nanoribbons. *Physical Review Letters* 97 (21), 216803 (2006).

62 Yoffe, A.D., Semiconductor quantum dots and related systems: electronic, optical, luminescence and related properties of low dimensional systems. *Advances in Physics* 50 (1), 1 (2001).

63 Han, M.Y., Özyilmaz, B., Zhang, Y., & Kim, P., Energy band-gap engineering of graphene nanoribbons. *Physical Review Letters* 98 (20), 206805 (2007).

64 Stampfer, C. *et al.*, Energy gaps in etched graphene nanoribbons. *Physical Review Letters* 102 (5), 056403 (2009).

65 Fujita, M., Wakabayashi, K., Nakada, K., & Kusakabe, K., Peculiar localized state at zigzag graphite edge. *Journal of the Physical Society of Japan* 65 (7), 1920 (1996).

66 Rudberg, E., Salek, P., & Luo, Y., Nonlocal exchange interaction removes half-metallicity in graphene nanoribbons. *Nano Letters* 7 (8), 2211 (2007).

67 Son, Y.-W., Cohen, M.L., & Louie, S.G., Half-metallic graphene nanoribbons. *Nature* 444 (7117), 347 (2006).

68 Wimmer, M., Adagideli, I., Berber, S., Tománek, D., & Richter, K., Spin currents in rough graphene nanoribbons: Universal fluctuations and spin injection. *Physical Review Letters* 100 (17), 177207 (2008).

69 Novoselov, K.S. *et al.*, Two-dimensional gas of massless Dirac fermions in graphene. *Nature* 438 (7065), 197 (2005).

70 Zhang, Y., Tan, Y.-W., Stormer, H.L., & Kim, P., Experimental observation of the quantum Hall effect and Berry's phase in graphene. *Nature* 438 (7065), 201 (2005).

71 Zhang, Y. *et al.*, Landau-level splitting in graphene in high magnetic fields. *Physical Review Letters* 96 (13), 136806 (2006).

72 Huang, Y.C. & et al., Magnetic and quantum confinement effects on electronic and optical properties of graphene ribbons. *Nanotechnology* 18 (49), 495401 (2007).

73 Hsu, H. & Reichl, L.E., Selection rule for the optical absorption of graphene nanoribbons. *Physical Review B* 76 (4), 045418 (2007).

74 Zhou, J. & Dong, J., Vibrational property and Raman spectrum of carbon nanoribbon. *Applied Physics Letters* 91 (17), 173108 (2007).

75 Brodie, B.C., On the Atomic Weight of Graphite. *Philosophical Transactions of the Royal Society of London* 149, 249 (1859).

76 Hummers, W.S. & Offeman, R.E., Preparation of graphitic oxide. *Journal of the American Chemical Society* 80 (6), 1339 (1958).

77 Luo, Z., Lu, Y., Somers, L.A., & Johnson, A.T.C., High yield preparation of macroscopic graphene oxide membranes. *Journal of the American Chemical Society* 131 (3), 898 (2009).

78 Stankovich, S. *et al.*, Graphene-based composite materials. *Nature* 442 (7100), 282 (2006).

79 Drude, P., Bestimmung optischer konstanten der metalle. *Wiedemanns Annalen* 39, 481 (1897).

80 Park, S. *et al.*, Colloidal suspensions of highly reduced graphene oxide in a wide variety of organic solvents. *Nano Letters* 9 (4), 1593 (2009).

81 Schniepp, H.C. *et al.*, Functionalized single graphene sheets derived from splitting graphite oxide. *The Journal of Physical Chemistry B* 110 (17), 8535 (2006).

82 Mkhoyan, K.A. *et al.*, Atomic and electronic structure of graphene-oxide. *Nano Letters* 9 (3), 1058 (2009).

83 Lerf, A., He, H., Forster, M., & Klinowski, J., Structure of graphite oxide revisited. *The Journal of Physical Chemistry B* 102 (23), 4477 (1998).

84 Jung, I., Dikin, D.A., Piner, R.D., & Ruoff, R.S., Tunable electrical conductivity of individual graphene oxide sheets reduced at "low" temperatures. *Nano Letters* 8 (12), 4283 (2008).

85 Gomez-Navarro, C. *et al.*, Electronic transport properties of individual chemically reduced graphene oxide sheets. *Nano Letters* 7 (11), 3499 (2007).

86 Thomson, J.J., Cathode rays. *Philosophical Magazine Series 5* 44, 310 (1897).

87 Ashcroft, N.W. & Mermin, N.D., Solid state physics. *Thomson Learning Inc.*, pp1-6 (1975).

88 Dirac, P.A.M., On the theory of quantum mechanics. P*roceedings of the Royal Society, Series A* 112, 661 (1926).

89 Goringe, C.M. & et al., Tight-binding modelling of materials. *Reports on Progress in Physics* 60 (12), 1447 (1997).

90 Foulkes, W.M.C. & Haydock, R., Tight-binding models and density-functional theory. *Physical Review B* 39 (17), 12520 (1989).

91 Mitin, A.V., Exact solution of the Hartree-Fock equation for the H2 molecule in the linear-combination-of-atomic-orbitals approximation. *Physical Review A* 62 (1), 010501 (2000).

92 Parr, R.G., Density functional theory. *Annual Review of Physical Chemistry* 34 (1), 631 (1983).

93 Hohenberg, P. & Kohn, W., Inhomogeneous electron gas. *Physical Review* 136 (3B), B864 (1964).

94 Martin, R.M., Electronic structure basic theory and practical methods. *Cambridge University Press*, pp119-170 (2005).

95 Kohn, W. & Sham, L.J., Self consistent equations including exchange and correlation effects. *Physical Review* 140 (4A), A1133 (1965).

96 Perdew, J.P., Burke, K., & Ernzerhof, M., Generalized gradient aproximation made simple. *Physical Review Letters* 77 (18), 3865 (1996).

97 Perdew, J.P. & Yue, W., Accurate and simple density functional for the electronic exchange energy: Generalized gradient approximation. *Physical Review B* 33 (12), 8800 (1986).

98 Tao, J., Perdew, J.P., Staroverov, V.N., & Scuseria, G.E., Climbing the density functional ladder: Nonempirical meta-generalized gradient approximation designed for molecules and solids. *Physical Review Letters* 91 (14), 146401 (2003).

99 Herman, F., Van Dyke, J.P., & Ortenburger, I.B., Improved statistical exchange approximation for inhomogeneous many electron systems. *Physical Review Letters* 22 (16), 807 (1969).

100 Becke, A.D., Density-functional exchange-energy approximation with correct asymptotic behavior. *Physical Review A* 38 (6), 3098 (1988).

101 Perdew, J.P. & Wang, Y., Accurate and simple analytic representation of the electron-gas correlation energy. *Physical Review B* 45 (23), 13244 (1992).

102 Perdew, J.P., Burke, K., & Ernzerhof, M., Generalized gradient approximation made simple. *Physical Review Letters* 77 (18), 3865 (1996).

103 Singh, D.J. & Nordstrom, L., Planewaves, pseudopotentials and the LAPW method. *Springer*, pp23-36 (Second edition).

104 Phillips, J.C. & Kleinman, L., New method for calculating wave functions in crystals and molecules. *Physical Review* 116 (2), 287 (1959).

105 Herring, C., A new method for calculating wave functions in crystals. *Physical Review* 57 (12), 1169 (1940).

106 Kleinman, L. & Bylander, D.M., Efficacious form for fodel pseudopotentials. *Physical Review Letters* 48 (20), 1425 (1982).

107 Vanderbilt, D., Soft self-consistent pseudopotentials in a generalized eigenvalue formalism. *Physical Review B* 41 (11), 7892 (1990).

108 Becke, A.D. & Edgecombe, K.E., A simple measure of electron localization in atomic and molecular systems. *The Journal of Chemical Physics* 92 (9), 5397 (1990).

109 Silvi, B. & Savin, A., Classification of chemical bonds based on topological analysis of electron localization functions. *Nature* 371 (6499), 683 (1994).

110 Pecharsky, V.K. & Zavalji, P.Y., Fundamentals of powder diffraction and structural characterization of materials. *Springer*, pp1-11 (Second edition).

111 Warren, B.E., X-ray diffraction. *Dover Publication Inc.* , pp15-40 (1990).

112 Dinnebier, R.E. & Billinge, S.J.L., Powder diffraction theory and practice. *RSC Publishing*, pp376-381 (2008).

113 Watt, I.M., Principles and practice of electron microscopy. *Cambridge University Press*, pp59-135 (Second edition).

114 Craig, D.P. & Thirunamachandran, T., Molecular quantum electrodynamics:An introduction to radiation molecule interactions. *Dover Publication Inc.* , pp128-141 (1984).

115 Stöhr, J. *et al.*, Extended absorption fine structure studies above the carbon, nitrogen, oxygen, and fluorine K absorption edges. *Applied Optics* 19 (23), 3911 (1980).

116 Rehr, J.J. & Albers, R.C., Theoretical approaches to x-ray absorption fine structure. *Reviews of Modern Physics* 72 (3), 621 (2000).

117 Zhu, W., Börjesson, A., & Bolton, K., DFT and tight binding Monte Carlo calculations related to single-walled carbon nanotube nucleation and growth. *Carbon* 48 (2), 470.

118 Ye-Fei, L. & et al., The computational design of junctions between carbon nanotubes and graphene nanoribbons. *Nanotechnology* 20 (22), 225202 (2009).

119 Hersam, M.C., Progress towards monodisperse single-walled carbon nanotubes. *Nature Nanotechnology* 3 (7), 387 (2008).

120 Zheng, M. *et al.*, DNA-assisted dispersion and separation of carbon nanotubes. *Nature Materials* 2 (5), 338 (2003).

121 Krupke, R., Hennrich, F., Lohneysen, H.v., & Kappes, M.M., Separation of metallic from semiconducting single-walled carbon nanotubes. *Science* 301 (5631), 344 (2003).

122 Wang, B. *et al.*, (n,m) Selectivity of single-walled carbon nanotubes by different carbon precursors on Co-Mo catalysts. *Journal of the American Chemical Society* 129 (29), 9014 (2007).

123 Kresse, G. & Hafner, J., Ab initio molecular dynamics for liquid metals. *Physical Review B* 47 (1), 558 (1993).

124 Mehrez, H., Svizhenko, A., Anantram, M.P., Elstner, M., & Frauenheim, T., Analysis of band-gap formation in squashed armchair carbon nanotubes. *Physical Review B* 71 (15), 155421 (2005).

125 Sun, C.-H., Yin, L.-C., Li, F., Lu, G.-Q., & Cheng, H.-M., Van der Waals interactions between two parallel infinitely long single-walled nanotubes. *Chemical Physics Letters* 403 (4-6), 343 (2005).

126 Popescu, A., Woods, L.M., & Bondarev, I.V., Simple model of van der Waals interactions between two radially deformed single-wall carbon nanotubes. *Physical Review B* 77 (11), 115443 (2008).

127 Saxena, S. & Tyson, T.A., Interacting quasi-two-dimensional sheets of interlinked carbon nanotubes: A high-pressure phase of carbon. *ACS Nano* 4 (6), 3515 (2010).

128 Stein, S.E. & Brown, R.L., .pi.-Electron properties of large condensed polyaromatic hydrocarbons. *Journal of the American Chemical Society* 109 (12), 3721 (1987).

129 Saxena, S. & Tyson, T.A., Role of edge states in graphene nanoribbons:- DFT studies. *Proceedings of the American Physical Society March Meeting* 54 (1) (2009).

130 Gass, M.H. *et al.*, Free-standing graphene at atomic resolution. *Nature Nanotechnology* 3 (11), 676 (2008).

131 Braga, S.F. *et al.*, Structure and dynamics of carbon nanoscrolls. *Nano Letters* 4 (5), 881 (2004).

132 Xie, X. *et al.*, Controlled fabrication of high-quality carbon nanoscrolls from monolayer graphene. *Nano Letters* 9 (7), 2565 (2009).

133 Campos-Delgado, J. *et al.*, Thermal stability studies of CVD-grown graphene nanoribbons: Defect annealing and loop formation. *Chemical Physics Letters* 469 (1-3), 177 (2009).

134 Liu, Z., Suenaga, K., Harris, P.J.F., & Iijima, S., Open and Closed Edges of Graphene Layers. *Physical Review Letters* 102 (1), 015501 (2009).

135 Saxena, S. & Tyson, T.A., Ab initio density functional studies of the restructuring of graphene nanoribbons to form tailored single walled carbon nanotubes. *Carbon* 48, 1153 (2010).

136 Barboza, A.P.M., Chacham, H., & Neves, B.R.A., Universal response of single-wall carbon nanotubes to radial compression. *Physical Review Letters* 102 (2), 025501 (2009).

137 Shenoy, V.B., Reddy, C.D., Ramasubramaniam, A., & Zhang, Y.W., Edge-stress-induced warping of graphene sheets and nanoribbons. *Physical Review Letters* 101 (24), 245501 (2008).

138 Du, A.J., Smith, S.C., & Lu, G.Q., Formation of single-walled carbon nanotube via the interaction of graphene nanoribbons: Ab initio density functional calculations. *Nano Letters* 7 (11), 3349 (2007).

139 Geerlings, P., De Proft, F., & Langenaeker, W., Conceptual density functional theory. *Chemical Reviews* 103 (5), 1793 (2003).

140 Juan, F.C. & Andrei, G., The effect of bundling on the G' Raman band of single-walled carbon nanotubes. *Nanotechnology* 20 (46), 465703 (2009).

141 Delaney, P., Choi, H.J., Ihm, J., Louie, S.G., & Cohen, M.L., Broken symmetry and pseudogaps in ropes of carbon nanotubes. *Nature* 391 (6666), 466 (1998).

142 Salvetat, J.-P. *et al.*, Elastic and shear moduli of single-walled carbon nanotube ropes. *Physical Review Letters* 82 (5), 944 (1999).

143 Sears, A. & Batra, R.C., Macroscopic properties of carbon nanotubes from molecular-mechanics simulations. *Physical Review B* 69 (23), 235406 (2004).

144 Merlen, A. *et al.*, Resonant Raman spectroscopy of single-wall carbon nanotubes under pressure. *Physical Review B* 72 (3), 035409 (2005).

145 Lu, J.-Q. *et al.*, Metal-to-semiconductor transition in squashed armchair carbon nanotubes. *Physical Review Letters* 90 (15), 156601 (2003).

146 Tangney, P., Capaz, R.B., Spataru, C.D., Cohen, M.L., & Louie, S.G., Structural transformations of carbon nanotubes under hydrostatic pressure. *Nano Letters* 5 (11), 2268 (2005).

147 Sharma, S.M. *et al.*, Pressure-induced phase transformation and structural resilience of single-wall carbon nanotube bundles. *Physical Review B* 63 (20), 205417 (2001).

148 Rols, S., Goncharenko, I.N., Almairac, R., Sauvajol, J.L., & Mirebeau, I., Polygonization of single-wall carbon nanotube bundles under high pressure. *Physical Review B* 64 (15), 153401 (2001).

149 López, M.J., Rubio, A., Alonso, J.A., Qin, L.C., & Iijima, S., Novel Polygonized Single-Wall Carbon Nanotube Bundles. *Physical Review Letters* 86 (14), 3056 (2001).

150 Yildirim, T., Gülseren, O., C., K., & Ciraci, S., Pressure-induced interlinking of carbon nanotubes. *Physical Review B* 62 (19), 12648 (2000).

151 Wang, Z. *et al.*, A quenchable superhard carbon phase synthesized by cold compression of carbon nanotubes. *Proceedings of the National Academy of Sciences of the United States of America* 101 (38), 13699 (2004).

152 Chhowalla, M., Ferrari, A.C., Robertson, J., & Amaratunga, G.A.J., Evolution of sp^2 bonding with deposition temperature in tetrahedral amorphous carbon studied by Raman spectroscopy. *Applied Physics Letters* 76 (11), 1419 (2000).

153 Park, C.-J., Kim, Y.-H., & Chang, K.J., Band-gap modification by radial deformation in carbon nanotubes. *Physical Review B* 60 (15), 10656 (1999).

154 Bulusheva, L.G., Okotrub, A.V., Romanov, D.A., & Tomanek, D., Electronic structure of (n,0) zigzag carbon nanotubes: Cluster and crystal approach. *The Journal of Physical Chemistry A* 102 (6), 975 (1998).

155 Kunstmann, J., Quandt, A., & Boustani, I., An approach to control the radius and the chirality of nanotubes. *Nanotechnology* 18 (15), 155703 (2007).

156 Lau, K.C., Pati, R., Pandey, R., & Pineda, A.C., First-principles study of the stability and electronic properties of sheets and nanotubes of elemental boron. *Chemical Physics Letters* 418 (4-6), 549 (2006).

157 Boustani, I., Systematic ab initio investigation of bare boron clusters:Determination of the geometryand electronic structures of Bn. *Physical Review B* 55 (24), 16426 (1997).

158 Quandt, A. & Boustani, I., Boron Nanotubes. *ChemPhysChem* 6 (10), 2001 (2005).

159 Tang, H. & Ismail-Beigi, S., Novel Precursors for Boron Nanotubes: The Competition of two-center and three-center bonding in boron sheets. *Physical Review Letters* 99 (11), 115501 (2007).

160 Gonzalez Szwacki, N., Sadrzadeh, A., & Yakobson, B.I., B80 fullerene: An ab initio prediction of geometry, stability, and electronic structure. *Physical Review Letters* 98 (16), 166804 (2007).

161 Brey, L. & Fertig, H.A., Electronic states of graphene nanoribbons studied with the Dirac equation. *Physical Review B* 73 (23), 235411 (2006).

162 Tang, W. & et al., A grid-based Bader analysis algorithm without lattice bias. *Journal of Physics: Condensed Matter* 21 (8), 084204 (2009).

163 Sanville, E., Kenny, S.D., Smith, R., & Henkelman, G., Improved grid-based algorithm for Bader charge allocation. *Journal of Computational Chemistry* 28 (5), 899 (2007).

164 Henkelman, G., Arnaldsson, A., & Jónsson, H., A fast and robust algorithm for Bader decomposition of charge density. *Computational Materials Science* 36 (3), 354 (2006).

165 Kiran, B. *et al.*, Planar-to-tubular structural transition in boron clusters: B20 as the embryo of single-walled boron nanotubes. *Proceedings of the National Academy of Sciences of the United States of America* 102 (4), 961 (2005).

166 Breslow, R., Antiaromaticity. *Accounts of Chemical Research* 6 (12), 393 (1973).

167 Ding, Y., Yang, X., & Ni, J., Electronic structures of boron nanoribbons. *Applied Physics Letters* 93 (4), 043107 (2008).

168 Barone, V., Hod, O., & Scuseria, G.E., Electronic structure and stability of semiconducting graphene nanoribbons. *Nano Letters* 6 (12), 2748 (2006).

169 Sakai, S., Ab Initio molecular orbital study of the chemical reactions of diborane with ammonia. *The Journal of Physical Chemistry* 99 (16), 5883 (1995).

170 Geim, A.K. & Novoselov, K.S., The rise of graphene. *Nature Materials* 6 (3), 183 (2007).

171 Gao, W., Alemany, L.B., Ci, L., & Ajayan, P.M., New insights into the structure and reduction of graphite oxide. *Nature Chemistry* 1 (5), 403 (2009).

172 Hirata, M., Gotou, T., Horiuchi, S., Fujiwara, M., & Ohba, M., Thin-film particles of graphite oxide: High-yield synthesis and flexibility of the particles. *Carbon* 42 (14), 2929 (2004).

173 Titantah, J.T., Lamoen, D., Schowalter, M., & Rosenauer, A., Density-functional theory calculations of the electron energy-loss near-edge structure of Li-intercalated graphite. *Carbon* 47 (10), 2501 (2009).

174 Froudakis, G.E. *et al.*, Pathways for oxygen adsorption on single-wall carbon nanotubes. *Physical Review B* 68 (11), 115435 (2003).

175 Cai, W. *et al.*, Synthesis and solid-state NMR structural characterization of 13C-labeled graphite oxide. *Science* 321 (5897), 1815 (2008).

176 Si, Y. & Samulski, E.T., Synthesis of water soluble graphene. *Nano Letters* 8 (6), 1679 (2008).

177 Li, D., Muller, M.B., Gilje, S., Kaner, R.B., & Wallace, G.G., Processable aqueous dispersions of graphene nanosheets. *Nature Nanotechnology* 3 (2), 101 (2008).

178 Abe, T. *et al.*, Carbon K edge XANES spectra of stage 2 FeCl3-graphite intercalation compound. *Carbon* 34 (9), 1160 (1996).

179 Fischer, D.A., Wentzcovitch, R.M., Carr, R.G., Continenza, A., & Freeman, A.J., Graphitic interlayer states: A carbon K near-edge x-ray-absorption fine-structure study. *Physical Review B* 44 (3), 1427 (1991).

180 Vance, A.L. *et al.*, XAS and XPS characterization of a surface-attached rotaxane. *Nano Letters* 3 (1), 81 (2002).

181 Jeong, H.-K. *et al.*, X-ray absorption spectroscopy of graphite oxide. *Europhysics Letters* (6), 67004 (2008).

182 Kuznetsova, A. *et al.*, Oxygen-containing functional groups on single-wall carbon nanotubes: NEXAFS and vibrational spectroscopic studies. *Journal of the American Chemical Society* 123 (43), 10699 (2001).

183 Posternak, M., Baldereschi, A., Freeman, A.J., Wimmer, E., & Weinert, M., Prediction of electronic interlayer states in graphite and reinterpretation of alkali bands in graphite intercalation compounds. *Physical Review Letters* 50 (10), 761 (1983).

184 Saxena, S. & Tyson, T.A., Insights on the atomic and electronic structure of boron nanoribbons. *Physical Review Letters* 104, 245502 (2010).

185 Pacile, D. *et al.*, Near-edge x-ray absorption fine-structure investigation of graphene. *Physical Review Letters* 101 (6), 066806 (2008).

186 Chen, J., Lin, C.L., Qiu, S.L., Strongin, M., & denBoer, M.L., Auger and x-ray absorption studies of solid molecular oxygen. *Journal of Vacuum Science & Technology A: Vacuum, Surfaces, and Films* 8 (3), 2591 (1990).

187 Billinge, S.J.L. & Levin, I., The Problem with determining atomic structure at the nanoscale. *Science* 316 (5824), 561 (2007).